Universidade Federal do Rio Grande – FURG

Instituto de Oceanografia

Programa de Pós-Graduação em Oceanologia

Influence of the Drake Low and Atmospheric Rivers on Glaciers of the South Shetland Islands, Antarctica

Christian Manuel Torres Ramos

Tese apresentada ao Programa de Pós-Graduação em Oceanologia, como parte dos requisitos para a obtenção do Título de Doutor.

Supervisor: Dr. Prof. Jorge Arigony-Neto

Universidade Federal do Rio Grande (FURG), Brasil.

Co-supervisor: Dr. Prof. Deniz Bozkurt

Universidad de Valparaíso, Chile

Rio Grande, RS, Brazil

June – 2024

Influence of the Drake Low and Atmospheric Rivers on Glaciers of the South Shetland Islands, Antarctica

Tese apresentada ao Programa de Pós-Graduação em Oceanologia, como parte dos requisitos para a obtenção do Título de Doutor.

Christian Manuel Torres Ramos

Rio Grande, RS, Brazil

June – 2024

UNIVERSIDADE FEDERAL DO RIO GRANDE - FURG
INSTITUTO DE OCEANOGRAFIA – IO
PROGRAMA DE PÓS-GRADUAÇÃO EM OCEANOLOGIA
E-mail: ccpofqg@furg.br – home-page: www.ppgo.furg.br

ATA ESPECIAL DE DEFESA DE TESE DE DOUTORADO – 01/2024

Às 9 horas do dia 15 de maio do ano dois mil e vinte e quatro, por videoconferência na sala: https://conferenciaweb.rnp.br/sala/jorge-arigony-neto, a Comissão Examinadora da Tese de **DOUTORADO** intitulada **"Influence of the Drake Low and Atmospheric Rivers on Glaciers of the South Shetland Islands, Antarctica (Influência da Baixa de Drake e Rios Atmosféricos nas Geleiras das Ilhas Shetland do Sul, Antártica)"**, do **Acad. Christian Manuel Torres Ramos**. A Comissão Examinadora foi composta pelos seguintes membros: Prof. Dr. Jorge Arigony Neto – Orientador (FURG), Prof. Dr. Deniz Bozkurt – Coorientador (Universidad de Valparaíso), Prof. Dr. Jefferson Cardia Simões (UFRGS), Prof. Dr. Ricardo Jaña (INACH), Prof. Dr. Jeferson P. Machado (FURG), Prof. Dr. Felipe Daniel Garcia Rodrigues (FURG/Universidad de la República). Dando início à reunião, a Coordenadora do PPGO, Profa. Dra. Grasiela L. L. Pinho, agradeceu a presença de todos e fez a apresentação da Comissão Examinadora. Logo após, esclareceu que o candidato teria um tempo de 45 a 60 min para explanação do tema, e cada membro da Comissão Examinadora, um tempo máximo de 30 min para perguntas. A seguir, passou a palavra ao candidato que apresentou o tema e respondeu às perguntas formuladas. Após ampla explanação, a Comissão Examinadora reuniu-se em reservado para discussão do conceito a ser atribuído ao candidato. Foi estabelecido que as sugestões de todos os membros da Comissão Examinadora, que seguem em pareceres em anexo, foram aceitas pelo Orientador/Candidato para incorporação na versão final da Dissertação. Finalmente, a Comissão Examinadora considerou o candidato APROVADO por unanimidade. Nada mais havendo a tratar, foi lavrada a presente ATA, por mim, Clabisnei Moura de Melo – Secretário PPGO, que após lida e aprovada, será assinada pela Comissão Examinadora, pelo Candidato e pela Coordenadora Adjunta do Programa de Pós-Graduação em Oceanologia.

gov.br Documento assinado digitalmente
JORGE ARIGONY NETO
Data: 21/05/2024 18:22:47-0300
Verifique em https://validar.iti.gov.br

Prof. Dr. Jorge Arigony Neto
Orientador

Prof. Dr. Deniz Bozkurt
Coorientador

gov.br Documento assinado digitalmente
JEFFERSON CARDIA SIMOES
Data: 22/05/2024 18:26:59-0300
Verifique em https://validar.iti.gov.br

Prof. Dr. Jefferson Cardia Simões

Prof. Dr. Ricardo Jaña

gov.br Documento assinado digitalmente
FELIPE DANIEL GARCIA RODRIGUEZ
Data: 22/05/2024 10:26:04-0300
Verifique em https://validar.iti.gov.br

Prof. Dr. Jeferson P. Machado

Prof. Dr. Felipe Daniel Garcia Rodrigues

gov.br Documento assinado digitalmente
JEFERSON PRIETSCH MACHADO
Data: 21/05/2024 21:43:29-0300
Verifique em https://validar.iti.gov.br

Acad. Christian Manuel Torres Ramos

Profª. Drª Grasiela L. L. Pinho
Coordenadora PPGO

gov.br Documento assinado digitalmente
CHRISTIAN MANUEL TORRES RAMOS
Data: 21/05/2024 18:33:54-0300
Verifique em https://validar.iti.gov.br

gov.br Documento assinado digitalmente
GRASIELA LOPES LEAES PINHO
Data: 21/05/2024 17:28:22-0300
Verifique em https://validar.iti.gov.br

Contents

Acknowledgments

I would especially like to thank Jorge Arigony-Neto for his mentoring during these 6 years from master's degree to PhD. Besides being my mentor, he is now a great friend. This PhD started in June 2020 during the COVID-19 pandemic. I remember I was about to return to Peru when the pandemic started, for several months I was unable to do anything stranded in Brazil, at that time Jorge motivated me and invited me to apply to the Graduate Program in Oceanology (PPGO). That's when it all started. Now I believe that in challenging times there can be opportunities depending on how we look at it and how we approach it.

I would like to thank Deniz Bozkurt, who has been my co-supervisor during my 10-month exchange at the University of Valparaíso, Chile. During this period I have been able to grow professionally and personally, and we have discussed cultural and social issues. Deniz has been a great co-supervisor who has provided valuable feedback for the finalisation of manuscripts and international collaborative research initiatives.

During the PhD period, I met Vitoria de Lima Cardoso who will soon be my wife. I thank her and her family for their support at all times. Before, I felt lonely because I was far away from the love and warmth of my family. However, since I met Vitoria and her family, that feeling disappeared. Now, I feel that I will stay in these "gauchas" lands to continue growing and building a family.

I thank my family, dad Robert and Ana, mum Pilar, siblings Carlos and Stefeany, grandparents Maria and Isidro, nieces and nephews, aunts and uncles. They are always present and give me a lot of energy to continue even when I am so far away from home.

I thank my friends and colleagues from the FURG Transit Hotel, Edwin, Paco, Mariano, Mary, Maite, etc, who were initially with me sharing experiences and knowledge. Furthermore, my new colleagues Eduardo and Pamela from Laboratório de Monitoramento da Criosfera (LaCrio) with whom I now discuss new research ideas. I would also like to thank all the people who were present at some point during the development of this thesis.

I am very grateful to the Scientific Committee on Antarctic Research (SCAR) for all the financial support they gave me to participate in international events and exchanges. I am also grateful to my friend Wolfgang Gurgiser from the University of Innsbruck, Austria, who invited me and supported me with a grant from his university to do a training course in his research group. These trips certainly helped me to extend my network and gave me the possibility to meet new people and cultures from all over the world.

In addition, I would like to thank the National Laboratory for High Performance Computing (NLHPC) from the University of Chile, this project was partially supported by the supercomputing infrastructure of the NLHPC (ECM-02:Powered@NLHPC).

Finally, I thank the professors and colleagues of PPGO, who provided me with solid knowledge and good discussions in the field of oceanography. I express gratitude to the CAPES for supporting the PPGO at the FURG.

Lists of Figures

List of Tables

List of Acronyms

A

AMS - American Meteorological Society

AIS - Antarctic Ice Sheet

ASL - Amundsen Sea Low

ARs - Atmospheric Rivers

AP - Antarctic Peninsula

AWS - Automatic Weather Station

C

CP - Central Pacific

COSIPY - COupled Snowpack and Ice surface energy and mass balance model in PYthon

D

Drake - Drake low

DC-CPAC - deep convection in the central tropical Pacific

E

ENSO - El Nino Southern Oscillation

EP - Eastern Pacific

ECMWF - European Centre for Medium-range Weather Forecasts

F

FPG-AWS - Fourcade and Polar Club Glacier station

J

JCI - Spanish Base Juan Carlos I

K

KKS-AWS - Korean King Sejong Station

L

LWS - low over the Weddell Sea

LAB - low over the Amundsen and Bellingshausen Seas

LDP - low over the Drake Passage

LWin - incoming longwave radiation

M

MSLP - Mean Sea Level Pressure

O

OLR - outgoing longwave radiation

P

PSFC - surface pressure

PDD - Positive Degree-Days

R

RAP - ridge over the Antarctic Peninsula

RH2 - relative humidity at 2 m

REMA - Reference Elevation Model of Antarctica

RMSE - root mean squared error

RACMO - Regional Atmospheric Climate MOdel

S

SMB - Surface Mass Balance

SAM - Southern Annular Mode

SIE - Sea Ice Extent

SIC - Sea Ice Concentration

SSI - South Shetland Islands

SAT - Surface Air Temperature

SACR - The Scientific Committee on Antarctic Research

SWin - incoming shortwave radiation

T

T2 - air temperature at 2 m

TP - total precipitation

Z

ZDP - zonal flow over the Drake Passage

W

WS - wind speed at 2 m

WGMS - World Glacier Monitoring Service

Abstract

The Antarctic Peninsula (AP) is one of the fastest-warming regions in the Antarctic continent due to its northernmost location, generating significant changes in precipitation patterns, glacial surface mass balance (SMB), impacts on the coastal environment, etc. Several studies link these changes to the main modes of climate variability, such as El Niño-Southern Oscillation (ENSO) and the Southern Annular Mode (SAM). It has also recently been indicated that these changes may be enhanced by Atmospheric Rivers (AR) events reaching the AP. However, over some regions, such as northern AP, these large-scale modes and AR events may have less influence compared to regional-scale climate forcing factors, such as the Amundsen Sea Low (ASL) and Drake Low (Drake). In this thesis, we evaluated the influence of climate and AR events and Drake on the interannual and seasonal variability of temperature, precipitation, and SMB of glaciers in the South Shetland Islands (SSI), located in the northern AP. For this purpose, we used different datasets from in-situ observations, glaciological and atmospheric regional climate models, and global reanalysis outputs. In addition, we comprehensively analysed the correlations and regressions between seasonal and annual temperature, precipitation, and SMB, with global-regional climate indices and a state-of-the-art AR tracking database from 1970 to 2020. The results reveal that both large- and regional-scale climate modes (i.e., ASL, SAM, and ENSO) have significant influences on the control of interannual and seasonal variability of surface temperature over SSI. While for precipitation and SMB over SSI, only the regional-scale modes (i.e., Drake) have significant influences on their interannual variability, although seasonally, the large-scale modes may have a weak but significant control. Furthermore, our findings reveal that ARs have dual effects on the SSI glacier's SMB. In glaciological winter, a positive correlation suggests ARs boost accumulation through increased snowfall. Conversely, in glaciological summer, a negative correlation indicates ARs intensify glacier melting. Our study highlights the necessity of investigating the climate variability and change in the AP and its surrounding areas, stressing the importance of considering Drake region. Moreover, we underscore the detailed investigations into the seasonal and sub-seasonal impacts of ARs on the AP environment, particularly on small-scale coastal glaciers.

Keywords: Glaciers, Climate Forcings, Atmospheric Rivers, Temperature, Precipitation, Surface Mass Balance, South Shetland Islands.

Resumo

A Península Antártica (AP) é uma das regiões que mais rapidamente está aquecendo no continente Antártico, devido à sua localização mais ao norte, gerando mudanças significativas nos padrões de precipitação, balanço de massa superficial das geleiras (SMB), impactos no ambiente costeiro, etc. Vários estudos relacionam essas mudanças aos principais modos de variabilidade climática, como o El Niño-Southern Oscillation (ENSO) e o Southern Annular Mode (SAM). Também foi recentemente indicado que essas mudanças podem ser amplificadas por eventos de Rios Atmosféricos (AR) que alcançam a AP. No entanto, em algumas regiões, como o norte da AP, esses modos de grande escala e eventos de AR podem ter menos influência em comparação com forçantes climáticas em escala regional, como o Amundsen Sea Low (ASL) e Drake low (Drake). Nesta tese, avaliamos a influência do clima e dos eventos de AR na variabilidade interanual e sazonal de temperatura, precipitação e SMB das geleiras nas Ilhas Shetland do Sul (SSI), localizadas ao norte da AP. Para este fim, utilizamos diferentes conjuntos de dados de observações in situ, saídas de modelo climático regional, e de reanálise global. Além disso, analisamos amplamente as correlações e regressões entre temperatura, precipitação e SMB sazonal e anual, com índices climáticos globais-regionais e um banco de dados de rastreamento de AR de última geração de 1980 a 2020. Os resultados revelam que tanto os modos climáticos de escala-larga-regional (e.i., ASL, SAM e ENOS) têm influências significativas no controle da variabilidade interanual e sazonal da temperatura superficial sobre as SSI. Enquanto para a precipitação e SMB sobre as SSI, apenas um modo de escala regional (i.e., Drake low) têm influências significativas em sua variabilidade interanual, embora sazonalmente os modos de escala-larga possam ter um controle fraco, mas significativo. Além disso, nossas descobertas revelam que os ARs têm efeitos duplos no SMB das geleiras da SSI. No inverno, uma correlação positiva sugere que os ARs aumentam a acumulação por meio do aumento da queda de neve. Por outro lado, no verão, uma correlação negativa indica que os ARs intensificam o derretimento das geleiras. Nosso estudo destaca a necessidade de investigar a variabilidade e a mudança climática na AP e em suas áreas circundantes, destacando a importância de considerar a região de Drake. Além disso, enfatizamos a necessidade de mais investigações detalhadas sobre os impactos sazonais e sub-sazonais dos ARs no ambiente da AP, especialmente em pequenas geleiras costeiras.

Palavras-Chave: Geleiras, Forçantes Climáticas, Rios Atmosféricos, Temperatura, Precipitação, Balanço de Massa Superficial, Ilhas Shetland do Sul.

Resumen

La Península Antártica (AP) es una de las regiones del continente Antártico que se calienta más rápidamente, debido a su ubicación más septentrional, generando cambios significativos en los patrones de precipitación, el balance de masa superficial de los glaciares (SMB), los impactos en el medio ambiente costero, etc. Varios estudios vinculan estos cambios en los principales modos de variabilidad climática como El Niño-Southern Oscillation (ENSO) y el Southern Annular Mode (SAM). También se ha indicado recientemente que estos cambios pueden verse potenciados por eventos de ríos atmosféricos (AR) que llegan al AP. Sin embargo, en algunas regiones, como el norte de AP, estos modos de gran escala y eventos AR pueden tener menos influencia en comparación con los forzantes climáticos de escala regional, como Amundsen Sea Low (ASL) y Drake low (Drake). En esta tesis, evaluamos la influencia del clima y los eventos AR en la variabilidad interanual y estacional de la temperatura, precipitación y SMB de los glaciares en las Islas Shetland del Sur (SSI), ubicadas al norte de AP. Para ello, utilizamos diferentes conjuntos de datos de observaciones in-situ, modelos climáticos regionales y resultados de reanálisis global. Además, analizamos las correlaciones y regresiones entre la temperatura, la precipitación y el SMB estacional y anual, con índices climáticos globales-regionales y una base de datos de seguimiento AR de última generación de 1980 a 2020. Los resultados revelan que ambos índices climáticos de larga-regional escala (i.e., ASL, SAM y ENSO) tienen influencias significativas en el control de la variabilidad interanual y estacional de la temperatura de la superficie sobre SSI. Mientras que para la precipitación y SMB sobre SSI solo un índice de escala regional (i.e., Drake) tiene influencia significativa en su variabilidad interanual, aunque estacionalmente los modos a gran escala pueden tener un control débil pero significativo. Además, nuestros hallazgos revelan que los AR tienen doble efecto en el SMB del glaciar SSI. En el invierno, una correlación positiva sugiere que las AR aumentan la acumulación a través del aumento de las nevadas. Por el contrario, en el verano, una correlación negativa indica que las AR intensifican el derretimiento de los glaciares. Nuestro estudio destaca la necesidad de investigar la variabilidad y el cambio climático en la AP y sus áreas circundantes, enfatizando la importancia de considerar la región de Drake. Finalmente, destacamos las investigaciones detalladas sobre los impactos estacionales y sub-estacionales de los AR en el medio ambiente de AP, particularmente en los glaciares costeros de pequeña escala.

Palabras claves: Glaciares, Forzamientos Climáticos, Ríos Atmosféricos, Temperatura, Precipitación, Balance de Masa Superficial, Islas Shetland del Sur.

Chapter I Introduction: The Antarctic Peninsula climate systems

The Antarctic continent is geographically divided into three main regions: East Antarctica, West Antarctica, and the Antarctic Peninsula (AP). Situated as the northernmost extension of the Antarctic continent, the AP stretches northward from Ellsworth Land (near 75°S) for approximately 1300 km, terminating near 62°S. This rugged peninsula serves as a natural mountain barrier, separating the Pacific and Atlantic oceans. With an average width of 70 km and an elevation ranging from approximately 800 m at its northern tip to over 2000 m in the central-south, the AP cordillera forms an orographic obstacle to the prevailing near-surface westerly flow. As a result of this geographical configuration, the AP experiences two distinct climatic zones: a relatively mild and humid marine climate on the windward west coast and a colder continental climate on the leeward east coast (King and Turner, 1997). In the following subsections, we describe the current understanding of the Antarctic climate, focusing on the AP, the impact of large-scale climate forcing factors on temperature, precipitation and glaciers in this region. The next sections are divided into 5 topics: temperature and sea ice, precipitation and regional atmospheric circulation, atmospheric rivers, glaciers and their relationship to climate, and finally the study area and thesis context.

1.1 Temperature and sea ice

The AP is one of the most climatologically variable areas of Antarctica. In the last decades, this region presented warming (0.32 °C/decade during 1979–1997) and cooling (-0.47 °C/decade during 1999–2014) trends (Turner et al., 2016; 2020; Olivia at al., 2017; Carrasco et al., 2021). The annual mean temperature in this region is mainly influenced by the Southern Annular Mode (SAM), which is the primary mode of atmospheric circulation variability at high Southern latitudes. The SAM can also be considered a proxy for the strength of the circumpolar westerlies around Antarctica. In recent decades, the SAM has become a more positive phase (i.e., stronger westerlies around the Antarctic continent) during summer in response to ozone depletion (Thompson and Solomon, 2002).

The mean sea level pressure (MSLP) fields are often used to study the influence of SAM on Antarctic temperature (e.g., Turner et al., 2020). In general, high (low) temperatures across the AP are associated with low (high) pressure anomalies over the Antarctic continent (Fig. 1d and e; Turner at al., 2020), which is the characteristic signature of the positive phase of the SAM. Furthermore, the Amundsen Sea Low (ASL), which is a climatological low-pressure centre located between the AP and the Ross Sea (Raphael et al., 2015), is particularly important in modulating the annual temperature of some regions located northwest of the AP, such as at the Vernadsky (Fig. 1c; Turner et al., 2020) and Bellingshausen (Bello et al., 2022) stations.

In addition to the SAM and ASL, sea surface temperature variability in the tropical regions can strongly influence the temperature of the AP, West and East Antarctica. This topical-polar teleconnection occurs through quasi-stationary atmospheric wave trains, known as Rossby Waves, originating in the tropical sector (Li et al., 2021). According to Li et al. (2021) Rossby wave trains are a series of cyclonic and anticyclonic vortices with a typical spatial scale of a thousand kilometres, superimposed on the uniform west to east flow, making up a succession of wave packages occurring at periodic intervals.

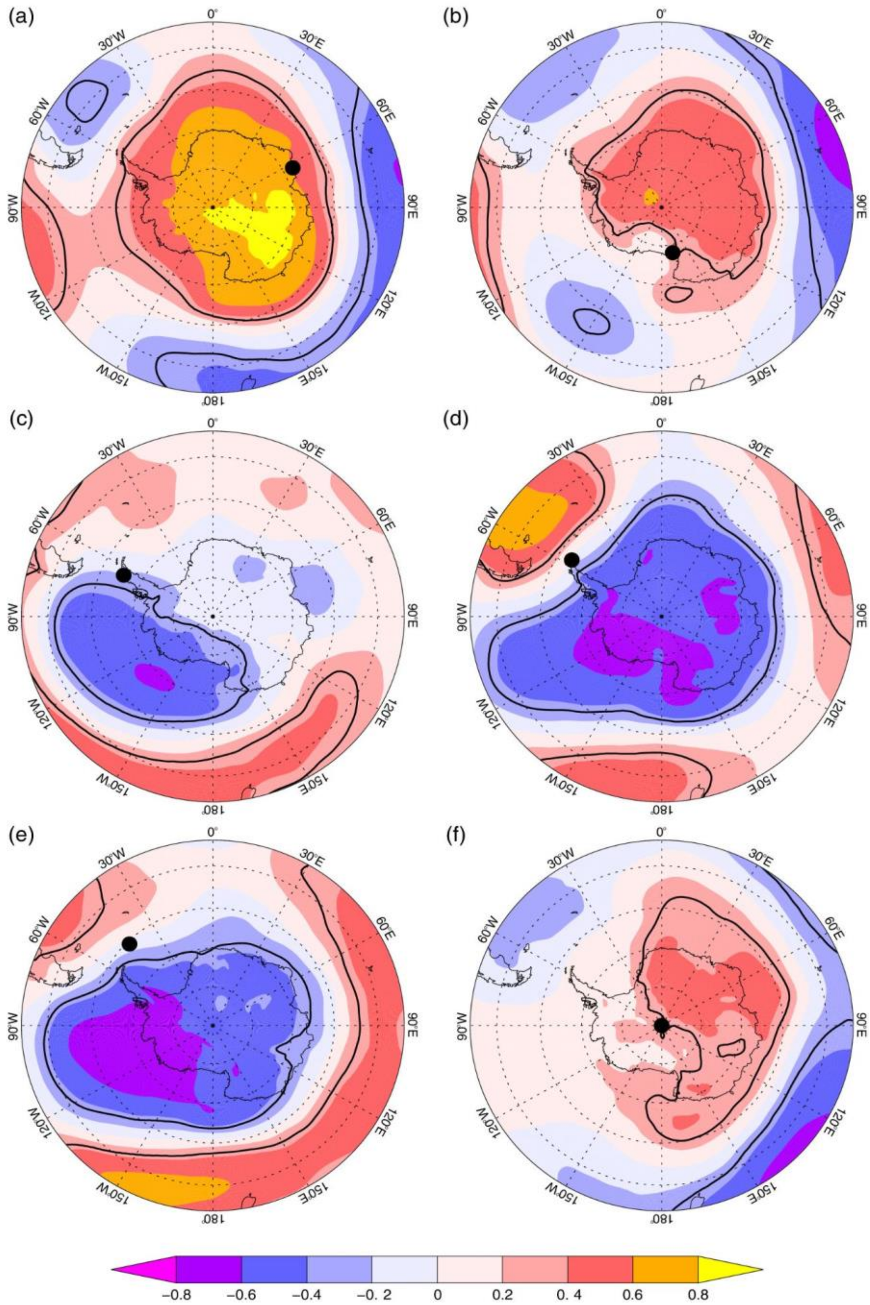

Figure 1. The correlation of the observed annual mean temperature time series for 1979–2018 with the spatial annual mean MSLP from ERA for the six stations considered in detail. (a) Mawson, (b) Scott Base, (c) Vernadsky, (d) Esperanza, (e) Orcadas and (f) Amundsen-Scott. The black dots indicate the locations of the stations. Source from: Turner et al. (2020).

Sea surface warming in the Pacific, Atlantic and Indian Oceans can generate Rossby waves that propagate towards the poles and cause important anomalies in these regions, such as Antarctica. El Niño-Southern Oscillation (ENSO) events are responsible for producing atmospheric patterns referred to as the Pacific–South American. Warming in the tropical Pacific Ocean produces convective motion anomalies in the atmosphere. This convection induces train waves that propagate southward and produce disturbances in the atmospheric circulation over the Southern Hemisphere. During these atmospheric anomalies, a low-pressure anomaly centre forms east of New Zealand, accompanied by a high-pressure anomaly near the Amundsen Sea (thus interacting with the ASL), and another low-pressure centre develops over southern America and the South Atlantic (Fig. 2a). Thus, during El Niño events, there is typically a weakening of the ASL, which can induce cooling in the AP of up to 1.5°C. Positive anomalies in sea ice concentration of up to 10-20% are also observed in the vicinity of the Amundsen, Bellingshausen, and Weddell Seas (Fig. 2b; Li et al., 2021). Conversely, the opposite effect is observed during La Niña events, which are associated with tropical Pacific cooling.

Various studies also have indicated that the impact of ENSO and SAM on AP temperature varies spatially and temporally (e.g., Fogt et al., 2011; Clem and Fogt 2013; Clem et al., 2016). A combined effect between SAM and ENSO can also influence the strengthening/weakening of ASL. Fogt et al. (2011) found that when a La Niña (El Niño) event occurs with a positive (negative) SAM phase, pressures within the ASL region are deeper (higher). However, the opposite effects of a positive SAM with El Niño, or a negative SAM with La Niña, lead to a very weak or totally absent ASL. Clem and Fogt (2013) noted persistent and significant relationships between ENSO and climate patterns in the western AP, while SAM-related relationships are prominent in the northeastern AP. Additionally, Clem at al. (2016) demonstrated that circulation changes associated with the SAM dominate the interannual variability of temperature across the entire AP during summer and autumn. Conversely, associations with ENSO are most pronounced and statistically significant primarily during winter and spring.

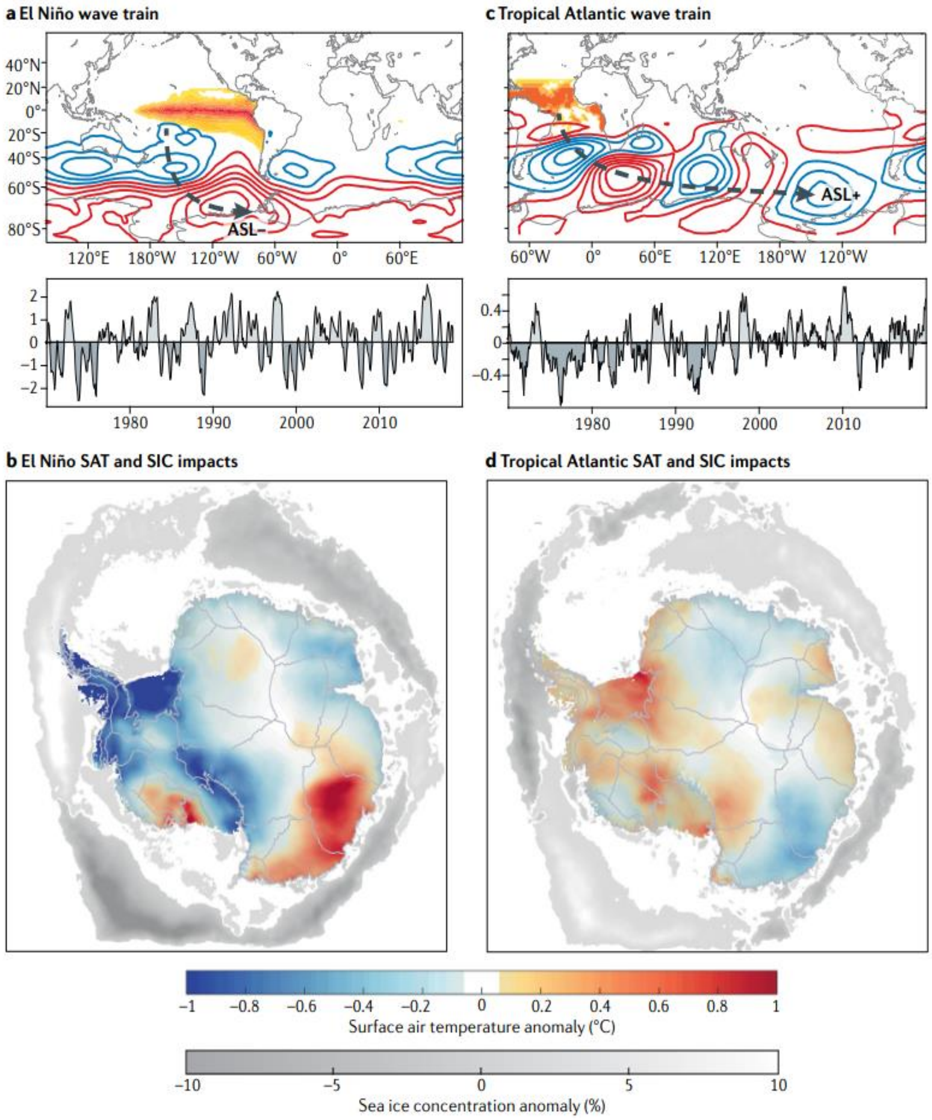

Figure 2. Tropical–polar teleconnection patterns on interannual timescales. (a) Austral winter (June, July, August; JJA) 500-hPa geopotential height anomalies (contours) associated with equatorial Pacific warming (colour shading) in the atmospheric model, NCAR CAM5. The pattern of sea surface temperature anomalies represents a one standard deviation positive JJA El Niño–Southern Oscillation event. Red and blue contours indicate positive and negative pressure anomalies, respectively, drawn at intervals of 8 m. The time series is that of the Niño 3.4 index . (b) JJA Antarctic surface air temperature (SAT) and sea ice concentration (SIC) anomalies regressed onto the standardised JJA Niño 3.4 index; patterns represent anomalies associated with a one standard deviation El Niño event. (c) As in panel a but for tropical Atlantic warming. The time series represents that of area-weighted mean temperature over the tropical Atlantic (20°S–20°N). (d) As in panel b but regressions onto the tropical Atlantic time series. Both El Niño–Southern Oscillation and tropical Atlantic sea surface temperature variability promote stationary Rossby wave patterns to the Southern Hemisphere high latitudes; atmospheric pressure anomalies centred over the Amundsen Sea Low (ASL), in turn, drive SAT and SIC anomalies. Source: Li et al. (2021).

These findings illustrate the complex and regionally variable impacts of ENSO events on Antarctic temperature, including the AP and surrounding regions. It highlights the importance of understanding the dynamics of large-scale climate phenomena such as ENSO and their influence on regional climate patterns in AP.

Stationary wave mechanisms operate not only in response to Pacific SST variability but also SST variability in other ocean basins, specifically, the tropical and northern Atlantic. During austral spring-autumn-winter, warming over the tropical Atlantic intensifies a wave train and forms a pathway from the subtropical Atlantic to the Amundsen-Bellingshausen Seas, centring the waves in West Antarctica (Fig. 2c; Li et al., 2021). Tropical Atlantic warming typically results in deepening of the ASL and drives a positive phase of the SAM, leading to warming in West Antarctica and AP. This warming tends to reduce sea ice extent overall but increase sea ice cover in the Ross Sea (Fig. 2d; Li et al., 2021).

1.2 Precipitation and regional atmospheric circulation

The precipitation in the AP and surrounding islands also shows an increasing trend across the region. Recently, Carrasco et al. (2021) reported two positive (1970-1991 = +60 mm/decade and 2000-2019 = +31 mm/decade) and a negative (1991-1999 = -95 mm/decade) annual precipitation trends over the northern AP during the 1970-2019 period. Various studies have investigated the influence of large-scale circulation variability (i.e., SAM and ESNO) on Antarctic and AP precipitation. Genthon et al. (2005) and Thomas et al. (2008) suggested that during the positive SAM polarity, precipitation increases (decreases) over West Antarctica and the western side of AP (i.e., the Antarctic interior). Furthermore, snow accumulation over the western side of the southern AP has doubled over the 20th century, which might be induced by positive SAM trends (Thomas et al., 2008). Bromwich et al. (2000) and Cullather et al. (1996) revealed a close positive correlation between ENSO (Southern Oscillation Index - SOI) and precipitation over the West Antarctic sector from the early 1980s to 1990, and a negative correlation after 1990. Gou et al. (2004) also found a positive correlation between ENSO and precipitation over Marie Byrd Land, West Antarctica (75°–90°S, 120°W–180°), but a negative correlation over the South Atlantic sector (65°–75°S, 30°–60°W) and AP. In comparison, Carrasco and Cordero (2020) showed no statistically significant connection between the precipitation on the northern AP and ENSO or SAM during the 1970-2019 period.

Recently, Chen et al. (2023) studied the distinct impacts of ENSO on AP precipitation during austral spring (September-November). Their results revealed that ENSO events in the eastern Pacific (EP) and central Pacific (CP) have similar impacts on the precipitation of a region spanning from Amundsen to Bellingshausen Seas, including the AP, but opposite impacts on precipitation over the Weddell Sea, especially in the east AP. During EP-El Niño events, precipitation generally decreases over the entire AP and the Amundsen-Bellingshausen Seas. Conversely, during CP-El Niño events, precipitation decreases mainly over the western AP and increases in the eastern AP (Fig. 3). Moreover, because of the offsetting effects of these two types of ENSO events on precipitation responses, the composite ENSO signal is less significant, particularly in the northern AP.

Along the near coast of the AP, frontal cyclonic systems are responsible for most of the snowfall (King and Turn 1997). Near the coast, the most important mechanism for the production of precipitation is the adiabatic cooling of the air as it rises up the steep topography that characterises many coastal areas (King and Turn 1997). Turner et al. (1995) indicated that precipitation at Rothera Station is mainly influenced by unstable synoptic systems. Wang et al. (2021) highlighted the importance of atmospheric circulation in determining the precipitation phase (i.e., rainfall and snowfall) over northern AP.

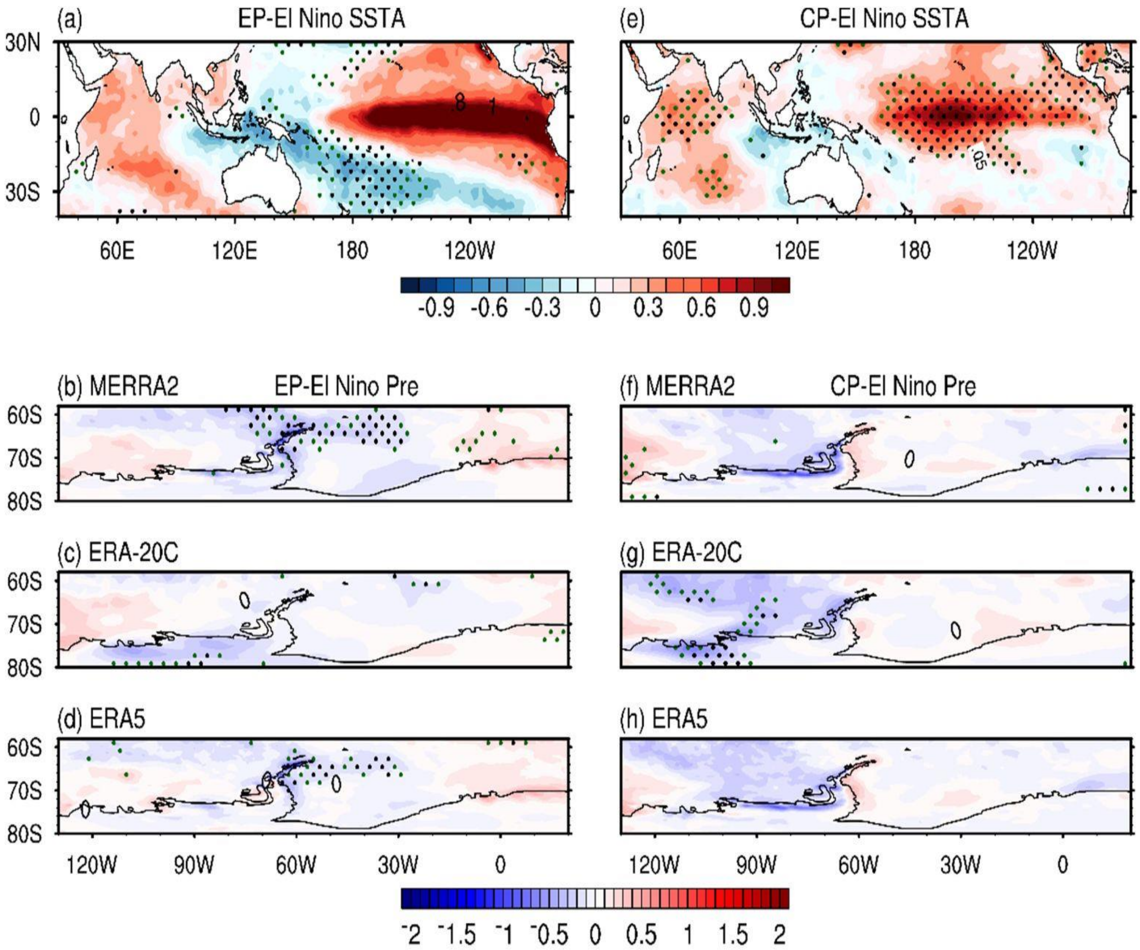

Figure 3. Composite (a, e) SSTA (units:°C) and (b–d, f–h) precipitation anomalies (units: mm d^{-1}) in the ABWS in the eight EP (left panels) and six CP (right panels) El Niño cases in 1980–2020. Three sets of precipitation datasets, from MERRA2, ERA-20C, and ERA5, respectively, were used. Dark green (black) stippled areas indicate statistical significance at the 90% (95%) confidence level. Source from: Chen et al. (2023).

Gonzalez et al. (2018) delineated five atmospheric circulation patterns affecting the AP: low over the Weddell Sea (LWS), low over the Amundsen and Bellingshausen Seas (LAB), low over the Drake Passage (LDP), zonal flow over the Drake Passage (ZDP), and ridge over the Antarctic Peninsula (RAP) (Fig. 4; Gonzalez et al., 2018). These patterns exert significant influence over temperature and precipitation dynamics in the AP. Their findings reveal that four of five atmospheric patterns (i.e., all except RAP) are strongly influenced by the SAM, with LAB and LWS additionally exhibiting some sensitivity to ENSO events. Furthermore, their analysis unveils a duality within the humidity and precipitation characteristics observed at the Spanish Base Juan Carlos I (JCI) Automatic Weather Station (AWS) situated on Livingston Island, particularly evident in the LDP pattern. This pattern displays two relative peaks in the density function for positive and negative temperature-humidity-precipitation anomalies. Notably, the study underscores that LAB does not determine the largest precipitation episodes but rather light drizzle events, while that the LDP and ZDP determine the largest anomalies of precipitation at JCI station.

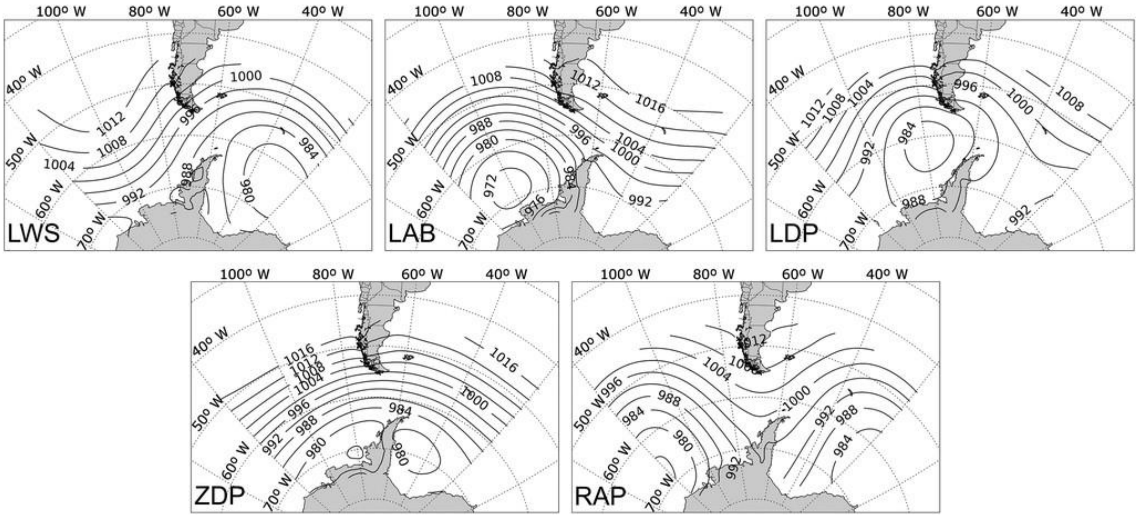

Figure 4. Synoptic patterns (cluster centroids) calculated using ERA-Interim reanalysis data for the AP region over the period between 1979 and 2016. Source: Gonzalez et al. (2018).

On the AP, the study of cyclones systems has been carried out since the 1980s (e.g., Carrasco et al., 1997; Carrasco et al., 2003; Turner et al., 2009; Setzer et al., 2022). These cyclones are associated with permanent or semi-permanent synoptic-scale low-pressure systems over the Weddell and Amundsen-Bellingshausen (e.g., ASL) regions. The AP is highly influenced by deep cyclonic systems from the Bellingshausen Sea that pass through the Drake Passage because it is located at the latitude of the circumpolar trough (Turner et al., 2009). Setzer et al. (2022) observed an increase in the number of explosive cyclones crossing the Drake Passage and reaching the northern AP with a significant positive trend of approximately 2.7 cyclones/decade, with a break in 2003 and average numbers of 7.3 and 11.8 events before and after that break, respectively. Generally, these cyclone systems can instigate strong wind (Turner et al., 2009; Kwon et al., 2019) and intense precipitation (Turner et al., 1997; Gonzalez et al., 2018) when interacting with the intricate topography of the AP. However, the precise extent of the impact of these low-pressure systems on meteorology and glaciology over this region remains unclear.

1.3 Atmospheric rivers on AP

In recent years, the scientific community has focused on understanding atmospheric rivers (ARs) and their associated impacts. The term ARs has been defined by the American Meteorological Society (AMS) as "A long, narrow, and transient corridor of strong horizontal water vapour transport that is typically associated with a low-level jet stream ahead of the coldfront of an extratropical cyclone. The water vapour in atmospheric rivers is supplied by tropical and/or extratropical moisture sources. Atmospheric rivers frequently lead to heavy precipitation where they are forced upward, for example, by mountains or by ascent in the warm conveyor belt. Horizontal water vapour transport in the midlatitudes occurs primarily in atmospheric rivers and is focused in the lower troposphere.".

Research on ARs in polar regions such as Antarctica is very recent with first publications available from 2014 (e.g., Gorodetskaya et al., 2014; Bozkurt et al., 2018; Wille et al., 2019; Clem et al., 2022). The life cycle of AR events are on very short timescales (i.e., 1 or 4 days) and are governed by Rossby wave dynamics. However, due to their strong impacts on the Antarctic climate system, the study of ARs is currently a very relevant research topic in the region.

Recent research has reported that ARs can affect the Antarctic continent in different ways, e.g. they can cause temperature extremes, intense precipitation, and break up of ice shelves (Bozkurt et al., 2018, Wille et al., 2021, Wille et al., 2022). Wille et al. (2022) indicated that the most intense ARs induce extremes in temperature, surface melt, sea-ice disintegration, or large swells that destabilise the ice shelves. This study revealed that strong ARs were precursors for more than 60% of the major calving events of the Larsen A and Larsen B ice shelves since 2000 (Fig. 5).

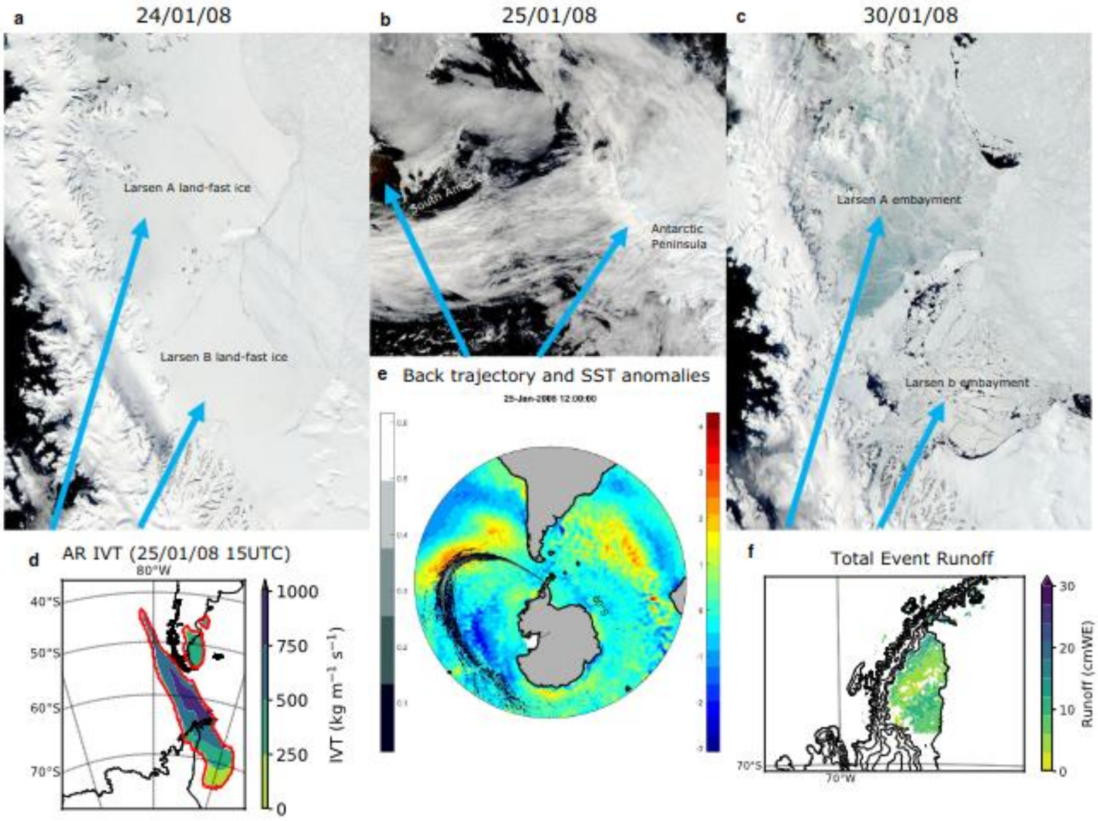

Figure 5. Overview of January 25th, 2008, AR over the AP. MODIS satellite imagery from a 24/01/08 and c 30/01/08 showing the land-fast ice and sea-ice decay after the passing of an AR as seen in b 25/01/08. d The shape and intensity of the detected AR on 25/01/08 15 UTC. e Flexpart footprints in 2D projections (stereographic). Colors (from black to white, see left color bar) on each grid point represent the number of particles over the 10-days back trajectory. This number is normalized by the total number of particles (on the 10-day period) and then multiplied by 10,000. It can be seen as the density of particles. Background (right color bar): Sea surface temperature anomaly calculated for the 19-01-08 to 23-01-08 period with respect to the 1980–2010 period. f The total runoff that occurred from 25/01/08–30/01/08. Satellite images from the NASA MODIS instrument in a, b, and c were obtained from the NASA Worldview application (https://worldview.earthdata.nasa.gov). Source: Wille et al. (2022).

The AR events reaching AP are generated by deep convection in the tropical region triggering Rossby waves. The genesis of AR events in the AP appear to be associated with global warming and the warming of small regions in the central tropical Pacific. Recent research suggests that these events are generated due to deep convention in small regions of the central tropical Pacific (Clem et al., 2022) and global warming together with ESNO (Gorodetskaya et al., 2023). Clem et al. (2022) indicated that during the summertime, deep convection in the central tropical Pacific (CPAC) produces atmospheric circulation anomalies over the South Pacific Ocean, favouring the transport of very warm and moist air to the southwest AP, often in the form of ARs. Then, these events produced strong foehn warming, generating high temperature and extreme surface melt on the eastern AP and Larsen C Ice Shelf. Gorodetskaya et al. (2023) also indicated that global warming played an important role in amplifying and increasing the probability of AR events over the AP, which favoured a new extreme warming event and a record surface melt in February 2022 over this region.

1.4 Glaciers and climate relationship

Changes in temperature and total precipitation (i.e., snowfall plus rainfall) in Antarctica influence the surface mass balance (SMB) of glaciers due to ablation and accumulation processes. The SMB, often defined as mm water equivalent (mm we/year), is the sum of all mass gains and losses of a glacier (i.e., accumulation, surface melt, refreezing, runoff, etc.). Over the Antarctic continent, accumulation depends mainly on snowfall or wind transport, while ablation is mainly associated with atmosphere and ocean temperature anomalies. As described in the previous sections, the temperature over the AP is increasing significantly and glaciers over this region are expected to lose mass.

The Antarctic Ice Sheet (AIS) mass loss has increased from 40±9 Gt/year in 1979-1990 to 252±26 Gt/year in 2009-2017 (Fig. 6; Rignot et al., 2019). This mass loss is primarily concentrated in the Amundsen Sea sector and the AP, combined accounting for 81% of the total AIS mass loss between 2003 and 2013 (Velicogna et al., 2014). The retreat of Antarctic ice shelves and glaciers will impact local, regional and global environmental conditions. At a regional scale, melting glaciers are altering the physico-chemical properties of the seawater in coastal areas, such as along the AP (e.g., Forsch et al., 2021). Globally, large glaciers in subpolar (e.g., Patagonia) and polar regions (e.g., AP) are estimated to be contributing significantly to sea level rise (Zemp et al., 2019; Edwards et al., 2021; Hugonnet et al., 2021).

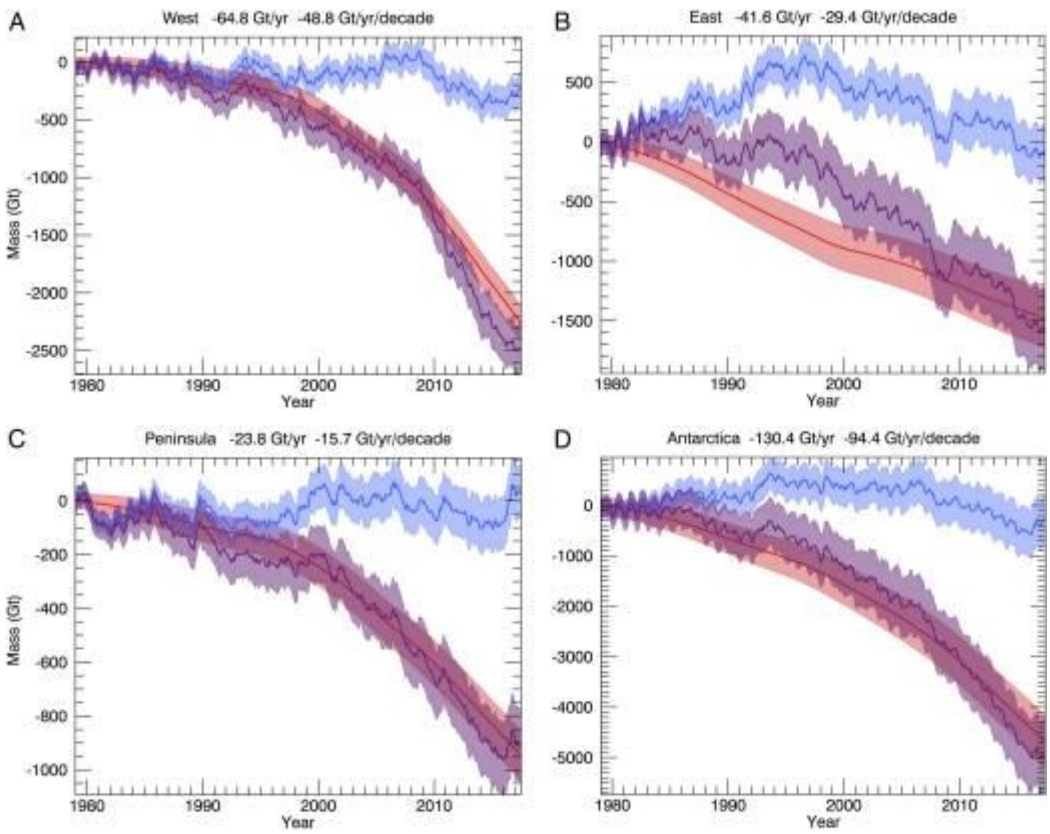

Figure 6. Time series of cumulative anomalies in SMB (blue), ice discharge (D, red), and total mass (M, purple) with error bars in billions of tons for (A) West Antarctica, (B) East Antarctica; (C) Antarctic Peninsula), and (D) Antarctica, with mean mass loss in billions of tons per year and an acceleration in billions of tons per year per decade for the time period 1979 to 2017. The balance discharge is SMB 1979−2008. Note that the total mass change, M = SMB − D, does not depend on SMB 1979−2008. Source: Rignot et al. (2019).

The interannual variability of the glacier SMB, surface melt and runoff of the AP and West Antarctica, and their relationship with the climate has recently been investigated (e.g., Costi et al., 2018; Donat-Magnin et al., 2020; Clem et al., 2022). Donat-Magnin et al. (2020) indicated that the variability of SMB and melting for all the Amundsen glacial drainage basin during summer is controlled by longitudinal migrations of the ASL, with a smaller influence of large-scale climate variability modes, such as ENSO and SAM. Their results reveal two distinct mechanisms controlling SMB and surface melting by the ASL: high summer SMB tends to occur when the ASL is shifted southward and westward, while high summer melt rates tend to occur when ASL is shallower (i.e. anticyclonic anomaly). Furthermore, Clem et al. (2022) indicated that summertime extreme surface melt events on the Larsen C Ice Shelf, in the eastern AP, are triggered by deep convection in the central tropical Pacific, while ENSO and SAM show low correlation with surface melting.

Nevertheless, other studies found concurrences between El Niño events and summer surface melting over West Antarctic ice shelves (Deb et al., 2018; Nicolas et al., 2017; Scott et al., 2019). It is possible that during its positive (negative) phase, ENSO favours positive (negative) SMB in the AP and West Antarctica, due to its relative control over precipitation in these areas (Chen et al., 2023). However, the present climatic control of Antarctic glaciers and ice shelves is under discussion. More detailed studies investigating the complex relationships between large- and regional-scales climate forcing factors with SMB are required.

1.5 Study area and thesis context

The South Shetland Islands (SSI), located in the northern AP, form one of the largest groups of islands around this region. The SSI comprise several islands, such as King George, Livingston, etc. These islands are separated by the Bransfield Strait and the Drake Passage (Fig. 7). According to Silva et al. (2020), the SSI contain 143 glaciers, among land-terminating and tidewater glaciers (70% of the total). Due to its particular location between the two climatic zones of the AP, the SSI mainly present mild and humid marine climate conditions, although on some occasions this region can be influenced by colder continental climate conditions. Furthermore, the local topography of SSI is markedly different compared to the western and northeast AP, and therefore has slightly different temperature-precipitation-wind relationships (e.g., Clem and Fogt 2013; Clem at al., 2016). This region has been also one of the fastest-warming regions on Earth since the 1950s and is also a highly dynamic transitional zone between the subpolar-polar and oceanic-coastal environments (Kerr et al., 2018).

Based on observational data available at the Russian Bellingshausen station for the time period from 1969 to 2020, the annual mean temperature is -1.98 ± 0.83 °C, and the annual accumulation of precipitation is 967±115 mm/yr. Interannual temperature variability across the SSI is predominantly governed by the positioning and intensification/weakening of the ASL (Bello et al., 2021). Conversely, the interannual variability of precipitation seems to be more influenced by mesoscale low-pressure systems originating over the Bellingshausen Sea and traversing the Drake Passage, as noted by Gonzalez et al. (2018). These systems exert their impact on temperature and moisture conditions over the SSI during their passage through the Drake Passage in two distinct ways: when situated to the west, they bring about warm and moist conditions, whereas when positioned to the east, they result in cold and dry conditions over the SSI. Such climatic phenomena are particularly distinctive to the SSI compared to neighbouring regions such as the northeastern and western AP, e.g., precipitation is primarily dictated by westerly winds and local orographic.

Given the importance of glaciers from local to global scales, it is relevant to develop large-term glacier-climate studies to understand glacier changes in the past, present and future and their main climatic controls in more detail. Glaciers are undergoing significant changes worldwide, with retreat and thinning occurring in most of the glacierized regions (Zemp et al., 2019), leading to important environmental impacts at various scales.

Several glaciological studies have been conducted for SSI, utilising remote sensing (e.g., Simões et al., 2004; Rückamp et al., 2010, 2011; Osmanoğlu et al., 2013; Pętlicki et al., 2017; Pudełko et al., 2018; Shahateet et al., 2021), in-situ observations (e.g., Molina et al., 2007; Navarro et al., 2013; Sobota et al., 2015), and modelling (e.g., Bintanja, 1995; Knap et al., 1996; Braun et a., 2001, 2004; Jonsell et al., 2012; Falk et al., 2018). Studies by Navarro et al. (2013) analysed a decade's of SMB data from two glaciers, Hurd and Johnsons, located on Livingston Island on the eastern part of the SSI. Their research compared this data with the available geodetic mass balance records spanning from 1957 to 2020. Their findings revealed a notable deceleration in mass losses from 1957-2000 to 2002-2011, with both glaciers experiencing nearly halved mass losses during the latter period. Shahateet et al. (2021) estimated the geodetic mass balance for all SSI glaciers for 2013 to 2017, providing insights into the local glacier health. Their analysis indicated a slightly negative average specific mass balance, close to equilibrium, for the entire area, with a value of −106 ± 70 mm w.e./year.

The studies mentioned above typically examined short periods, featured low temporal resolution, and, sometimes, focused on individual glaciers. Furthermore, the response of these glaciers to large-scale and regional-scale climate drivers, particularly during the austral winter and in the context of increasingly relevant extreme weather events, like ARs, remains inadequately understood. This limitation results in a constrained comprehension of the current climatic influence on the SMB of the SSI.

Unlike other regions, where investigations have delved into the interplay between glaciers, climate and ARs across regions like the eastern AP and West Antarctica, as outlined in preceding sections. Nonetheless, to the best of our knowledge, there exists no study elucidating the intricate relationship between climate patterns, glacier change, and precipitation on the SSI. This gap can be attributed partly to the scarcity of comprehensive, maily long-term glaciological datasets and the inherent limitations of current global models and reanalysis datasets, which fail to accurately capture these small islands due to their coarse spatial resolution. In this context, this thesis addresses the next scientific question: What are the principal climatic forcing factors shaping the interannual and seasonal variability of the temperature, precipitation, and SMB of the SSI?

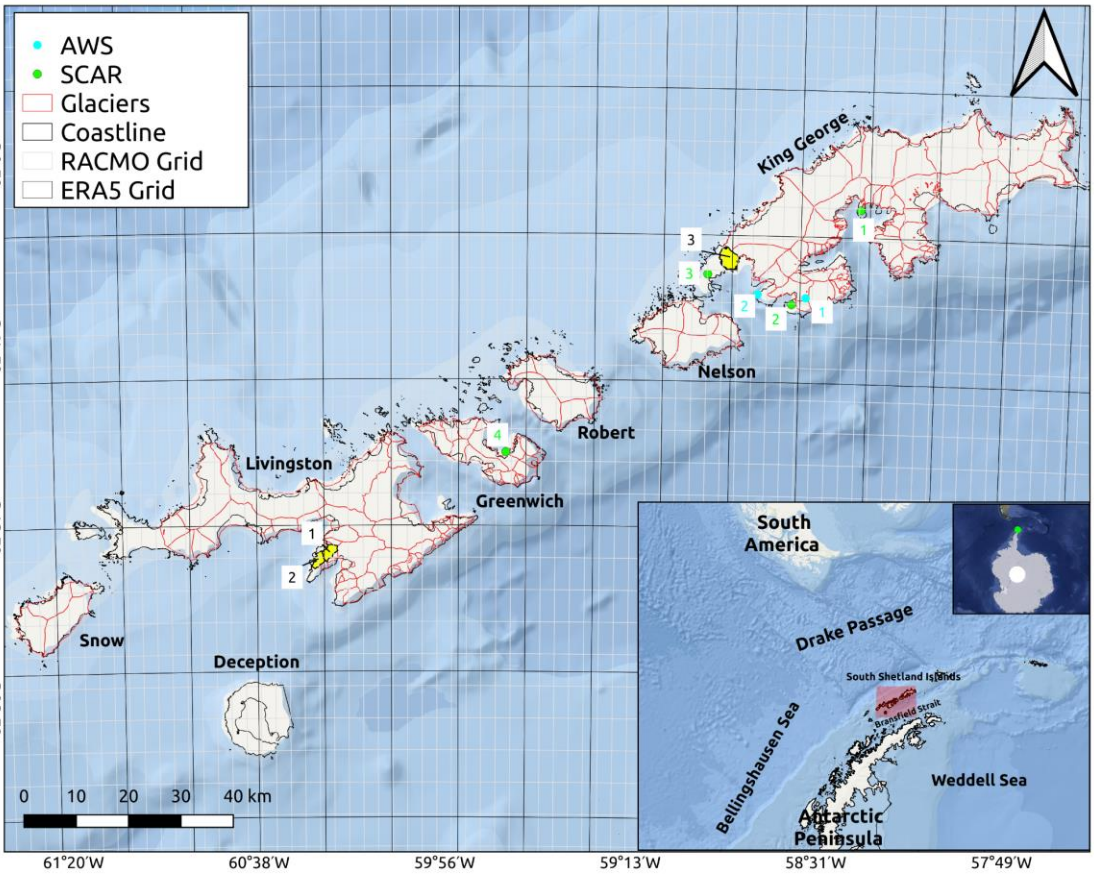

Figure 7. Location map of the South Shetland Islands (SSI), northern Antarctic Peninsula (AP). The green dots indicate the location of the climate READER-SCAR stations from east-west (1) Ferraz (Brazil), (2) Carline (Argentina), (3) Bellingshausen (Russia) and (4) Arturo Prat (Chile). The cyan dots indicate the positions of the two automatic weather stations (AWS), (1) Fourcade and Polar Club Glacier (AWS-FPG) and (2) Korean King Sejong Station (AWS-KKS). The red outlines represent the glacier contours obtained from the Randolph Glacier Inventory, (RGI, 2017). The yellow backgrounds mark the locations of the (1) Johnsons, (2) Hurd and (3) Bellingshausen glaciers. The silver grids indicate the spatial resolution of RACMO (approximately 5.5 km horizontal resolution) and the black grids represent the horizontal resolution of ERA5 (approximately 31 km).

Chapter II: Hypothesis

According to recent studies, described in the introduction, temperature variability over the Antarctic Peninsula and West Antarctica is influenced by both large- and regional-scale climatic forcing factors such as the El Niño-Southern Oscillation (ENSO), the Southern Annular Mode (SAM) and Amundsen Sea Low (ASL). While precipitation and glacier mass balance variability over the same region are controlled by mainly regional-scale forcings like ASL and Drake Low (Drake). Thus, the following hypothesis was tested:

"The interannual and seasonal variability of the temperature, precipitation, and surface mass balance (SMB) of glaciers of the Southern Shetland Islands (SSI) are primarily driven by regional-scale climatic forcing factors, notably the ASL and Drake, with low influence from large-scale climatic modes such as ENSO and SAM."

Chapter III: Objectives

The main objective of this thesis was to assess the influence of the Drake Low and Atmospheric Rivers on glaciers in the South Shetland Islands, Antarctica. The following specific objectives were developed:

- To assess the ability of atmospheric and glaciological models output to represent interannual and seasonal variability of temperature, precipitation and SMB;
- To study the role of climatic forcing factors in the interannual and seasonal variability of local temperature and precipitation;
- To analyse the influence of climatic forcing factors in the interannual and seasonal variability of the local glacier surface mass balance.

Chapter IV: Material and Methods

In this section, we describe the datasets, glaciological models, and statistical techniques used for the development of the thesis. As the following chapters (chapters V and VI) are individually published or submitted papers, they each contain methodology sections that describe data and methods as relevant to the specific study. This section will summarise the methodology sections of the two papers.

4.1 In-situ observation and reanalysis datasets

4.1.1 Meteorological observation

We used different meteorological/climatic datasets during the development of this thesis. We selected four conventional weather stations located on the SSI, where temperature and precipitation were recorded. Monthly temperature data were obtained from the Scientific Committee on Antarctic Research (SCAR) READER project (https://legacy.bas.ac.uk/met/READER/surface/stationpt.html). Precipitation data with daily resolution was obtained directly from the website of the Bellingshausen Russian Station (http://www.aari.aq/stations/bell/bell_en.html).

In addition, we used meteorological data from two automatic weather stations (AWS). Various hourly atmospheric variables are available from the Fourcade and Polar Club Glacier station (FPG-AWS), such as incoming shortwave radiation (SWin), incoming longwave radiation (LWin), air temperature at 2 m (T2), relative humidity at 2 m (RH2), wind speed at 2 m (WS), surface pressure (PSFC) and total precipitation (TP) from November 2010 to May 2016. The second dataset was also collected with an AWS installed at the Korean King Sejong Station (KKS-AWS). This station also provides various atmospheric variables available daily, such as SWin, T2, HR2, WS, PSFC and TP from January 1996 to December 2020. The locations of the manned weather stations and the AWSs are shown in Fig. 7. Table 1 provides information on their location, country and data period of availability.

Table 1. List of weather stations considered in the study.

Station	Operation nation	Available data	Variables	Lat.	Lon.	Ele (m)
Bellingshausen	Russian Federation	1968-2020	T2, PREC	62.20° S	58.97° W	16
Ferraz	Brazil	1986-2005	T2	62.10° S	58.40° W	20
Carlini	Argentina	1986-2020	T2	62.24° S	58.67° W	4
Arturo Prat	Chile	1966-2020	T2	62.50° S	59.70° W	5
AWS-FCG	Argentina	2010-2015	T2, PREC, RH2, PSFC, WS, SWin, LWin	62.24° S	58.61° W	195
AWS-KKS	Korea	1996-2020	T2, PREC, RH2, PSFC, WS, SWin	62.23° S	58.77° W	11

4.1.2 Glaciological in-situ observations

Very few glacier-monitoring programs are available on the SSI (Navarro et al., 2023). There is only one long-term program over this region, collecting data on two glaciers, Johnsons and Hurd, from 2002 to the present. Glacier-wide SMB data are freely available through the World Glacier Monitoring Service (WGMS) on seasonal and annual time scales. Additionally, other short-term (i.e., <5 years of monitoring) programs are available, such as for Bellingshausen Glacier from 2007 to 2012. We used these annual SMB data for the Johnsons, Hurd and Bellingshausen glaciers (Fig. 8) to calibrate and validate two glaciological models to reconstruct the SMB of these glaciers from 1969 to 2020.

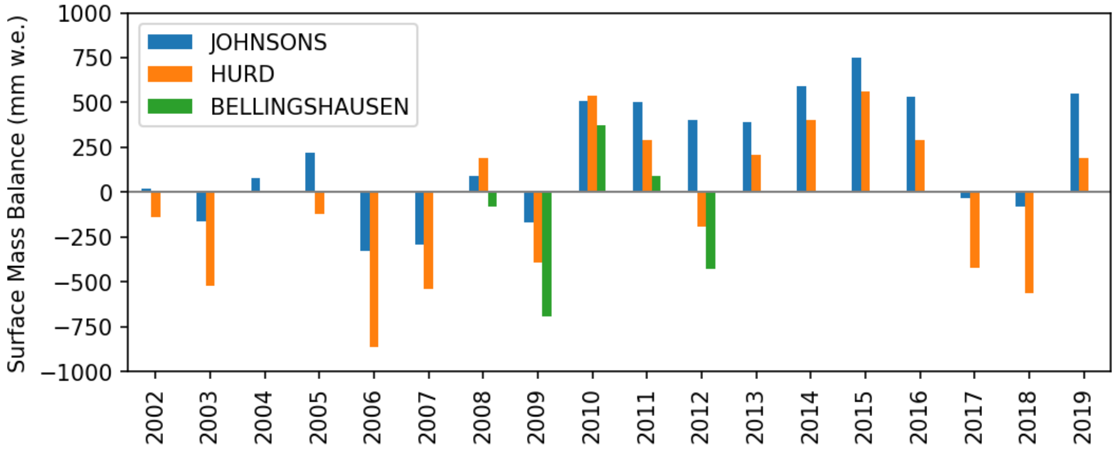

Figure 8. In-situ observation of annual surface mass balance at Johnsons (blue), Hurd (orange), and Bellingshausen (green) glaciers. Data was obtained from World Glacier Monitoring Service - WGMS (last access, 23 November 2022).

4.1.3 ERA5 and RACMO datasets

We also used atmospheric and oceanic data from the ERA5 reanalysis produced by the European Centre for Medium-range Weather Forecasts (ECMWF) (Hersbach et al., 2020). ERA5 is provided on a regular latitude-longitude grid of approximately 31 km at hourly and monthly time resolutions from 1940 to the present. Both ERA5 hourly and monthly products are available at the Copernicus Climate Data Store (https://cds.climate.copernicus.eu). We used hourly SWin, LWin, T2, PSFC, RH2, WS, total precipitation and snowfall from 1969 to 2020 to force glaciological models. Furthermore, we used monthly mean sea level pressure (MSLP), zonal (U) and meridional (V) wind, and geopotential height (Z) at different pressure levels, outgoing longwave radiation (OLR), SIC and SST to represent present atmospheric and oceanic conditions from 1969 to 2020.

Furthermore, we use monthly temperature and precipitation data available by van Wessem et al. (2018; https://zenodo.org/records/7961733). This is a data set of monthly averaged variables simulated by the hydrostatic regional atmospheric climate model RACMO2.3p2 over the AP. At the lateral and ocean boundaries, the model is forced by ERA-Interim reanalysis data every 6 hours from January 1979 to August 2019. After August 2019, the model is forced by ERA5 reanalysis every 3 hours, with an overlap from 2016 to December 2022. The model is run at a horizontal resolution of 5.5 km and 40 vertical levels for the AP domain, which after 2018 constitutes an update of the simulation forced from 1979-2018 by ERA-Interim reported in van Wessem et al. (2018).

A comparison of the annual climatology (1979-2019) of spatially distributed temperature and precipitation is shown in Fig. 9. Due to its high-spatial resolution, RACMO captures the low temperatures over the SSI. Furthermore, the precipitation fields are better represented in RACMO (Fig. 9d) with values up to 2700 mm w.e./year over the high elevation, while ERA5 does not represent such features (Fig. 9c).

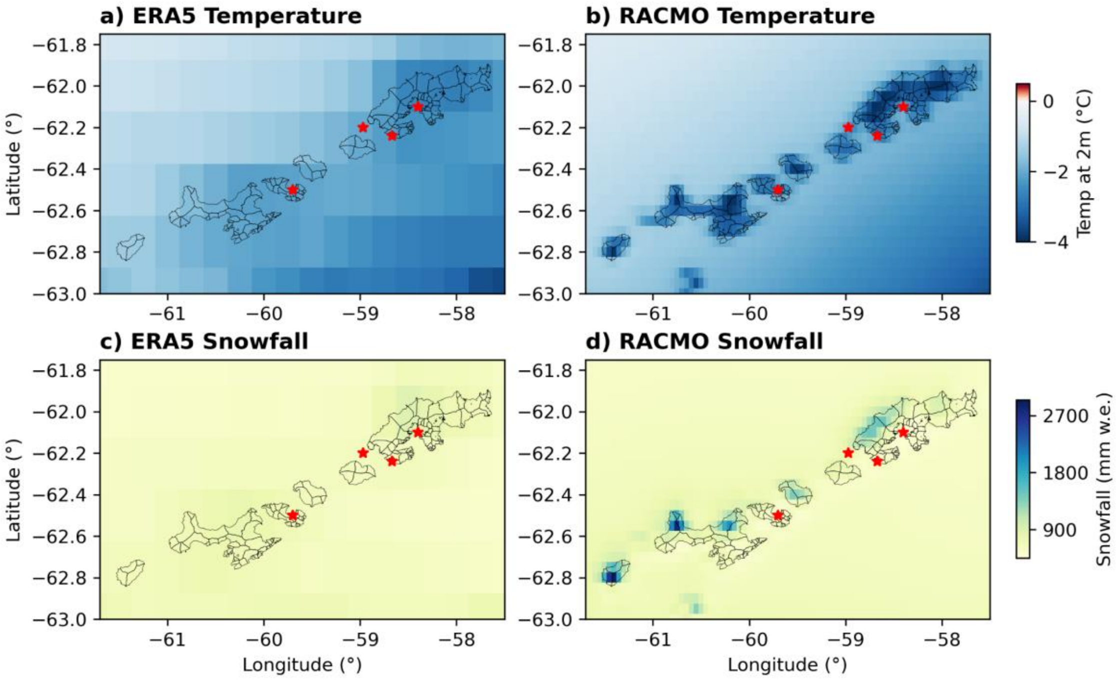

Figure 9. Annual mean temperature at 2 m (a) ERA5 and (b) RACMO, and annual total snowfall (c) ERA5 and (d) RACMO for the time period 1980-2019. Weather stations (i.e., Ferraz, Carline, Bellingshausen and Arturo Prat) are indicated by the red asterisk. The back outlines represent the glacier contours obtained from the Randolph Glacier Inventory, (RGI, 2017).

4.2 Glaciological models

4.2.1 PPD model

PDD is a simple model based on the empirical relationship between temperature and surface melting of snow/ice (Braithwaite, 1995). This model has been widely used to estimate the glaciers surface melt and runoff, ice fields and ice shelves on the AP (e.g., Vaughan, 2006; Costi et al., 2018). In this study, the SMB using PDD is derived considering accumulation and surface melting processes, as described in equation 1.

$$SMB = ACCUM + \frac{1}{n} \times DDice \times PDD + DDice \times PDD \quad (1)$$

Accumulation (ACCUM) is summed directly as solid precipitation (i.e., snowfall). The melt component (DDice * PDD + DDsnow * PDD) is calculated by multiplying the sums of positive temperatures over a specific period (here n = 8 hours) by snow (DDsnow) and ice (DDice) melting factors. Here, the temperature threshold above which melt occurs is

0°C (Costi et al., 2018). We used the same routine with the PDD model that was made available by Temme et al. (2023). This routine was used by these authors to model the mass balance at the Monte Sarmiento Massif, Tierra del Fuego.

4.2.2 COSIPY model

COSIPY is a multi-layer physical model based on the SEB (Sauter et al., 2020) approach. The SEB model combines all energy fluxes impacting the glacier surface energy budget, i.e., SWin, surface albedo (ALBEDO), LWin and outgoing longwave radiation (QLWout), turbulent sensible (QH) and latent (QLE) heat fluxes, ground heat flux (QG), and rain heat flux (QRain). QSWin and QLWin can be provided in the input data, whereas QLWout, QH, QLE, QG and QRain are derived by solving the heat equation (Sauter et al., 2020). This model is widely used in several glaciological studies worldwide due to its user-friendly implementation and free access. COSIPY considers various accumulation and ablation processes to estimate the SMB at high temporal resolution (hourly), following equation 2.

$$SMB = ACCUM + MELT + SUB + DEP + EVA + subMELT + REFRE \quad (2)$$

We calculated the SMB, which considers accumulation (ACCUM), melting (MELT), sublimation (SUB), deposition (DEP) and evaporation (EVA), subsurface melting (SubMELT) and refreezing (REFRE). These components are determined from the available energy, resulting from the SEB, which integrates solar and atmospheric radiation, albedo, turbulent heat fluxes, ground heat and heat from rainfall. In COSIPY, the discharge is assumed to be the sum of the total water percolating through the snow/ice cover due to melting, condensation, and moisture content. More detailed information on COSIPY and its physical parameterisations can be found in Sauter et al. (2020).

4.2.3 RACMO model

Additionally, we incorporated monthly SMB data from RACMO for comparison with our simulations. RACMO is a regional high spatial resolution atmospheric and glaciological product available for the entire AP at a 5.5 km horizontal resolution from 1979 to the present (van Wessem et al., 2016, van Wessem et al., 2018). RACMO outputs are used to force a glaciological firn densification model (FDM). The SMB in that FDM is calculated considering accumulation, melting, drifting snow and runoff processes, following equation 3.

$$SMB = PR - SU - SUs - SUds - ERds \quad (3)$$

where PR represents total precipitation (snowfall plus rain), SU denotes surface (SUs) plus drifting snow (SUds) sublimation, ERds corresponds to drifting snow erosion/deposition (caused by divergence/convergence in the horizontal drifting snow flux) and RU stands for meltwater runoff, the amount of liquid water (melt and rain) that is not retained or refrozen in the snowpack. More details on the FDM can be found in Ligtenberg et al. (2011). van Wessem et al. (2016) and van Wessem et al. (2018) found that while RACMO realistically simulates the strong spatial precipitation variability, significant biases remain as a result of the highly complex topography of the AP.

4.3 Methodology

4.3.1 Obtaining time series for weather stations from ERA5 and RACMO

Some pre-processing steps were applied to the ERA5 and RACMO datasets. First, the ERA5 or RACMO point of the grid closest to each weather station (see Fig. 9) was selected to obtain the hourly or monthly temperature time series. Next, a bias correction was applied to the temperature data using a constant temperature lapse rate of -1.0°C/100 m for ERA5 and -1.2°C/100 m for RACMO. We use different temperature lapse rates for ERA5 and RACMO because they better reduce the root-mean-square errors (RMSE) at each SCAR station. Finally, in the case of ERA5, hourly temperatures were temporally averaged into daily and monthly time scales. In the case of precipitation, as we only have one weather station with complete and consistent precipitation data, also of only grid select, we selected all ERA5 or RACMO grids that cover the entire SSI. This allows us to have a better spatial representation of precipitation for the entire SSI. Finally, in the case of ERA5, the hourly data were summed to obtain the monthly cumulative precipitation.

A comparison of the time series between the points of the grid closest to the weather stations and all grid covering the SSI showed no significant differences in both ERA5 and RACMO. This indicates that ERA5 and RACMO do not show large spatial variability in precipitation fields for the entire SSI. Therefore, we used the ERA5 and RACMO precipitation time series obtained from the spatial average of the whole grid covering the SSI.

4.3.2 Bias correction of ERA5

To facilitate comparisons with in-situ observations and to force our glaciological models, we carried out pre-processing steps on ERA5 data. First, we applied a bias correction to ERA5 data at the precise locations of the AWS-FPG and AWS-KKS meteorological stations. Second, we also applied a bias correction to the forcing variables at the centroid (Fig. 10) of each of the three glaciers (Johnsons, Hurd and Bellingshausen) to force the PDD and COSIPY models.

The bias correction pre-processing involved T2, dewpoint temperature (T2D), PSFC and WS. For T2 and T2D, a temperature lapse rate was used to adjust the ERA5 T2 (1 °K/100

m) and T2D (0.9 °K/100 m) to values corresponding to the AWS and glaciers' centroid elevations. These temperature lapse rates showed a better fit than those observed at AWS-FPG (see Figs. S1, S2 and S3 of the supplementary material of Chapter VII). Likewise, the ERA5 PSFC was adjusted to a value corresponding to the AWS and glaciers centroid elevations, using the barometric equation S1 in the supplementary material of Chapter VII. The WS at ERA5, initially at 10 meters was adjusted to 2 m using the logarithmic wind profile, equation S2 in supplementary material of Chapter VII. Finally, SWin, LWin, snowfall and total precipitation were obtained directly from ERA5 to compare and force glaciological models. Several studies indicated that the ERA5 dataset provides the most accurate depiction of the recent Antarctic climate (e.g., Gossart et al., 2019; Tetzner et al., 2019; Bozkurt et al., 2020; Hillebrand et al., 2021).

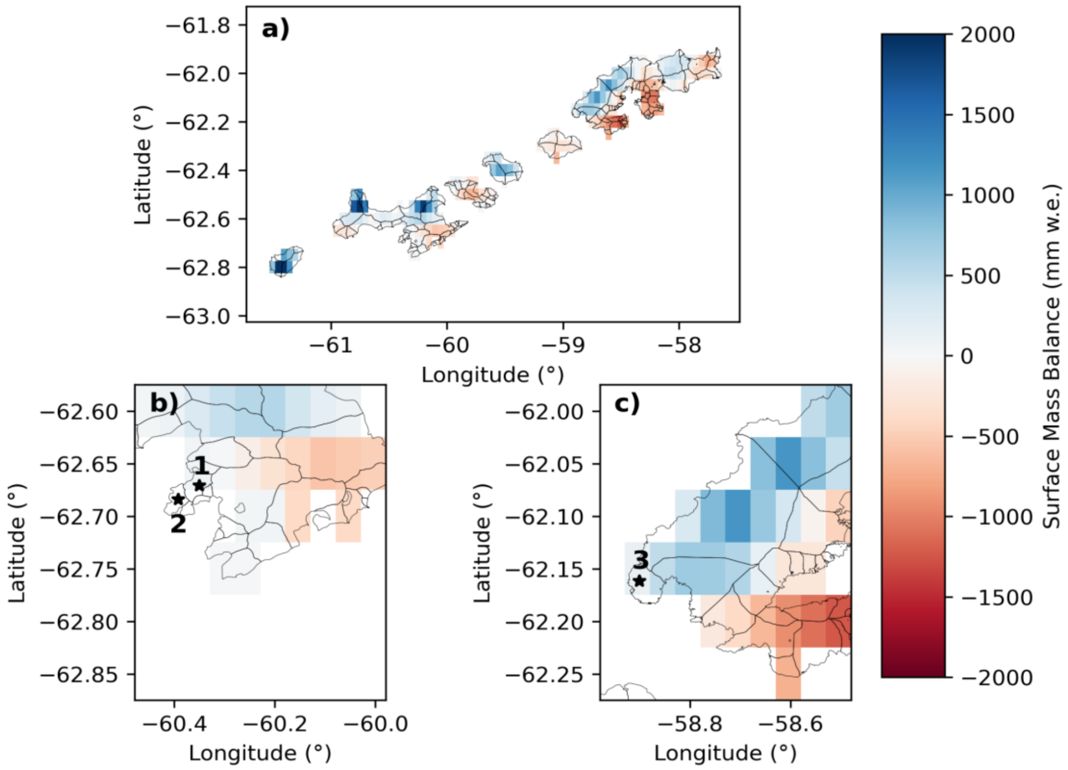

Figure 10. Annual mean surface mass balance over (a) the entire South Shetland Islands glaciers, (b) zoomed for the Johnsons and Hurd glaciers, and (c) zoomed for the Bellingshausen glacier. Data was obtained from RACMO 5.5 km for the time period 1980-2019. Black asterisks indicate the centroid of glaciers with in-situ surface mass balance observations (i.e., (1) Johnsons, (2) Hurd, and (3) Bellingshausen Glaciers). The back outlines represent the glacier contours obtained from the Randolph Glacier Inventory, (RGI, 2017).

4.3.3 Glaciological modelling

Both glaciological models (PDD and COSIPY) were configured at a single point since a single ERA5 grid covers the entire glacier area. The average elevation for each glacier was obtained using the glacier outlines available from the Randolph Glacier Inventory (RGI, 2017) and a new high-resolution digital elevation model (DEM) from the gapless 100-m Reference Elevation Model of Antarctica (Gapless-REMA100) as provided by Dong et al. (2022). To force the glaciological models, climate variables were extracted from the nearest ERA5 grid point for each glacier and averaged (SWin, LWin, T2, RH2, WS and PSFC) or summed (total precipitation and snowfall) over six-hour time steps. Therefore, the glaciological models were run at six-hour intervals to manage computational demands.

PDD requires only two atmospheric variables as input (temperature and precipitation or snowfall) and has very few free parameters requiring calibration. In contrast, COSIPY demands several atmospheric variables as input (SWin, LWin, T2, RH2, PSFC, WS, and total precipitation and/or snowfall) and entails the calibration for multiple free parameters.

In both PDD and COSIPY, accumulation is directly derived from snowfall from ERA5, eliminating the need for free parameters like temperature thresholds commonly used to distinguish between solid and liquid precipitation in total precipitation. Additionally, snowfall in ERA5 is already provided in mm water equivalent (w.e.) and does not require conversion using snow/ice density, thus avoiding the use of density parameters. T2, RH2 and PSFC underwent a bias correction (see Sect. 3.2), adjusting for the average-elevation of each glacier. SWin, LWin, snowfall and total precipitation are also directly obtained from ERA5 without prior preprocessing. Several studies have employed these downscaling strategies to drive long-term glaciological models (e.g., Weidemann et al., 2018; Arndt et al., 2021; Temme et al., 2023). Finally, these three atmospheric datasets of each glacier were used in the experiment simulations.

PPD and COSIPY were optimized using a Randomized Grid Search (RGSearch) technique (e.g., Bergstra and Bengio, 2012). RGSearch, widely used in machine learning, combines Grid Search and Random Search. Instead of evaluating all possible combinations, it randomly samples a specified number of combinations from the free parameters space. Therefore, the free parameters of both PDD and COSIPY were varied randomly within their specified ranges (see Table S2) over 1000 model runs, similar to Mölg et al. (2012). The optimal combination of parameters was that with the minimum RMSE between the observed and modeled SMB during the period calibration (from 2002 to 2011). The validation of the simulations was carried out using an out-of-sample dataset from 2012 to 2019. In PDD, we focused solely on calibrating two free parameters, the DDF_{ice} and DDF_{snow} melt factors. In contrast, for COSIPY, we focused on eight key free parameters associated with the physical parameterization schemes of surface albedo and roughness.

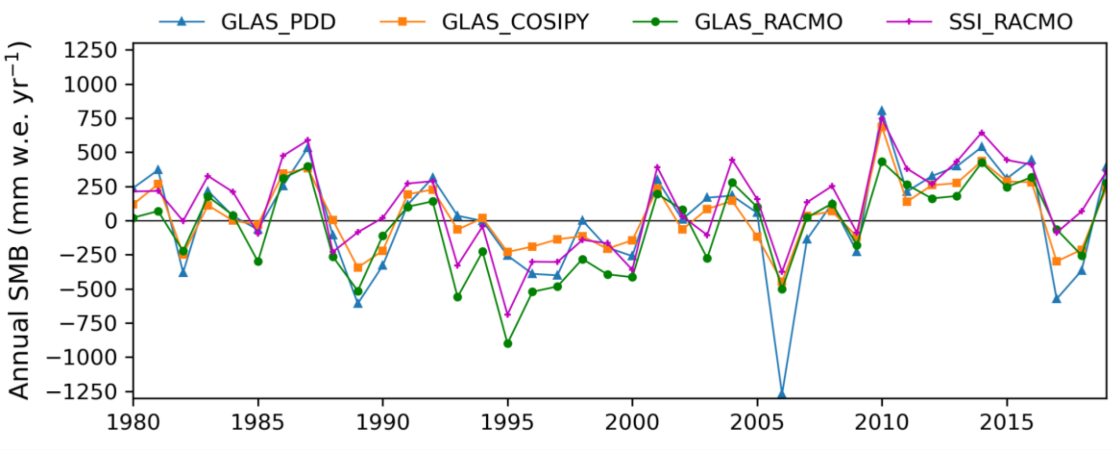

Figure 11. Annual surface mass balance intercomparison reconstruction from three glaciological models (blue line PDD model, orange line COSIPY model, green and magenta lines RACMO model). Both PDD and COSIPY models were forced using the global reanalysis ERA5-downscaled.

Figure 11 shows the annual SMB estimated by the different glaciological models configured and/or selected at a single point for the average of the three glaciers from 1980 to 2019. The same figure also shows the averaged SMB for the whole grid overlaying the SSI (see Fig. 10a). To clarify, GLAS_PDD and GLAS_COSIPY correspond to the average of the three glaciers configured at a single point modelled with PPD or COSIPY, respectively. GLAS_RACMO corresponds to the average of the three glaciers selected from the grid nearest each glacier. SSI_RACMO corresponds to the average of all grids overlapping the SSI. In general, all glaciological models show similar interannual variability of the SMB, with high significant correlations. Even when comparing SSI_RACMO (magenta line) with GLAS_PDD (blue line), GLAS_COSIPY (orange line) and GLAS_RACMO (green line), the correlation is highly significant (see Table 2). This indicates that the RACMO model captures the SMB of the SSI with little spatial variability. Furthermore, the configuration of the glaciological model (i.e., single point or distributed) has little influence on the final result of the interannual variability of the averaged SMB. The low spatial variability in the modelling outputs can be explained by the fact that the models used here do not include processes associated with glacier dynamics such as the calving of tidewater glaciers.

Table 2**.** Annual SMB correlation for each time series estimated with different glaciological models (i.e., PPD, COSIPY, and RACMO) from 1980 to 2018. Significance is indicated by an asterisk, where ** ($p<0.05$).

	GLAS_PDD	GLAS_COSIPY	GLAS_RACMO	SSI_RACMO
GLAS_PDD	-	0.95**	0.83**	0.83**
GLAS_COSIPY	-	-	0.84**	0.84**
GLAS_RACMO	-	-	-	0.96**
SSI_RACMO	-	-	-	-

4.3.4 Atmospheric modelling

We utilised the Polar Weather Research and Forecasting (PWRF) model, version 3.9.1, to generate high-resolution atmospheric data for the SSI. Our setup consists of three nested domains spatial resolutions of 15, 5 and 1 km with a one-way nesting approach on a polar stereographic projection. For our simulation domain, we incorporated the updated Reference Elevation Model of Antarctica (REMA) from Dong et al. (2021). We used updated REMA (Dong et al., 2021) because in standard REMA (Howat et al., 2019) there is missing data for the eastern part of the SSI. The ERA5 reanalysis released by ECMWF was used for the PWRF model initialization and input of the boundary conditions at six-hours intervals. The modelling experiment was tested for one summer (January) month in 2013. The physics options employed throughout this study were obtained from Bozkurt et al. (2020), which include the rapid radiative transfer model for general circulation models (RRTMG), the Noah-MP land-surface model, the Mellor-Yamada-Janjic (MYJ) boundary layer and the Grell-Freitas Ensemble (GFE) cumulus schemes.

4.3.5 Large-, synoptic-, and regional- scale climate indices and AR data

The ENSO indices (such as El Niño 3, 3.4 and 4 regions) were obtained from the National Oceanic and Atmospheric Administration Climate Prediction Center (https://www.cpc.ncep.noaa.gov/) to assess potential tropical-polar teleconnections. We also constructed a customized climatic index DC-CPAC with a large-scale perspective, using a sector delineated in the central tropical Pacific (10–15°S, 170–165°W, see the pink box in Fig. 12) by Clem et al. (2022) to obtain a monthly time series of the area-averaged Outgoing Longwave Radiation (OLR). Recent studies have indicated that deep convection in the central tropical Pacific region triggers ARs making landfall at the AP (e.g., Clem et al., 2022).

The SAM and ASL are the large- and synoptic-scale atmospheric circulation which influence the climate changes in the AP. The SAM is characterized by pressure variability between the mid and high southern latitudes, influencing the strength and position of the midlatitude jet. ASL is a climatological low-pressure center located over the southern end of the Pacific Ocean, off the coast of West Antarctica. Both SAM (https://legacy.bas.ac.uk/met/gjma/sam.html; monitored using Marshall's (2003) observation-based index) and ASL (https://climatedataguide.ucar.edu/climate-data/amundsen-sea-low-indices) were obtained from National Center for Atmospheric Research Climate Data Guide.

In addition to the large- and synoptic-scale indices, we constructed regional-scale climate indices over three key sectors: the Drake Passage (hereafter Drake; aqua box in Fig. 12), the Amundsen-Bellingshausen Sea (hereafter ABSea; magenta box in Fig. 12) and the Weddell Sea (hereafter WSea; blue box in Fig. 12), which directly are associated with the climate in the SSI. Monthly time series of SIE and SST are obtained from ABSea and WSea as area-averaged due to their strong relationship with temperature in SSI (Torres et al., 2023).

We identified the Drake Passage (85°W-40°W, 62.5°S-55°S, aqua box in Fig. 12) from west to east with significant correlations between SMB and Z500 during winter, annual and summer timescales, respectively. From this region, monthly time series of MSLP, Z500, T500 and SST were obtained as area-average. This sector was also contrasted with previous studies indicating the different low-pressure systems over the AP and their associated impacts on temperature and precipitation phase (rainfall and snowfall) (Gonzalez et al., 2018; Wang et al., 2021; Torres et al., 2023).

All atmospheric and oceanographic variables (i.e., ORL, MSLP, Z500, T500, SST, SIE) used to construct our large and regional indices were obtained from the monthly ERA5 reanalysis dataset. Then, the monthly anomaly of each variable was calculated independently. The last procedure is also applied for ASL since we used the area-average sea level pressure over the sector (170°E-298°E, 60°S-80°S) defined by Hosking et al. (2016).

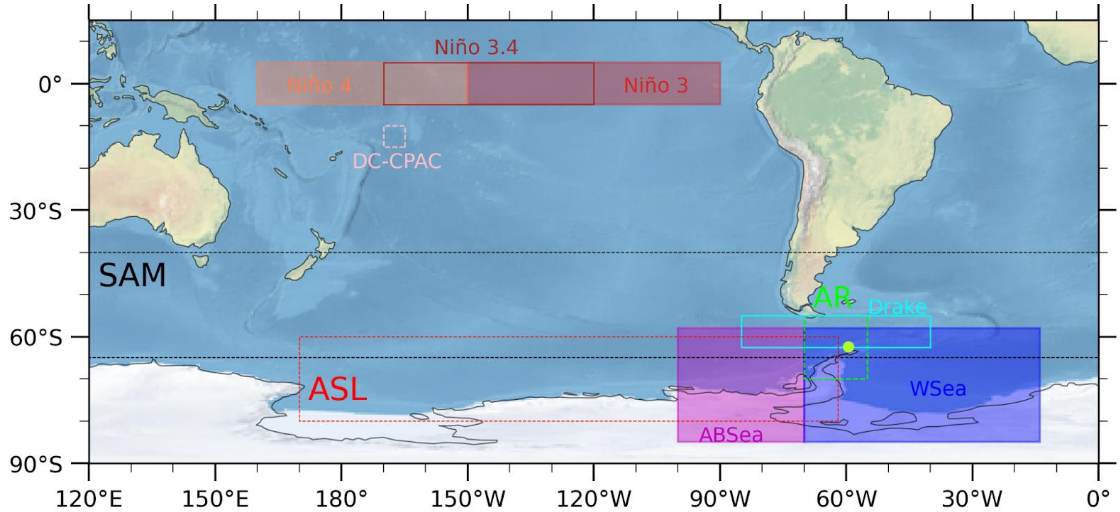

Figure 12**.** Regions used for the construction of climate indices. The green dot indicates the location of the SSI. Amundsen-Bellingshausen (100-70°W; 85-55°S) and Weddell (70-14; 85-55°S) Seas regions limits were obtained from Fogt et al. (2022). Deep convection over the central tropical Pacific (170W-165W; 15S-10S) region limit was obtained from Clem et al. (2022). ASL limit (170°E-298°E, 60°S-80°S) was obtained from Hosking et al. (2016). Drake region (85°W-40°W; 62.5°S-55°S) was obtained from correlation analysis between winter, annual and summer SMB and Z500. The lime dashed box (70°W-55°W; 55°S-70°S) indicates the area where the ARs frequency is selected and area-averaged.

Finally, AR frequency was used to evaluate its impact on the glaciers over the SSI. AR frequency data were obtained from state-of-the-art AR tracking databases (1979-2018) available from Guan and Waliser (2019). Monthly time series for AR frequency were constructed for the area of 50W-80W and 55S-75S (green dashed box in Fig. 12). The AR frequency was calculated independently for each grid cell within the box by counting the number of 6-hourly time steps with AR conditions (i.e., grids within detected AR shape boundaries) and dividing by the total number of 6-hourly time steps during the analysis period. The AR frequency is expressed in units of days (i.e., one 6-h AR step = 0.25 days).

4.3.6 Statistical evaluation and analysis

Glaciological and atmospheric modelling were validated with in-situ observations using three commonly used statistical measures: (1) Pearson's or Spearman's coefficient (r), (2) bias (Bias) and (3) root mean squared error (RMSE).

To analyse the relationship between temperature, precipitation and SMB with climate conditions, we used Pearson correlation analysis and linear regression. Trend was analysed using Mann-Kendall test. In all statistical test analyses, a significance level of 95% and 90% was used.

Chapter V: Large-scale and regional climatic influences on surface temperature and precipitation in the South Shetland Islands, northern Antarctic Peninsula

This chapter contains the first scientific article published from this thesis, authored by Christian Torres, Deniz Bozkurt and Jorge Arigony-Neto, and entitled "**Large-scale and regional climatic influences on surface temperature and precipitation in the South Shetland Islands, northern Antarctic Peninsula**". This paper was published in the special edition of "Anais da Academia Brasileira de Ciências" Journal (https://doi.org/10.1590/0001-3765202320230685). The original format of the paper has been changed for better indexing and understanding of the thesis.

Large-scale and regional climatic influences on surface temperature and precipitation in the South Shetland Islands, northern Antarctic Peninsula

Christian Torres[1,2,*]; Deniz Bozkurt[2,3,4]; Jorge Arigony-Neto[1]

[1] Institute of Oceanography, Universidade Federal do Rio Grande, Brazil
[2] Department of Meteorology, University of Valparaíso, Chile
[3] Center for Climate and Resilience Research (CR)2, Santiago, Chile
[4] Center for Oceanographic Research COPAS COASTAL, Universidad de Concepción, Chile

* christian010194@gmail.com

5.1 Abstract

Using data from SCAR observations, ERA5 reanalysis, and regional climate model simulations (RACMO), we examined the influence of large- and regional-scale climate forcing on temperature and precipitation variations in the South Shetland Islands (SSI). Specifically, we focused on understanding how regional climate indices influence the temporal variability of temperature and precipitation on the SSI. Our findings indicate that both large- and regional-scale climate indices significantly impact the interannual and seasonal temperature variability in the SSI. For instance, the Amundsen Sea Low, characterised by low-pressure systems over the Amundsen Sea, and sea ice extent in the northwestern part of the Weddell Sea, exert a strong influence on temperature variability (r from -0.64 to -0.87; $p < 0.05$). In contrast, precipitation variability in this region is primarily controlled by regional climatic indices. Particularly, anomalies in atmospheric and surface pressure over the Drake Passage region strongly regulate the interannual variability of precipitation in the SSI (r from -0.46 to -0.70; $p < 0.05$). Large-scale climatic indices demonstrate low but statistically significant correlations, including the Southern Annular Mode and deep convection in the central tropical Pacific. Given the importance

of temperature and precipitation in the glacier changes, we recommend assessing the impact of the Drake region on SSI glaciers.

Key words: Temperature, Precipitation, Drake Passage, South Shetland Islands.

5.2 Introduction

Significant changes in key atmospheric variables, such as temperature and precipitation, have been reported over the Antarctic Peninsula (AP) in recent years. Turner et al. (2016) reported a significant warming trend of 0.32 °C/decade over the AP from 1979 to 1997, accompanied by a cooling period (-0.47 °C/decade) between 1999 and 2014 attributed to internal climate variability. More recently, Carrasco et al. (2021) indicated that this warming pause came to an end in the mid-2010s and in another study, the AP is projected to warm for the next two decades (Bozkurt et al. 2021). Carrasco & Cordero (2020) also showed significant increases in precipitation (+16 mm/decade) over the northern AP during the last decades (1970-2020). In addition, Bozkurt et al. (2021) projected positive trends in both temperature and precipitation for the next two decades across the entire AP. Changes in temperature and precipitation are causing significant negative and positive impacts on the cryosphere. For instance, Oliva et al. (2017) indicated positive mass balance in several glaciers located in northern AP from 2006 to 2012, which was apparently associated with a cooling period over the region. Yet, the overall long-term warming trend has caused abrupt negative changes in the Peninsula's cryosphere (e.g., Sobota et al. 2015, Pudełko et al. 2018, Silva et al. 2020, Shahateet et al. 2021).

Recent studies have analysed the impact of large- and regional-scale climate forcing factors on temperature and precipitation over the AP region. For example, Turner et al. (2020) reported that the interannual and seasonal variability of temperature over the AP is influenced by major climate modes such as the El Niño-Southern Oscillation (ENSO) and Southern Annular Mode (SAM). Similar results were reported for King George Island, located north of the AP by Bello et al. (2022). Carrasco & Cordero (2020) showed that observed monthly precipitation over the northern AP shows statistically non-significant correlations with main climate indices such as ENSO, SAM and Amundsen Sea Low (ASL), indicating that these climate indices have a low influence on precipitation in the region. Gonzalez et al. (2018) indicated that a low-pressure atmospheric circulation system over the Drake Passage strongly influences precipitation over Livingston Island, located north of the AP. Recently, Clem et al. (2022) reported that strong deep convection anomalies in the central tropical Pacific (DC-CPAC) drive high temperatures and surface melt over the Larsen C Ice Shelf located in the eastern part of the AP.

The South Shetland Islands (SSI), located in the northern AP, has been one of the fastest warming regions on Earth since the 1950s and serve as a highly dynamic transitional zone between the subpolar-polar and oceanic-coastal environments (Kerr et al. 2018). The SSI is influenced by different atmospheric forcing from regional (cyclonic and anticyclonic circulations) to global (SAM, ENSO and DC-CPAC) scales (e.g., Marshall & King 1998, Gonzalez et al. 2018, Turner et al. 2016, 2020, Bello et al. 2022, Clem et al. 2022, Marín et al. 2022, Bozkurt et al. 2022). This region is also influenced by different regional oceanic forcing factors, including sea ice extent-concentration, sea surface temperature, and ocean circulation, encompassing the Bransfield Strait, the Amundsen-Bellingshausen, Drake Passage and Weddell Seas regions (Cook et al. 2016, Kerr et al. 2018). While the role of large-scale climate indices on temperature and precipitation variability has been well studied, the influence of regional-scale climate forcing factors on both temperature and precipitation in this region remains relatively unexplored. In this study, we, therefore, aim to enhance our understanding of how regional climate indices, constructed from anomalies of atmospheric and oceanographic variables in three key regions, impact the interannual and seasonal variability of temperature and precipitation over the SSI. We also examined the temporal variability of the temperature and precipitation in this region over the last four decades (1980-2020). The key contribution of this study is a comprehensive understanding of the role of atmospheric and oceanic forcing factors across three key regions that influence environmental conditions in the SSI, namely the (1) Drake Passage, (2) Amundsen-Bellingshausen, and (3) Weddell Sea regions. By analyzing the impact of these factors on temperature and precipitation variability, we can advance our knowledge of the complex climatic dynamics in this region.

5.3 Materials and Methods

5.3.1 Study area

The SSI comprise several islands such as King George, Livingston, etc. These islands are located north of the AP and separated by the Bransfield Strait and the Drake Passage (Fig. 13). The climate of these islands is heavily influenced by maritime climatic conditions (Falk et al. 2018) due to their small size and geographical location. Based on the observational data available at the Russian Bellingshausen station, the annual mean temperature is -1.98 ± 0.83 °C, and the annual accumulation of precipitation is 967 ± 115 mm/yr.

5.3.2 Climatological in-situ observations and modelling

Monthly air temperature observations for several climatological stations in Antarctica are available through The Scientific Committee on Antarctic Research (SCAR) READER (https://legacy.bas.ac.uk/met/READER/surface/stationpt.html). For this study, we selected four climatological stations (Bellingshausen, Ferraz, Carlini and Arturo Prat) located on the SSI. Figure 13 shows the station and Table 3 presentes their names, locations, altitudes, and periods of available data. The selection of these stations was based on the period of available data and their geographic distribution. For instance, Ferraz station is located on the eastern part, while Arturo Prat station is located on the western part of the SSI. This selection allows us to capture the spatial variability of local temperature on the SSI. These data were extensively used to analyse the temporal variability and trends of air temperature in the region and its relationship with large-scale climate forcings (e.g., Turner et al. 2016, 2020, Oliva et al. 2017, Bello et al. 2022).

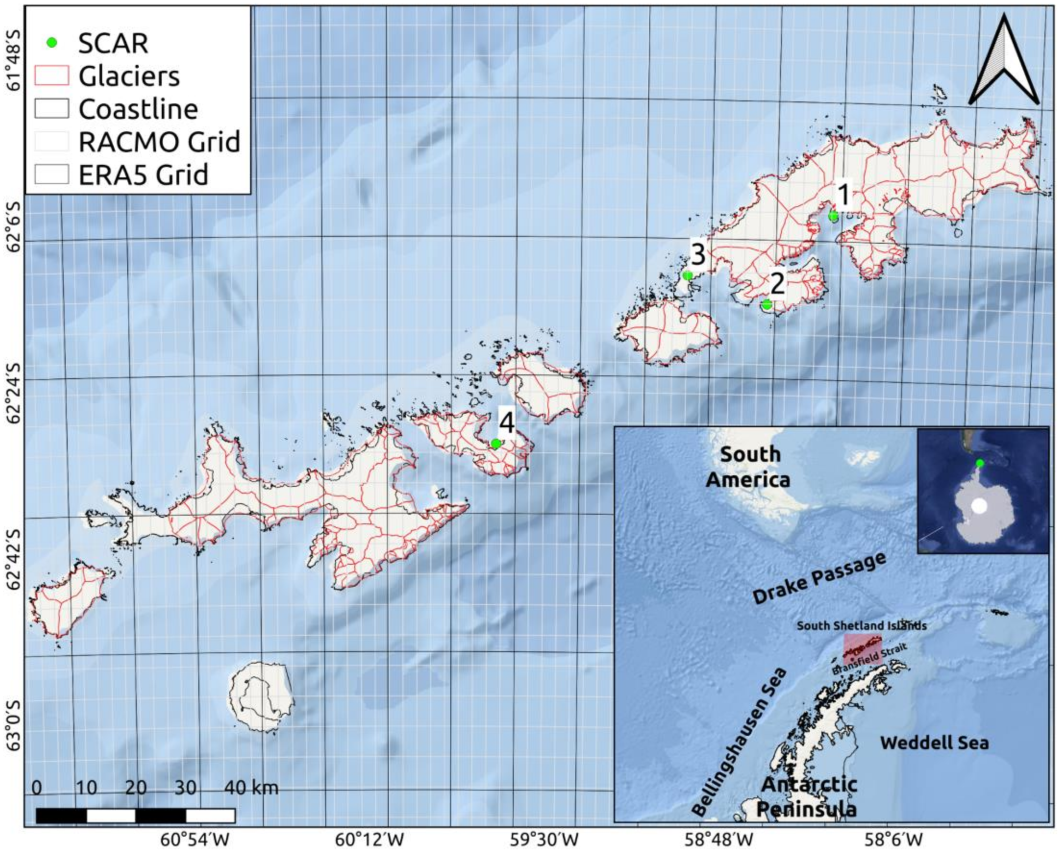

Figure 13. Location map of the South Shetland Islands (SSI), northern Antarctic Peninsula (AP). The green dots indicate the location of the climate stations from east-west (1) Ferraz (Brazil), (2) Carline (Argentina), (3) Bellingshausen (Russia) and (4) Arturo Prat (Chile). The grey grids indicate the spatial resolution of RACMO (~5.5 km horizontal resolution) and the black grids of ERA5 (~31 km horizontal resolution).

Long-term precipitation and consistent observations are very sparse in the Antarctic region. Furthermore, quantifying precipitation in Antarctica involves unique challenges, such as wind and technical difficulties associated with the harsh environment.

The strong winds in Antarctica, which can sometimes travel up to 20 m/s, resulting in blowing snow (Van Lipzig et al. 2004), have a profound effect on the accuracy and reliability of precipitation observations. In the SSI, which has a higher concentration of research stations, we found only one climatic station (Bellingshausen Russian Station) that provides freely available monthly precipitation data from 1968 to the present, ensuring the consistency over time. Monthly accumulation precipitation was obtained directly from Bellingshausen Russian Station website (http://www.aari.aq/stations/bell/bell_en.html).

Table 3. List of climatological stations considered in the study.

Station	Operation nation	Available data	Variables	Lat	Lon	Elevation (m)
Bellingshausen	Russian Federation	1968-2020	T2, PREC	62.20° S	58.97° W	16
Ferraz	Brazil	1986-2005	T2	62.10° S	58.40° W	20
Carlini	Argentina	1986-2020	T2	62.24° S	58.67° W	4
Arturo Prat	Chile	1966-2020	T2	62.50° S	59.70° W	5

In addition, temperature and precipitation data were obtained from the hourly global ERA5 reanalysis and monthly regional RACMO modelling datasets to compare with observations. ERA5 is a global intermediate spatial resolution atmospheric and oceanic dataset available for the entire globe at ~31 km horizontal resolution (Hersbach et al., 2020). Several studies indicated that the ERA5 dataset provides the most accurate depiction of the recent Antarctic climate (e.g., Gossart et al. 2019, Tetzner et al. 2019, Bozkurt et al. 2020, Hillebrand et al. 2021). RACMO is a regional climate model providing high spatial resolution (5.5 km) of atmospheric and glaciological datasets for the entire AP from 1979 to the present (Van Wessem et al. 2016) (https://www.projects.science.uu.nl/iceclimate/models/racmo-data.php). Van Wessem et al. (2016) found that the RACMO realistically simulates the strong spatial variability, although significant biases remain due to the highly complex topography of the AP.

Some preprocessing steps were applied to the ERA5 and RACMO datasets. First, the ERA5 or RACMO grid closest to each climatic station (see Fig. 13) was selected to obtain the hourly or monthly temperature time series. Next, a bias correction was applied to the temperature data using a constant temperature lapse rate of -1.0°C/100 m for ERA5 and -1.2°C/100 m for RACMO. We use different temperature lapse rates for ERA5 and RACMO because they better reduce the root-mean-square errors (RMSE) at each SCAR station. Finally, in the case of ERA5, hourly temperatures were temporally averaged into daily and monthly time scales. In the case of precipitation, as we only have one climatic station with complete and consistent precipitation data, also of only grid select, we selected all ERA5 or RACMO grids that cover the entire SSI. This allows us to have a better spatial representation of precipitation for the entire SSI. Finally, in the case of ERA5, the hourly data were summed to obtain the monthly cumulative precipitation.

A comparison of the time series between the grids closest to the climate stations and all grids covering the SSI showed no significant differences in both ERA5 and RACMO. This indicates that ERA5 and RACMO do not show large spatial variability in precipitation fields for the entire SSI. Therefore, we used the ERA5 and RACMO precipitation time series obtained from the spatial average of all grids covering the SSI.

5.3.3 Atmospheric and oceanic variables from ERA5 reanalysis

In addition, atmospheric and oceanic variables such as geopotential height at 300 hPa (Z300) and air temperature at 850 hPa (T850), mean sea level pressure (MSLP), sea ice extension (SIE) and sea surface temperature (SST) obtained from the monthly ERA5 reanalysis dataset were used to represent large and regional climatic conditions. The ERA5 hourly and monthly products are freely available in the Copernicus Climate Data Store (https://cds.climate.copernicus.eu). The main reason for using the ERA5 reanalysis dataset was because it starts from 1940 compared to satellite-derived oceanographic data for sea ice (e.g., US National Snow and Ice Data Center; https://nsidc.org/home) or surface temperature (e.g., Optimum Interpolated OI SST v2; https://www.ncei.noaa.gov/products/optimum-interpolation-sst). Furthermore, the satellite-derived oceanographic data from 1979 to the present and reconstructed from 1979 to 1950 with a sophisticated approach (e.g., Hirahara et al. 2016) were used to force the European Climate System Model that generates the ERA5 reanalysis dataset.

5.3.4 Large and regional climatic indices

The ENSO indices (such as El Niño 3, 3.5 and 4 regions) were obtained from temperature anomalies (https://www.cpc.ncep.noaa.gov/) to represent teleconnection between the Tropic and South Polar regions. Furthermore, we constructed a custom climatic index that is considered to be large-scale based on outgoing longwave Radiation anomalies in the central Pacific region (hereafter DC-CPAC, see pink in Fig. 14). Recent studies have indicated that deep negative anomalies in the central Pacific region trigger atmospheric rivers landfalling at the AP (Clem et al. 2022). These atmospheric rivers carry large amounts of moisture and heat, which can strongly increase the surface air temperature and surface melting of ice over the AP (Clem et al. 2022). The SAM (https://legacy.bas.ac.uk/met/gjma/sam.htm; monitored using Marshall's (2003) observation-based index) and ASL (https://climatedataguide.ucar.edu/climate-data/amundsen-sea-low-indices) indices were used to represent the large-scale atmospheric circulation of the Antarctic continent (Hosking et al. 2016).

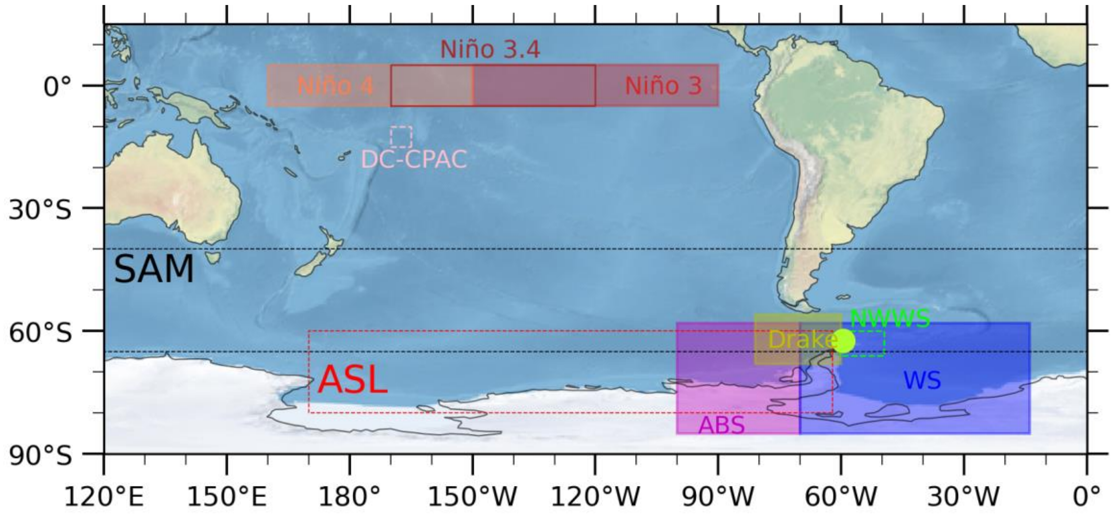

Figure 14. Regions used for the construction of climate indices. Green dot indicates location of the SSI. Amundsen-Bellingshausen (100W-70W; 85S-55S) and Weddell (70W-14W; 85S-55S) Seas regions limits were obtained from Fogt et al. (2022). Drake (81W-60W; 68S-57S) and deep convection anomalies in the central tropical Pacific in the central Pacific (170W-165W; 15S-10S) regions limits were obtained from Clem et al. (2022).

Besides the large-scale indices, we constructed regional-scale climate indices based on the anomalies of Z300, T850, MSLP, SIE, and SST over three key regions: the Drake Passage (hereafter Drake; yellow box in Fig. 14), the Amundsen-Bellingshausen Sea (hereafter ABS; magenta box in Fig. 14), and the Weddell Sea (hereafter WS; blue box in Fig. 14), which directly impact the climate in the SSI. All atmospheric and oceanographic variables used to construct our regional indices were obtained from the monthly ERA5 reanalysis dataset. Finally, we also constructed local climate indices based on SIE and SST for a small region located over the Northwestern Weddell Sea (hereafter NWWS) to assess the local effect of SIE and SST conditions on the SSI.

Recent cryosphere-climate studies on the Larsen C Ice Shelf and Patagonian Icefields used similar strategies to construct climatic indices (e.g., Clem et al., 2022, Carrasco-Escaff et al. 2023). We named these time series Z300-Drake, T850-Drake, SST-Drake, SIE-Drake, SST-WS, SIE-WS, SST-ABS and SIE-ABS, respectively.

5.3.5 Statistical analysis

Pearson's correlations analysis were conducted with significance testing based on detrended time series. Interannual time series were computed for the hydrological year in the Southern Hemisphere that starts on 01 April (year n-1) and ends on 31 March (year n). For example, for the year 2000 it starts on 1 April 1999 and ends on 31 March 2000. Standard meteorological season times series for the Southern Hemisphere were used, where DJF represents summer, MAM represents autumn, JJA represents winter, and SON represents spring, where summer begins in December of the previous year.

5.4 Results

5.4.1 Interannual and seasonal temperature and precipitation variability

Table 4 shows the mean, standard deviation (STD), minimum (Min) and maximum (Max) values for annually observed temperature and precipitation (OBS) from the ERA5 reanalysis and RACMO model. Colder and warmer conditions are evident in RACMO (Mean + STD = -2.09 ± 0.78 °C) and ERA5 (Mean + STD = -1.80 ± 0.75 °C), respectively, compared to OBS (Mean + STD = -1.98 ± 0.83 °C). Regarding annual precipitation, ERA5 has the highest value (Mean + STD = 882 ± 80 mm/yr), followed by RACMO (Mean + STD = 872 ± 81 mm/yr) and OBS (Mean + STD = 696 ± 115 mm/yr). In terms of Min values, both OBS (Min = -4.16 °C) and RACMO (Min = -4.02 °C) temperatures are closer compared to ERA5 (Min = -3.59 °C). Although in terms of Max values, OBS (Max = -0.62 °C) and ERA5 (Max = -0.68 °C) temperatures are closer compared to RACMO (Max = -0.50 °C). Precipitation in ERA5 (Min = 733 mm/yr and Max = 1063 mm/yr) and RACMO (Min = 696 mm/yr and Max = 1070 mm/yr) has higher values compared to OBS (Min = 487 mm/yr and Max = 924 mm/yr).

Table 4. Annual mean (MEAN), standard deviation (STD), minimum (MIN) and maximum (MAX) values of temperature and precipitation observed and modelled for the time period 1980-2020.

	Temperature (°C)			Precipitation (mm)		
	OBS	ERA5	RACMO	OBS	ERA5	RACMO
MEAN	-1.98	-1.80	-2.09	696	882	872
STD	0.83	0.75	0.78	115	80	81
MIN	-4.16	-3.59	-4.02	487	733	696
MAX	-0.62	-0.68	-0.50	924	1063	1070

6.4.2. Temperature and precipitation anomalies intercomparison

When comparing the mean annual air temperature anomalies between OBS, ERA5 and RACMO (Fig. 15a) for the average of the four stations, a good performance is observed with high correlation coefficients (r^2 = 0.89 for the ERA5 and RACMO) and low root mean square errors (RMSE = 0.27 °C for the ERA5 and RMSE = 0.30 °C for the RACMO). However, when comparing the cumulative annual precipitation anomalies between OBS, ERA5 and RACMO (Fig. 15b), persistent systematic errors are present with low correlation coefficients (r^2 = 0.06 for ERA5 and r^2 = 0.26 for RACMO) and large root mean square errors (RMSE = 124 mm for ERA5 and RMSE = 100 mm for RACMO). It is important to highlight that from 2006 to 2020 (Fig. 15b), there is a good agreement between the observed and reanalysis-and-modelled precipitation anomalies (ERA5 and RACMO) with higher correlation coefficients (r^2 = 0.73 for ERA5 and r^2 = 0.67 for

RACMO) and lower root mean square errors (RMSE = 74 mm for ERA5 and RMSE = 63 mm for RACMO) compared to the full-length time series.

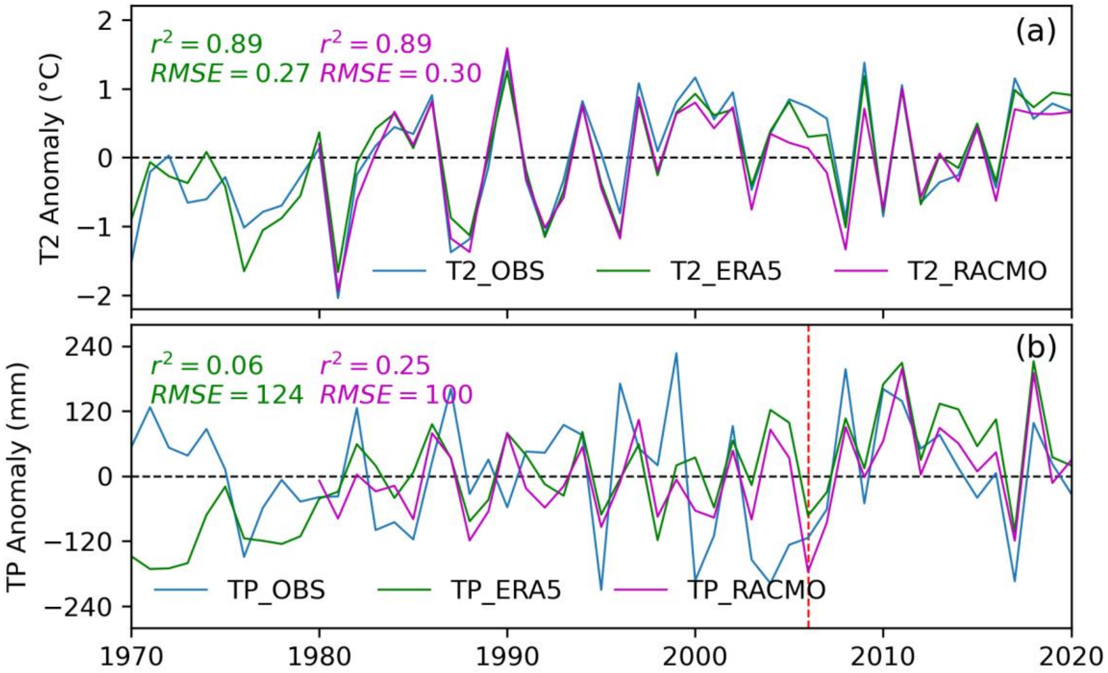

Figure 15**.** Interannual anomalies for the (a) air temperature and (b) total precipitation over the SSI from 1970 to 2020, as estimated for Observations (blue lines), ERA5 reanalysis (green lines) and RACMO (magenta lines). The vertical red line in (b) indicates the start of 2006.

5.4.2 Interannual and seasonal correlation with large- and regional-scale climate indices

As a result of the poor agreement between ERA5, RACMO, and OBS precipitation anomalies, the analysis was conducted independently for observations, ERA5, and RACMO time series.

Interannual temperature variability is influenced by both large- and regional-scale climate indices (Table 5). The ENSO 3.4 (r between -0.33 and -0.43) and ENSO 4 (r between -0.40 and -0.49) indices show weak negative but statistically significant correlations with temperature. The ENSO 3 index also shows weak statistically significant for OBS temperature (r = -0.31) and RACMO (r = -0.35), and non-significant for ERA5 (r = -0.24 for ERA5) correlations. Meanwhile, the DC-CPAC index shows weak negative correlations and statistically significant correlations for ERA5 temperature (r = -0.36) and RACMO (r = -0.30). The SAM index (r between 0.45 and 0.48) shows statistically significant positive correlations, and the ASL index (r between -0.64 and -0.71) demonstrates strong negative correlations with annual temperatures over the SSI.

Table 5. Left three columns show correlation between annual temperature anomalies from Observations, ERA5 and RACMO time series, and large-regional climatic indices. Right three columns show correlation between precipitation anomalies from Observations, ERA5 and RACMO time series, and large-regional climatic indices. Significance is indicated by number asterisk, where * ($p < 0.10$) and ** ($p < 0.05$).

	Temperature			Precipitation		
	OBS	**ERA5**	**RACMO**	**OBS**	**ERA5**	**RACMO**
NIÑO 3.4	-0.38**	-0.33**	-0.43**	-0.17	-0.19	-0.19
NIÑO 4	-0.41**	-0.40**	-0.49**	-0.18	-0.23	-0.24
NIÑO 3	-0.31**	-0.24	-0.35**	-0.17	-0.26	-0.25
DC-CPAC	-0.23	-0.36**	-0.30*	-0.06	-0.19	-0.14
SAM	0.46**	0.48**	0.45**	0.17	0.39**	0.40**
ASL	-0.64**	-0.69**	-0.71**	-0.11	-0.37**	-0.38**
SST-ABS	0.27*	0.27*	0.29*	-0.11	-0.12	-0.02
SIE-ABS	-0.47**	-0.43**	-0.49**	-0.06	-0.04	-0.07
SST-WS	0.64**	0.66**	0.67**	-0.02	0.00	0.03
SIE-WS	-0.62**	-0.65**	-0.67**	-0.02	-0.15	-0.14
SST-NWWS	0.77**	0.68**	0.66**	-0.04	-0.01	0.07
SIE-NWWS	-0.88**	-0.84**	-0.81**	0.18	-0.11	-0.17
Z300-Drake	0.16	0.10	0.08	-0.55**	-0.54**	-0.56**
MSLP-Drake	-0.17	-0.27*	-0.27*	-0.48**	-0.69**	-0.70**
T850-Drake	0.68**	0.69**	0.66**	-0.29*	-0.12	-0.03
SST-Drake	0.46**	0.46**	0.47**	-0.20	-0.11	-0.01
SIE-Drake	-0.57**	-0.57**	-0.65**	-0.14	-0.24	-0.30*

The interannual variability of precipitation is weakly influenced by the large-scale indices and strongly influenced by two regional climate indices. Large-scale indices such as SAM (r between 0.17 and 0.40) and ASL (r between -0.11 and -0.38) show weak but statistically significant correlations in the ERA5 and RACMO time series. In contrast, all ENSO (3, 3.4 and 4) and DC-CPAC indices show weak but statistically non-significant correlations. Only two regional-scale climate indices associated with atmospheric and surface pressure such as Z300-Drake (r between -0.55 and -0.56) and MSLP-Drake (r between -0.48 and -0.70) over the Drake Passage show strong negative correlations with all OBS, ERA5 and RACMO annual precipitation time series in the SSI.

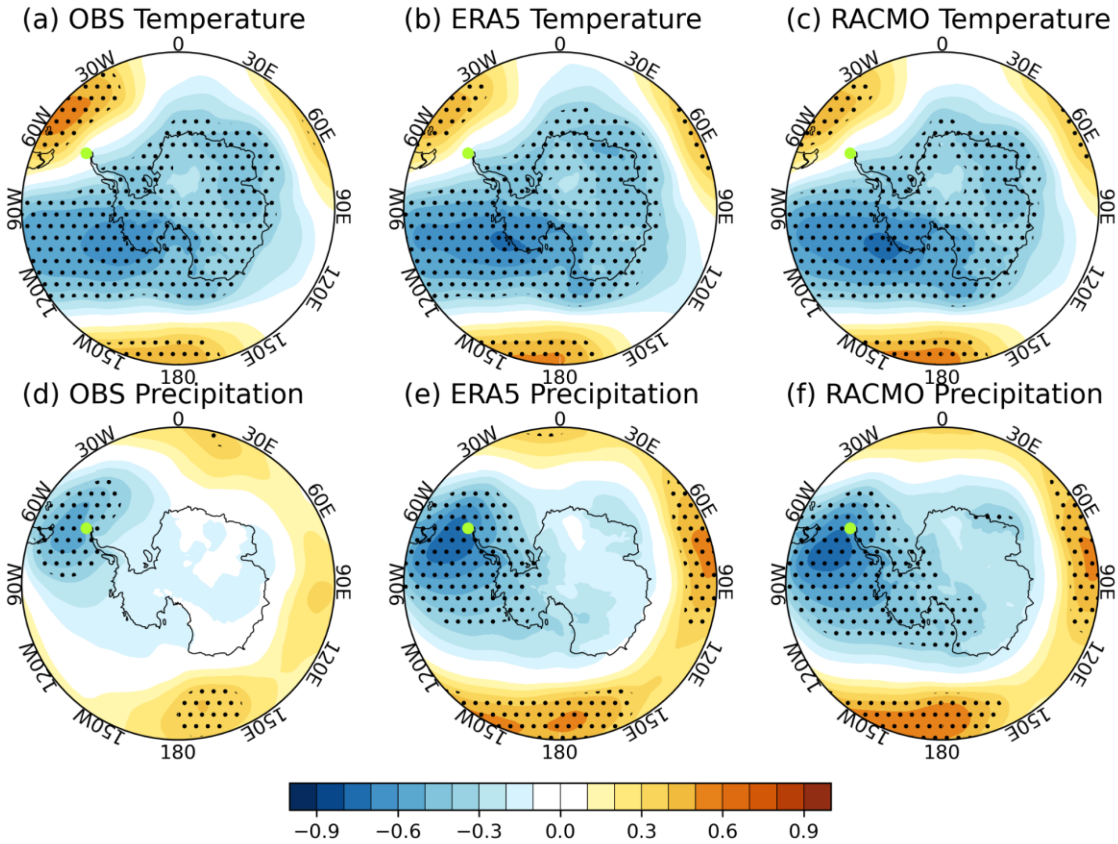

Figure 16. Spatial correlation of the observational data, ERA5 reanalysis and RACMO modelling annual mean temperature (upper plots) and precipitation (bottom plots) time series for 1980–2019 with the spatial annual MSLP from ERA5. The black dots indicate areas where the correlation is significant at $p < 0.05$. The green dots indicate the location of the SSI.

Since the ASL and MSLP-Drake indices were constructed from the ERA5 MSLP fields and they represented the major controls on the temperature and precipitation, respectively. Therefore, it is reasonable to use these fields to show the main atmospheric circulation patterns that control the variability of temperature and precipitation in the SSI. The spatial correlation analysis map between the annual time series of temperature and precipitation with MSLP fields (Fig. 16) clearly shows that temperature is strongly controlled by MSLP anomalies over the Amundsen Sea, while precipitation is mainly controlled by MSLP anomalies over the Drake region. Furthermore, these results are supported by the time series correlation analysis between the Z300-Drake and MSLP-Drake climate indices shown in Table 5 and interannual temperature anomalies with ASL index anomalies and precipitation anomalies with MLSP-Drake anomalies shown in Figures 17, 18 and 19.

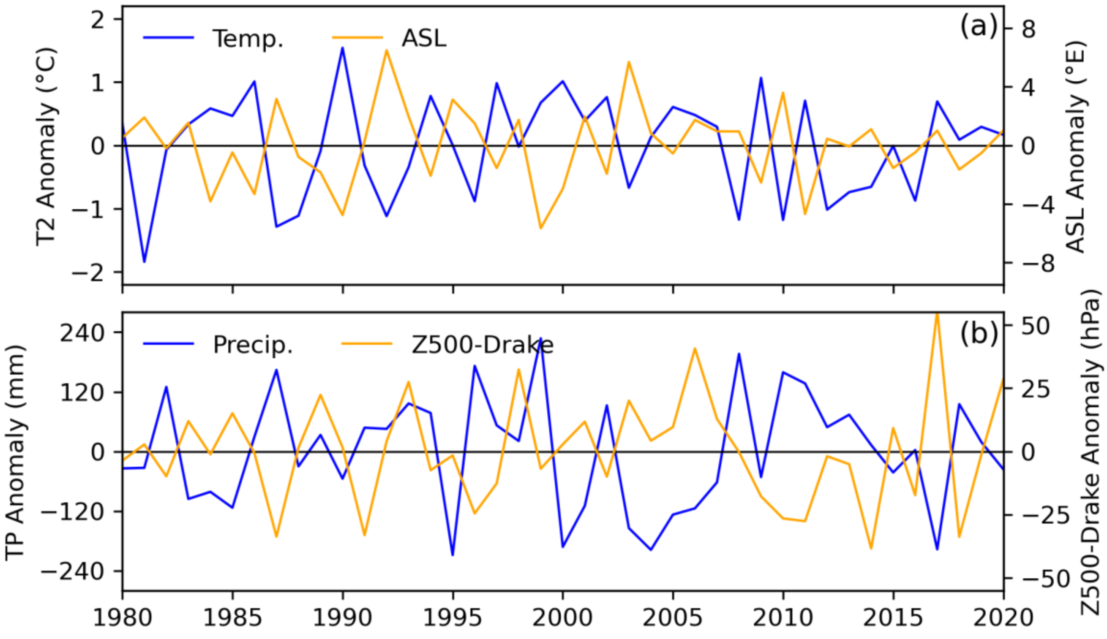

Figure 17. Interannual time series observation of the (a) temperature anomalies (blue) with ASL anomalies index (orange) and (b) precipitation anomalies (blue) with MSLP-Drake anomalies from ERA5 (orange).

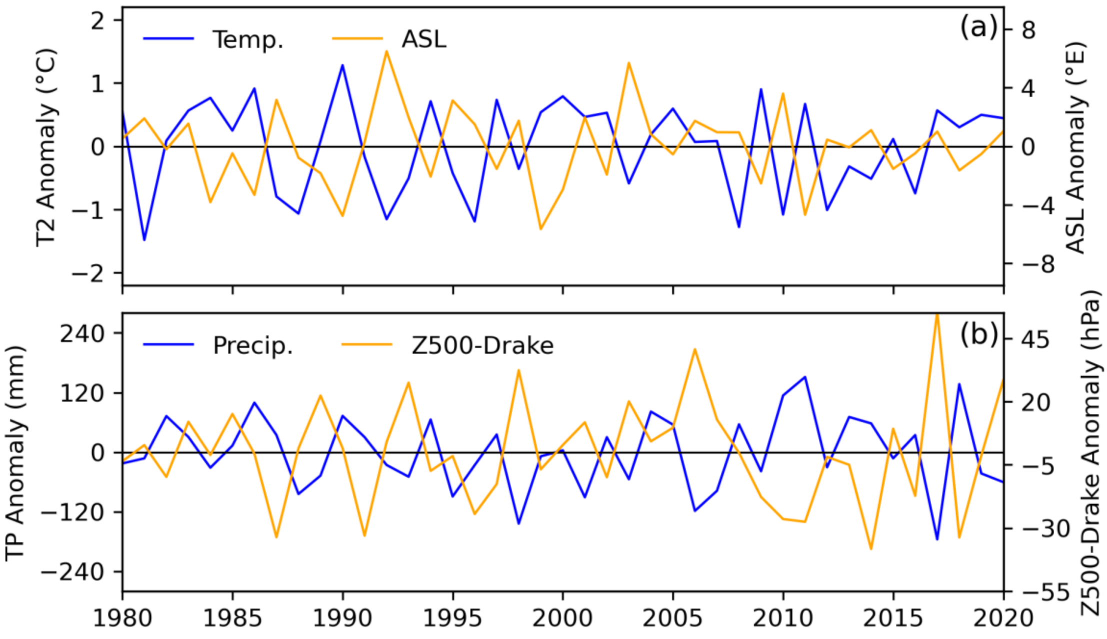

Figure 18**.** The same as in Fig. 17 but using temperature and precipitation anomalies from ERA5.

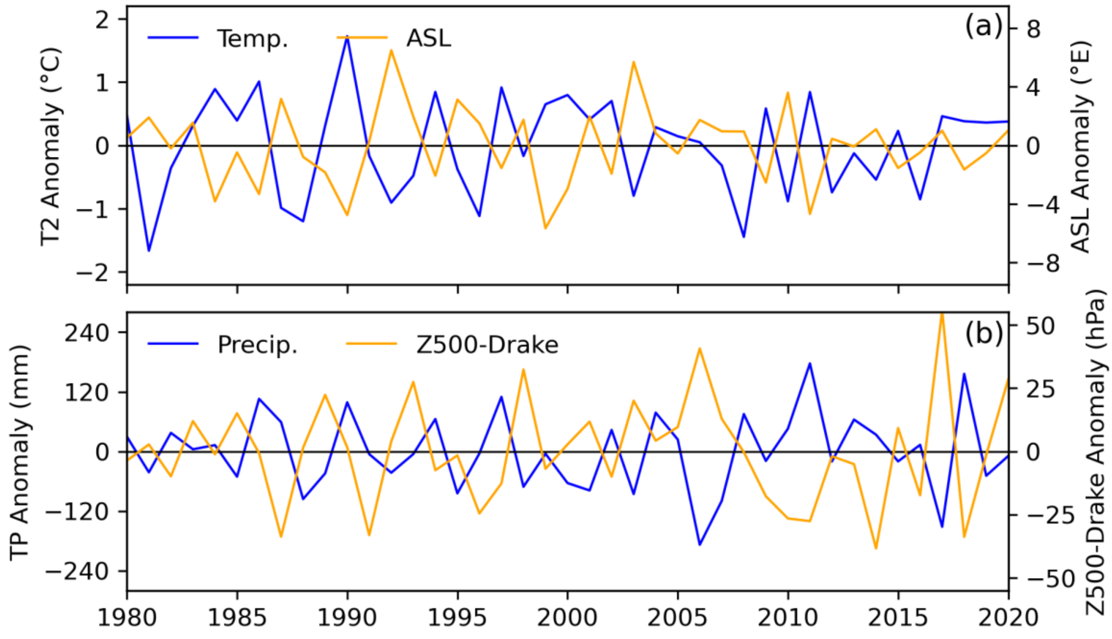

Figure 19. The same as in Fig. 17 but using temperature and precipitation anomalies from RACMO.

Table 6 presents the correlations between the seasonal temperature OBS, ERA5 and RACMO with the different climate indices. Regarding the large-scale climate indices, ENSO 3.4 shows higher significant negative correlations during spring (r = -0.39 for the OBS; r = -0.36 for the ERA5; r = -0.46 = for the RACMO) compared to non-significant during autumn (r = -0.14 for the OBS; r = -0.11 for the ERA5; r = -0.16 = for the RACMO). Meanwhile, ENSO 4 shows higher correlations during winter (r = -0.43 for the OBS; r = -0.44 for the ERA5; r = -0.44 = for the RACMO) compared to summer (r = -0.13 for the OBS; r = -0.27 for the ERA5; r = -0.20 = for the RACMO). Similarly to ENSO 3.4, ENSO 3 shows statistically significant correlations during spring (r = -0.37 for the OBS; r = -0.34 for the ERA5; r = -0.42 = for the RACMO) and non-significant correlations during autumn (r = -0.14 for the OBS; r = -0.09 for the ERA5; r = -0.13 = for the RACMO). SAM and ASL also show significantly stronger signals during winter and spring and weaker signals during summer and autumn, although they remain statistically significant. Clearly, ASL strongly controls the interannual variability of temperature on the SSI, reaching high negative correlations during winter (r = -0.78 for the OBS; r = -

0.79 for the ERA5; r = -0.78 = for the RACMO). DC-CPAC shows weak statistically non-significant correlations during spring (r = -0.12 for the OBS; r = -0.25 for the ERA5; r = -0.21 = for the RACMO).

Table 6. Correlation between seasonal temperature anomalies (Observation, ERA5 and RACMO time series) and large-regional climatic indices. Significance is indicated by number asterisk, where * ($p < 0.10$) and ** ($p < 0.05$).

	Summer			Autumn			Winter			Spring		
	OBS	ERA5	RACMO	OBS	ERA5	RACMO	OBS	ERA5	RACMO	OBS	ERA5	RACMO
NIÑO 3.4	-0.18	-0.36**	-0.30*	-0.14	-0.11	-0.16	-0.29*	-0.29*	-0.32**	-0.39**	-0.36**	-0.46**
NIÑO 4	-0.13	-0.27*	-0.20	-0.26	-0.22	-0.28*	-0.43**	-0.44**	-0.44**	-0.33**	-0.32**	-0.41**
NIÑO 3	-0.20	-0.39**	-0.34**	-0.14	-0.09	-0.13	-0.20	-0.20	-0.23	-0.37**	-0.34**	-0.42**
DC-CPAC	0.05	0.05	-0.01	-0.15	-0.17	-0.18	-0.09	-0.14	-0.18	-0.12	-0.25	-0.21
SAM	0.35**	0.38**	0.48**	0.58**	0.51**	0.61**	0.44**	0.45**	0.39**	0.44**	0.41**	0.47**
ASL	-0.30*	-0.42**	-0.40**	-0.52**	-0.48**	-0.65**	-0.78**	-0.79**	-0.78**	-0.63**	-0.59**	-0.67**
SST-ABS	0.36**	0.35**	0.22	0.32**	0.32**	0.36**	0.42**	0.45**	0.45**	0.31*	0.39**	0.41**
SIE-ABS	-0.40**	-0.38**	-0.33**	-0.31*	-0.23	-0.32**	-0.51**	-0.51**	-0.49**	-0.40**	-0.41**	-0.44**
SST-WS	0.49**	0.61**	0.45**	0.24	0.34**	0.25	0.44**	0.52**	0.56**	0.61**	0.72**	0.73**
SIE-WS	-0.38**	-0.43**	-0.37**	-0.12	-0.21	-0.14	-0.48**	-0.55**	-0.57**	-0.62**	-0.65**	-0.64**
SST-NWWS	0.71**	0.77**	0.64**	0.58**	0.6**	0.45**	0.76**	0.80**	0.80**	0.76**	0.83**	0.80**
SIE-NWWS	-0.70**	-0.63**	-0.58**	-0.67**	-0.69**	-0.53**	-0.93**	-0.93**	-0.92**	-0.81**	-0.85**	-0.81**
Z300-Drake	0.17	0.06	0.08	0.22	0.24	0.21	0.17	0.14	0.13	0.12	0.14	0.04
MSLP-Drake	0.01	-0.15	-0.08	-0.08	-0.04	-0.15	-0.18	-0.22	-0.22	-0.21	-0.19	-0.31*
T850-Drake	0.58**	0.53**	0.46**	0.65**	0.64**	0.68**	0.68**	0.68**	0.69**	0.70**	0.68**	0.69**
SST-Drake	0.55**	0.55**	0.38**	0.36**	0.39**	0.36**	0.55**	0.60**	0.62**	0.36**	0.46**	0.50**
SIE-Drake	-0.29*	-0.27*	-0.23	-0.20	-0.14	-0.24	-0.63**	-0.65**	-0.68**	-0.64**	-0.64**	-0.69**

Considering the regional scale climate indices, both SST and SIE over the three key regions considered in this study, such as ABS, WS and Drake (Fig. 14), have stronger signals in temperature during winter and spring compared to summer and autumn. SIE over the Northwestern Weddell Sea even reaches high correlations during winter (r = -0.93 for the OBS; r = -0.93 for the ERA5; r = -0.92 = for the RACMO). Meanwhile, the pressure fields of both the atmosphere and the ocean show weak and statistically non-significant signals in all seasons. In contrast, T850-Drake shows strong positive correlation signals in all temperature seasons and increases during winter and spring.

Table 7 presents the correlations between the seasonal precipitation from OBS, ERA5 and RACMO with the different climate indices. In context of the large-scale climate indices, ENSO 3.4 indices show significant negative correlations during spring (r = -0.34 for the OBS; r = -0.40 for the ERA5; r = -0.45 = for the RACMO) compared to non-significant during summer, autumn and winter. Similarly, ENSO 3 and 4 show significant negative correlations during spring and non-significant correlations during summer, autumn and winter. DC-CPAC index shows only a significant correlation during autumn (r = -0.24 for the OBS; r = -0.33 for the ERA5; r = -0.30 = for the RACMO). SAM and ASL show non-significant correlations in all seasons.

Still looking at the regional-scale climate indices, both SST and SIE over the Drake and Weddell Seas show weak significant negative correlations with precipitation during spring (e.g., for SIE-Drake, r = -0.31 for the OBS; r = -0.31 for the ERA5; r = -0.37 = for the RACMO). Z300-Drake climate index shows high significant negative correlations during winter (r = -0.53 for the OBS; r = -0.67 for the ERA5; r = -0.60 = for the RACMO), then during autumn (r = -0.44 for the OBS; r = -0.66 for the ERA5; r = -0.68 = for the RACMO), and finally during spring (r = -0.37 for the OBS; r = -0.44 for the ERA5; r = -0.38 = for the RACMO), while it is non-significant during summer (r = -0.14 for the OBS; r = -0.31 for the ERA5; r = -0.22 = for the RACMO). Similar to the Z300-Drake index, the MSLP-Drake index shows high significant negative correlations during winter (r between -0.43 and -0.76), autumn (r between -0.46 and -0.73) and spring (r between -0.44 and -0.48), and non-significant during summer (r between -0.18 and -0.36). Other climate indices do not show significant correlations.

Table 7. Correlation between seasonal precipitation anomalies (Observation, ERA5 and RACMO time series) and large-regional climatic indices. Significance is indicated by number asterisk, where * ($p < 0.10$) and ** ($p < 0.05$).

	Summer			Autumn			Winter			Spring		
	OBS	ERA5	RACMO	OBS	ERA5	RACMO	OBS	ERA5	RACMO	OBS	ERA5	RACMO
NIÑO 3.4	-0.02	0.07	0.05	0.06	-0.15	-0.15	-0.02	-0.06	-0.12	-0.34**	-0.40**	-0.45**
NIÑO 4	0.08	0.13	0.13	-0.08	-0.16	-0.20	-0.05	-0.12	-0.18	-0.32**	-0.36**	-0.40**
NIÑO 3	-0.05	0.06	0.03	0.11	-0.08	-0.08	0.00	-0.15	-0.20	-0.36**	-0.41**	-0.47**
DC-CPAC	-0.14	-0.16	-0.10	-0.25*	-0.31**	-0.32**	-0.12	0.02	-0.01	0.03	0.10	0.06
SAM	0.04	-0.20	-0.20	-0.04	-0.04	-0.04	-0.18	0.15	0.22	0.33**	0.10	0.12
ASL	-0.15	-0.04	0.10	-0.08	-0.20	-0.21	0.17	-0.14	-0.29*	-0.25	-0.14	-0.22
SST-ABS	-0.16	-0.24	-0.17	0.12	-0.02	0.07	-0.17	0.00	0.14	0.03	0.07	0.11
SIE-ABS	-0.04	0.28*	0.25	0.14	0.03	-0.03	0.26	0.05	-0.08	-0.07	-0.18	-0.19
SST-WS	0.13	0.20	0.17	0.05	-0.03	0.03	0.06	0.16	0.22	0.20	0.32**	0.35**
SIE-WS	-0.12	-0.13	-0.13	-0.23	-0.05	-0.08	-0.06	-0.22	-0.29*	-0.15	-0.37**	-0.37**
SST-NWWS	0.22	0.20	0.19	-0.13	-0.14	-0.09	-0.20	0.15	0.23	-0.03	0.02	0.07
SIE-NWWS	-0.22	-0.08	-0.05	0.08	0.08	0.08	0.32**	-0.08	-0.21	0.10	-0.06	-0.08
Z300-Drake	-0.14	-0.31*	-0.22	-0.44**	-0.66**	-0.68**	-0.53**	-0.67**	-0.60**	-0.37**	-0.44**	-0.38**
MSLP-Drake	-0.18	-0.36**	-0.25	-0.46**	-0.73**	-0.72**	-0.43**	-0.76**	-0.76**	-0.44**	-0.48**	-0.46**
T850-Drake	-0.03	-0.17	-0.11	-0.24	-0.26	-0.28*	-0.29*	-0.15	0.01	0.03	0.00	0.12
SST-Drake	-0.11	-0.19	-0.14	0.03	-0.05	0.05	-0.05	0.19	0.31**	0.09	0.18	0.20
SIE-Drake	-0.06	0.12	0.11	0.12	-0.06	-0.11	0.06	-0.21	-0.32**	-0.31*	-0.31*	-0.37**

5.5 Discussions

In general, temperature fields from ERA5 and RACMO are in good agreement with observations. However, precipitation fields show low correlations and large RMSE with observations. Several studies indicated that both reanalysis products and regional models (e.g., ERA5 and RACMO) adequately capture temperature but have a poor representation of precipitation, showing strong overestimates over the Antarctic continent (e.g., Gossart et al. 2019, Tetzner et al. 2019, Hillebrand et al. 2021). Interestingly, from 2006 onwards, the annual precipitation anomalies show good agreement with observations (see Fig. 3, $r^2 = 0.73$ for ERA5 and $r^2 = 0.67$ for RACMO). This could be associated with the large uncertainties present in the SSI precipitation observations due to blowing and drifting snow (Tang et al. 2018). It is possible that the strongest correlation can be attributed to the changing atmospheric circulation, as suggested by Bulat Mavlyudov in personal communication, it is particularly noteworthy considering the prevailing cooling conditions during the 2006-2016 period. In addition, it is difficult to assess and draw a robust conclusion that modelled precipitation data do not capture the temporal variability of precipitation well with only one climate station. However, recent intercomparison studies of short-term precipitation derived from remote sensing and modelling indicate that there is a general overestimation in modelled Antarctic precipitation (e.g., Roussel et al. 2020). Therefore, more long-term observations are required to more robustly assess precipitation fields from ERA5 and RACMO or to assess indirectly with glaciological data such as glacier mass balance.

Interannual temperature variability over SSI is primarily controlled by ASL, followed by SAM and ENSO. It is crucial to note that changes in ASL are largely driven by ENSO and other teleconnections (like strong deep convection over the central tropical Pacific) as well as SAM. Therefore, it is essential to recognize that ASL changes are not independent but rather governed by intricate internal dynamics and teleconnections between the tropical and polar (like Southern Hemisphere) regions. For example, Clem et al. (2016) indicated strong correlations between ASL and SAM during summer ($r = -0.78$), autumn ($r = -0.50$), winter ($r = -0.72$) and spring ($r = -0.81$). They also found that ASL has significant correlations with ENSO during summer ($r = 0.35$) and winter ($r = 0.33$). Regional indices such as SIE and SST over the three key regions (i.e. ABS, WS and Drake) also influence the temperature variability. The SIE-NWWS and SST-NWWS indices have higher correlations compared to the remaining large- and regional-scale climate indices. The T850-Drake index also has a high positive correlation with annual temperatures over the SSI. Our results are in agreement with previous studies (e.g., Gonzalez et al. 2018, Turner et al. 2020, Bello et al. 2022). For example, Bello et al. (2022) reported that the interannual temperature variability observed at King George Island exhibits strong, direct and positive correlations with SAM. In addition, Turner et al. (2020) indicated that ASL plays a fundamental role in the AP temperature, altering the meridional component of the wind, which alters the concentration and extent of sea ice over surrounding seas such as Amundsen, Bellingshausen and Weddell and consequently, the heat flux from the ocean to the atmosphere. Furthermore, Gonzalez et al. (2018) indicated that atmospheric low-pressure patterns over Amundsen and Bellingshausen favour the transport of warm and humid air from the Southeast Pacific to the SSI. Similar influences are found to be considerable during the atmospheric blocking patterns over the Drake Passage and AP (Bozkurt et al. 2022).

We find a statistically significant correlation between precipitation anomalies in the SSI and Z300 pressure anomalies in the Drake region (Table 5 and Figure 16). In general, negative (positive) annual precipitation anomalies are strongly associated with positive (negative) pressure anomalies over the Drake Passage (Table 5 and Figures 17b, 18b and 19b). This indicates that the Drake region plays a key role in precipitation over the SSI. In contrast, the large-scale climate indices show low correlations, in some cases significant (such as ASL and SAM) and in others non-significant (such as ENSO and DC-CPAC) in interannual time scale. These results indicate that large-scale climate indices play a less important role in the interannual variability of local precipitation over the SSI. Nonetheless, at regional and decadal scales, these indices have the potential to generate important environmental changes in the AP such as atmospheric circulation, surface temperature and sea ice, leading to changes in decadal precipitation in the region. Our results are in agreement with Carrasco & Cordero (2020), who indicated that monthly precipitation over the northern AP presents low and non-statistical correlations with the main modes of climate variability such as ENSO, SAM and ASL.

There is a consensus among the observed, ERA5 reanalyses and RACMO modelling precipitation anomalies about the role that the Drake region plays in its interannual variability. Using the time series of observed precipitation anomalies, MSLP anomalies over the Drake play up to 48% (Table 5) of its interannual variability. When using the time series of ERA5 and RACMO precipitation anomalies, these MSLP anomalies over Drake can account for up to 69% and 70% (Table 5), respectively, over these islands. Similar results were reported by Gonzales et al. (2018), who found that a low-pressure atmospheric circulation pattern over the Drake Passage is associated with large negative and positive precipitation anomalies over Livingston Island, located in the SSI. We note that from 2005 to 2016, the MSLP anomalies over the Drake were consistently negative, leading to positive precipitation anomalies over the SSI during this period (Figs. 17b, 18b, 19b). We hypothesise that anomalously low-pressure in the Drake region indicates a higher density of synoptic-scale cyclones, and precipitation from the trailing cold fronts of these systems is a major contributor to precipitation over the SSI.

While this study does not specifically investigate the teleconnections and mechanisms that potentially cause the Drake low, we can speculate on its origin. It is likely that this pressure feature is influenced by tropical forcing (e.g., Hoskins & Karoly 1981, Karoly 1989, Carrasco-Escaff et al. 2023) and the amplified regional warming and cooling over the AP. For instance, Carrasco-Escaff et al. (2023) argued that the establishment of the Drake low would be highly sensitive to the specific location of SST anomalies in the tropical Pacific, indicating that only certain eastern Pacific SST warming and cooling events could activate an anomalous pressure center near the Drake Passage end to favour annual precipitation and high positive mass balances on Patagonia Icefields. In addition, temperature changes are associated with the negative (positive) phases of the SAM, increasing (decreasing) the SIE in the northern part of the AP. For example, from 2005 to 2016 (Figs. 5b, 6b and 7b), MSLP over Drake had negative anomalies in most years. This period was indicated as cooling conditions over the AP (e.g., Turner et al. 2016, 2020, Oliva et al. 2017). Furthermore, Turner et al. (2016) indicated that the positive (negative) phase of SAM has warming (cooling) conditions over the northern AP during the last decades (1980 - 2020). Therefore, we suggest further studies must address the understanding of the teleconnections and mechanisms associated with potentially triggering the Drake low.

5.6 Conclusions

The role of different climatic forcing factors on the interannual and seasonal variability of temperature and precipitation over the South Shetland Islands (SSI) was studied from 1980 to 2020 period. Observational data, ERA5 reanalysis and RACMO simulations were used to determine monthly and annual temperature and precipitation anomalies. In addition, different atmospheric (geopotential height, temperature) and oceanic (mean sea level pressure, ice and sea surface temperature) variables from the ERA5 global reanalysis were used to assess their impacts on the seasonal and interannual variability of temperature and precipitation over the SSI. Various large-scale and regional climate indices were constructed based on these atmospheric and oceanic datasets, focusing on three key regions: Weddell (WS), Amundsen-Bellingshausen (ABS), and Drake Passage (Drake) Seas.

We find that the interannual and seasonal variations in air temperature over the SSI are strongly influenced by large- and regional scale climate conditions. Conversely, interannual and seasonal variability of precipitation in this region is weakly influenced by large-scale climate factors but strongly influenced by regional climate conditions, particularly atmospheric and oceanic pressure anomalies in the Drake region. These pressure anomalies are associated with significant positive and negative precipitation anomalies over the SSI. It is important to note that the indices associated with atmospheric dynamics over Drake (such as Z300-Drake and MSLP-Drake) were statistically significant for precipitation, but did not show such statistically high values for temperature. These results emphasize the crucial role of the Drake region in the temporal variability of precipitation, while its impact on surface temperature over the SSI is relatively less significant. Notable precipitation and temperature changes could directly impact the annual variability of glacier mass balance in the SSI. Hence, it is recommended that future studies consider both large-scale and regional-scale climate modes to gain a better understanding of environmental changes in this region.

Acknowledgments

We thanked the resources provided by the Aperfeiçoamento de Pessoal de Nível Superior (CAPES) to support the Graduate Program in Oceanology at Universidade Federal do Rio Grande (FURG). The first author also thanked CAPES for the PhD scholarship. We wish to acknowledge ECMWF for ERA5 data and JM van Wessem and Jordi Bolibar at Utrecht University for RACMO data. In addition, we would like to thank Tomás Carrasco-Escaff for his useful discussions on this research and share his scripts for the elaboration of some figures. We also appreciate the comments and suggestions of the three anonymous reviewers, as they helped to improve our manuscript. Finally, we are grateful for the SCAR fellowships (https://www.scar.org/general-scar-news/2022-scar-fellows/) that allowed the first author to conduct a research exchange at the University of Valparaíso, Chile.

Chapter VI: New insights on the interannual surface mass balance variability on the South Shetland Islands glaciers, northerly Antarctic Peninsula

This chapter contains the second scientific article published from this thesis, authored by Christian Torres, Deniz Bozkurt, Tomás Carrasco-Escaff, Jordi Bolibar and Jorge Arigony-Neto, and entitled "**New insights on the interannual surface mass balance variability on the South Shetland Islands glaciers, northerly Antarctic Peninsula**". This paper was published in the "Global and Planetary Change" Journal (https://doi.org/10.1016/j.gloplacha.2024.104506). The original format of the paper has been changed for better indexing and understanding of the thesis.

New insights on the interannual surface mass balance variability on the South Shetland Islands glaciers, northerly Antarctic Peninsula

Christian Torres[1,2,*]; Deniz Bozkurt[2,3,4]; Tomás Carrasco-Escaff[3], Jordi Bolibar[5]; Jorge Arigony-Neto[1]

[1] Institute of Oceanography, Federal University of Rio Grande, Brazil
[2] Department of Meteorology, University of Valparaíso, Chile
[3] Center for Climate and Resilience Research (CR)2, Chile
[4] Center for Oceanographic Research COPAS COASTAL, Universidad de Concepción, Chile
[5] Department of Civil Engineering and Geosciences, Delft University of Technology, Netherlands

Corresponding author: * christian010194@gmail.com

6.1 Abstract

Few studies have assessed a comprehensive understanding of how the seasonal and interannual variability and trends of the surface mass balance (SMB), including the influence of atmospheric river (ARs), are governed by the climate on the South Shetland Islands (SSI) glaciers located in the northerly Antarctic Peninsula (AP). To address this gap, we comprehensively analyzed the correlations and regressions between seasonal and annual SMB with regional to global climate indices and a state-of-the-art AR tracking database from 1980 to 2019. The daily and monthly SMB was obtained from two physical glaciological models, which was verified against 19 years of annual and seasonal glacier-wide SMB observations available in three glaciers (Johnsons, Hurd, and Bellingshausen), showing a good ability to capture interannual and seasonal variability. Results indicate a low dependence of the SMB on main atmospheric modes of variability (e.g., El Niño-Southern Oscillation and the Southern Annular Mode), and a moderate dependence on regional climate indices based on atmospheric pressure anomalies and sea surface temperature anomalies over the Drake Passage. Furthermore, our findings reveal that ARs

have different effects on the SMB depending on the season. For example, winter ARs tend to boost accumulation due to increased snowfall, while summer ARs tend to intensify surface melting due to increased sensible heat flux. Our study highlights the Drake Passage as a key region that has the potential to influence the interannual and seasonal variability of the SMB and other climate variables, such as air temperature and snowfall over the SSI. We suggest that future work should consider this region to better understand the past, present and future climate changes on the SSI and surrounding areas.

Keywords: Climate forcings, Atmospheric Rivers, Surface Mass Balance, South Shetland Islands.

6.2 Introduction

The Antarctic Peninsula (AP) region has become a focal point in climate science due to its rapid and pronounced response to global climate change. Since the 1950s, the AP has experienced one of the most significant warming trends on Earth (Bromwich et al., 2013). This region, home to vital ice shelves like Larsen C, is a unique and critical indicator of the ongoing environmental changes occurring on a global scale.

In the last few decades, the AP's climate has demonstrated remarkable variability at decadal time scales, with warming trends intermingling with cooling periods, offering a dynamic canvas upon which the impacts of climate change unfold. For instance, the AP region presented warming (+0.32 °C/decade during 1979–1997) and cooling (-0.47 °C/decade during 1999–2014) trends (Turner et al., 2016; 2020; Oliva at al., 2017; Carrasco et al., 2021). Furthermore, this region experienced two positive (1970-1991 = +60 mm/decade and 2000-2019 = +31 mm/decade) and one negative (1991-1999 = -95 mm/decade) annual precipitation trends (Carrasco et al., 2020). These patterns have been assessed and attributed to a range of factors, from large-scale atmospheric circulation patterns to regional climate drivers, such as the Southern Annular Mode (SAM), El Niño-Southern Oscillation (ENSO), deep convection in the central tropical Pacific (DC-CPAC), and synoptic low-pressure systems (e.g., Marshall, 2007; Ding et al., 2011; Fogt et al., 2011; Fogt and Marshall, 2020; Turner et al., 2016; 2020; Gonzalez et al., 2018; Bello et al., 2022; Clem et al., 2022).

The AP's climate variability and the associated cryospheric responses are not only of scientific interest but also have profound implications for the local and global environment. Understanding the interplay between these atmospheric and cryospheric dynamics is crucial, especially as the AP is projected to experience continued warming and increased precipitation throughout the 21st century (Bozkurt et al., 2021; Vignon et al., 2021). One remarkable aspect of this evolving climate narrative is the role of extreme weather events, specifically atmospheric rivers (ARs), which have recently gained prominence in our understanding of the region's environmental dynamics (e.g., Wille et al., 2019; 2022). These concentrated moisture-laden airstreams can significantly influence temperature, precipitation, and the cryosphere in the AP.

Different glaciological models, ranging from empirical to physical, have been utilized to estimate the surface mass balance (SMB), surface melting and runoff in the AP, examining their relationship with the climate. The positive day degree (PDD) model, for example, has been successfully applied to the AP (e.g., Vaughan, 2006; Costi., at al., 2018). Conversely, more complex physical models coupling atmospheric and snow-ice models have been employed to represent energy exchange processes between the atmosphere and surface in this region (e.g., van Wessem et al., 2016; van Wessem et al., 2018; Wille et al., 2022; Clem et al., 2022). For instance, the Regional Atmospheric Climate Model (RACMO) (Van Meijgaard et al., 2008) and Modèle Atmosphérique Régional (MAR) (Gallée and Schayes, 1994) are each coupled with a snow-ice model.

RACMO and MAR, depending on their configuration, simulate the evolution of the snowpack through subroutines of snow metamorphism, surface albedo, meltwater runoff, percolation, retention, refreezing, and drifting-snow. These models rely on the surface energy balance (SEB) to determine the energy available for melting. Currently, both RACMO and MAR models generate atmospheric and glaciological data at high spatio-temporal resolution for the entire AP, 5.5 and 7.5 km horizontal resolution, respectively. In addition, some studies have used the atmospheric Polar Weather Research and Forecasting (PWRF) (Hines and Bromwich, 2008) model to estimate summer surface melt over the Larsen C ice shelf, located on the eastern AP (e.g., Clem et al., 2022; Zou et al., 2023). In general, RACMO, MAR and PWRF adequately capture the spatial and temporal variability of the AP SMB, as evidenced by comparisons with in-situ and remote sensing observations. Van Wessem et al. (2016) evaluated the RACMO-simulated AP SMB by comparing it with 132 in-situ SMB observations and data from six glacier discharge basins, showing reasonable agreement.

Previous research suggests that recent interdecadal to decadal changes in Antarctic ice mass, as determined by remote sensing or glaciological models, are influenced by both SAM and ENSO (King et al., 2023). The impacts of SAM and ENSO on the ice mass balance across the Antarctic continent exhibit notable variability. For example, during the positive phase of the SAM, negative mass anomalies are observed along much of the West Antarctic coast and southern AP, while notable positive mass anomalies are found over the northern AP (King et al., 2023). Similarly, the positive phase of ENSO tends to drive positive mass anomalies over the majority of western AP (King et al., 2023), while potentially inducing negative mass anomalies over the eastern AP (Zhang et al., 2021). However, more localized studies suggest that SAM and ENSO exert minimal influence on the mass balance and surface melting on interannual scales over West Antarctica and the AP. Clem et al. (2022) found that summer surface melting on the Larsen C Ice Shelf, located in the eastern AP, is primarily triggered by the DC-CPAC, which does not necessarily correlate with ENSO. Similarly, Donat-Magnin et al. (2020) observed that the interannual variability of summer SMB and surface melting over the drainage basins of the Amundsen Sea glaciers, in West Antarctica, is influenced by the position and intensity of the Amundsen Sea Low (ASL). Both studies suggest that ENSO or SAM have minimal or insignificant control over summer mass and melting changes in these regions.

The glacier-climate interaction on AP is complex because other climate forcing factors may have a more pronounced control on glacier mass changes. Wallis et al. (2021) demonstrated that glaciers in the western AP respond to seasonal ice-ocean-atmosphere forcing, highlighting their sensitivity to changes in glacier terminus position and surface melt, rainwater flux, and ocean temperature. Furthermore, ARs over the AP lead to extremely high-temperature events (Bozkurt et al., 2018), significant changes in precipitation patterns (Wille et al., 2021), which in turn, impact on sea ice disintegration, surface melting, and instability of ice shelves in this region (Wille et al., 2022). ARs may also have a spatially varied impact on the mass balance of glaciers and ice shelves located in AP, with positive SMB in the western AP and negative SMB in the eastern AP (Wille et al., 2022). Recently, Zou et al. (2023) reported surface melting on the entire northern AP during the formation of low-pressure and high-pressure systems, resulting in prolonged AR events.

The mass balance changes among glaciers in the northern AP can be quite varied. According to estimates by Seehaus et al. (2023), the Starbuck Glacier showed a slightly positive specific mass balance of 0.03 kg/m^2 year, while the Drygalski Glacier showed an extremely negative specific mass balance of -2.07 kg/m^2 year, both over the period 2013-2017. These changes in mass balance are mainly caused by changes in glacier-to-glacier ice dynamics. However, in much of the northern AP, the observed mass changes can be attributed to climatic mass balance variations.

As the impact of ENSO, SAM, DC-CPAC, ARs, ASL and other climate forcing on the ice mass changes vary spatially over the AP and West Antarctic, more detailed studies need to be developed to understand how these climate forcing factors impact locally in each region. Here, we focused on understanding the influence of climatic forcing factors (i.e., ENSO, SAM, DC-CPAC, ARs, ASL and others climate forcings), on the interannual and seasonal SMB of the South Shetland Islands (SSI) glaciers, situated in northern AP. These islands experience the intricate interplay of atmospheric forces, oceanic dynamics, and the ever-changing cryosphere. The surrounding oceanic forces, including sea ice extent-concentration (SIE-SIC), sea surface temperature (SST), and regional ocean circulation patterns, are integral components of the complex SSI climate system (e.g., Cook et al., 2016; Kerr et al., 2018). Recent studies have further demonstrated that the climatic conditions on the SSI are significantly shaped by specific atmospheric circulation systems, such as low-pressure systems over the Drake Passage and the Amundsen-Bellingshausen Sea (i.e., ASL) (Gonzalez et al., 2018; Torres et al., 2023).

Motivated by Carrasco-Escaff et al. (2023), whose research delved into the impact of climate on the Patagonian Icefields, our study embarks investigating the glacier-climate relationship within the SSI. Carrasco-Escaff et al. (2023) underscored the significance of a low-pressure system situated over the Drake Passage (Drake low) as a prominent driver of the positive SMB over the Patagonian Icefields, surpassing even the primary modes of climate variability, such as ENSO and SAM. In this context, our hypothesis posits that the same low-pressure atmospheric circulation system plays a pivotal role in influencing the variability of SMB among the SSI glaciers, particularly during the winter season.

The Drake low has been identified as one of five atmospheric circulation patterns over the AP (Gonzalez et al., 2018). This system significantly controls precipitation and moisture anomalies over northern AP, including the SSI (Gonzalez et al., 2018, Torres et al., 2023). Gonzalez et al. (2018) underscores that the Drake low and flow over the Drake Passage determine the largest anomalies of precipitation observed at the Spanish Base Juan Carlos I Automatic Weather Station situated on Livingston Island. Here, we define the Drake low as a typical synoptic-scale condition associated with passing frontal cyclones in the Drake Passage.

Furthermore, a comprehensive understanding of how the seasonal and interannual variability and trends of SMB, including the influence of ARs, are governed by the climate in this region is lacking. To address these knowledge gaps, our study is primarily focused on three key objectives to (1) the compare the annual and seasonal SMB obtained with three glaciological models such as PDD model, an intermediate COupled Snowpack and Ice surface energy and mass balance model in PYthon (COSIPY), and RACMO model for the period 1980 to 2019; (2) the assessment of the atmospheric and oceanic influences on SMB across seasonal and interannual timescales; and (3) the evaluation of the impact of ARs on the SMB of these peripheral glaciers.

6.3 Study site and data

6.3.1 South Shetlands Islands glaciers and climate variability

The SSI, located in the northern AP, form one of the largest groups of islands around this region. The SSI comprises several islands, such as King George, Livingston, etc. These islands are separated by the Bransfield Strait and the Drake Passage (Fig. 20). According to Silva et al. (2020), the SSI contains 143 glaciers, among land-terminating and tidewater glaciers (70% of the total).

The climate over the northern AP, where the SSI are located, is extremely complex and varies due to several factors: (1) its northerly position, which leads to both warm-wet and cold-dry through the advection of moist and dry air from the Bellingshausen Sea and Weddell Sea, respectively; (2) its less pronounced topography, which may condition the impact of westerly winds and ARs, in contrast to the central-southern AP that has a more pronounced topographic barrier affecting temperature-precipitation-wind relationships (e.g., Clem and Fogt 2013; Clem at al., 2016); and (3) its proximity to the Drake Passage, making it susceptible to mesoscale cyclonic systems originating from the Bellingshausen Sea, traveling west to east and reaching the Weddell Sea. Additionally, this region has been one of the fastest-warming regions on Earth since the 1950s and serves as a dynamic transitional zone between subpolar-polar and oceanic-coastal environments (Kerr et al., 2018).

Based on the observational data available from the Russian Bellingshausen station covering the period 1969 to 2020, the annual mean temperature is -1.98 ± 0.83 °C, and the annual precipitation accumulation is 967±115 mm/year. Interannual temperature variability across the SSI is predominantly governed by the positioning and intensity of the ASL (Bello et al., 2021; Torres et al., 2023), but it is also moderately influenced by large-scale climate indices such as SAM and ENSO, with ENSO being more visible during spring (September to November) (Clem and Fogt 2013; Clem at al., 2016). Conversely, the interannual variability of precipitation and snowfall over those islands is strongly influenced by mesoscale low-pressure systems originating from the Bellingshausen Sea and traversing the Drake Passage (Gonzalez et al., 2018; Torres et al., 2023), with weaker influences from ENSO and SAM (Carrasco et al., 2021). For instance, Gonzalez et al. (2018) underscored that lows over the Drake Passage are responsible for the largest anomalies of precipitation observed at the Spanish Base Juan Carlos I on Livingston Island.

During the last decades, most glaciers on the SSI experienced shrinkage (21-70 % during 1956-2018), thinning (−0.5 ± 0.6 m/year during 2012-2016), and increased surface melt (Simões et al., 2015; Rückamp et al.2011; Pudełko et al., 2018; Sziło and Bialik 2018; Rosa et al., 2020; Pasik et al., 2021; Shahateet et al., 2021), all of which have been associated with regional warming. However, during the 2002-2011 period, these glaciers showed a decelerated rate of mass loss, attributed to increased precipitation and lower summer surface temperatures (Navarro et al., 2013; Oliva et al., 2017).

Several glaciological studies on SSI glaciers have employed remote sensing (e.g., Simões et al., 2004; Rückamp et al., 2010; 2011; Osmanoğlu et al., 2013; Pętlicki et al., 2017; Pudełko et al., 2018; Shahateet et al., 2021), in-situ observations (e.g., Molina et al., 2007; Navarro et al., 2013; Sobota et al., 2015), and modeling techniques (e.g., Bintanja, 1995; Knap et al., 1996; Braun et al., 2001, 2004; Jonsell et al., 2012; Falk et al., 2018). For instance, Braun et al. (2001) evaluated the influence of large-scale atmospheric circulation on the King George Island ice cap, located on the eastern part of the SSI, for a few case days during the summer of 1997-1998. Their results indicated maximum surface melt rates up to 20 mm w.e. per day under specific atmospheric conditions. Furthermore, Navarro et al. (2013) analyzed a decade's worth of SMB data from two glaciers, Hurd and Johnsons, on Livingston Island in the eastern SSI, revealing a notable deceleration in mass losses from 1957-2000 to 2002-2011. Shahateet et al. (2021) estimated the geodetic mass balance for all SSI glaciers from 2013 to 2017, providing insights into the local glacier health. Their analysis indicated a slightly negative average specific mass balance, close to equilibrium, for the entire area, with a value of −106 ± 70 mm w.e./year.

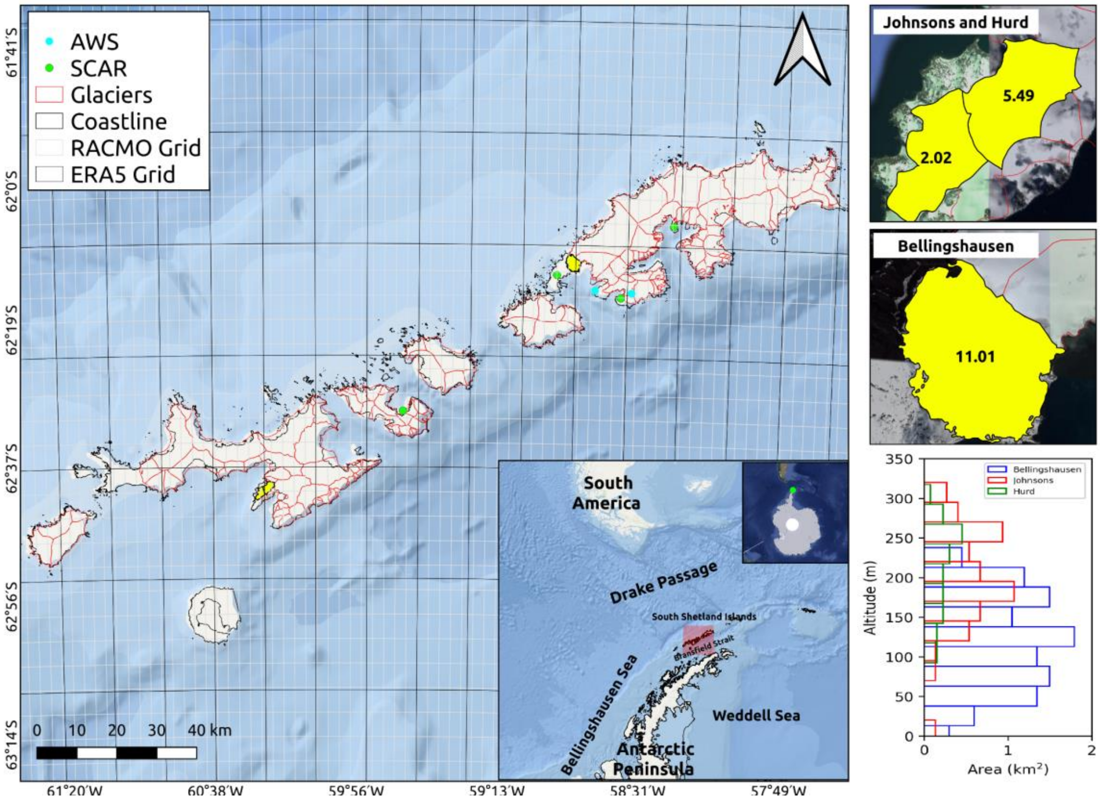

Figure 20**.** Location map of the South Shetland Islands (SSI), northern Antarctic Peninsula (AP). The green dots indicate the locations of the climate stations from READER-SCAR. The cyan dots indicate the positions of the two automatic weather stations (AWS). The red outlines represent the glacier contours obtained from the Randolph Glacier Inventory, (RGI, 2017). The yellow backgrounds mark the locations of the Johnsons, Hurd and Bellingshausen glaciers. The silver grids indicate the spatial resolution of RACMO (approximately 5.5 km horizontal resolution) and the black grids represent the horizontal resolution of ERA5 (approximately 31 km).

6.3.2 Climatological in-situ observations

We used various datasets with different periods and temporal resolutions. The first dataset was collected with an automatic weather station (AWS) installed at Fourcade and Polar Club Glacier (AWS-FPG) and represented the highest station at 194.5 m a.s.l in the SSI (Falk et al., 2018). Various hourly atmospheric variables are available in the AWS-FPG, such as incoming shortwave radiation (QSWin), incoming longwave radiation (QLWin), air temperature at 2 m (T2), relative humidity at 2 m (RH2), wind speed at 2 m (WS), surface pressure (PSFC) and total precipitation (TP) from November 2010 to May 2016. The second dataset was also collected with an AWS installed at the Korean King Sejong Station (AWS-KKS). This station also provides various atmospheric variables available daily, such as QSWin, T2, HR2, WS, PSFC and TP from January 1996 to December 2020. Finally, the third dataset includes only the T2 variable obtained at four climatological stations (Bellingshausen, Ferraz, Carlini and Arturo Prat stations) located over the SSI and made available online by the READER-SCAR (https://legacy.bas.ac.uk/met/READER/surface/stationpt.html). Figure 20 shows the locations of the stations, and Table S1 presented their names, locations, altitudes, and periods of available data.

6.3.3 Glaciological in-situ observations

Very few long-term glacier monitoring programs are available on the SSI (Navarro et al., 2023). There is only one long-term program over this region, collecting data on two glaciers: Johnsons and Hurd, from 2002 to the present. Glacier-wide SMB data are freely available through the World Glacier Monitoring Service (WGMS) on seasonal and annual time scales. Additionally, other short-term (i.e., <5 years of monitoring) programs are available, such as for Bellingshausen Glacier from 2007 to 2012. We used these annual and seasonal SMB data for the Johnsons, Hurd and Bellingshausen glaciers (Fig. 1) to calibrate and validate two glaciological models to reconstruct the SMB of these glaciers from 1979 to 2019.

6.3.4 ERA5 reanalysis

We also used atmospheric and oceanic data from the ERA5 reanalysis produced by the European Centre for Medium-range Weather Forecasts (ECMWF) (Hersbach et al., 2020). ERA5 is provided on a regular latitude-longitude grid of approximately 31 km at hourly and monthly resolutions from 1940 to the present. Both ERA5 hourly and monthly products are available at the Copernicus Climate Data Store (https://cds.climate.copernicus.eu). We used hourly QSWin, QLWin, T2, PSFC, RH2, WS, total precipitation and snowfall from 1979 to 2019 to force glaciological models. Furthermore, we used monthly mean sea level pressure (MSLP), zonal (U) and meridional (V) wind, and geopotential height (Z) at different pressure levels, outgoing longwave radiation (OLR), SIC and SST to represent present atmospheric and oceanic conditions from 1979 to 2019.

6.4 Methods

6.4.1 Glaciological models

6.4.1.1 PDD model

PDD is a simple model based on the empirical relationship between temperature and surface melting of snow/ice (Braithwaite, 1995). This model has been widely used to estimate the glaciers surface melt and runoff, ice fields and ice shelves on the AP (e.g., Vaughan, 2006; Costi et al., 2018). In this study, the SMB using PDD is derived considering accumulation and surface melting processes, as described in equation 1.

$$SMB = ACCUM + \frac{1}{n} \times DDice \times PDD + DDice \times PDD \quad (1)$$

Accumulation (ACCUM) is summed directly as solid precipitation (i.e., snowfall). The melt component (DDice * PDD + DDsnow * PDD) is calculated by multiplying the sums of positive temperatures over a specific period (here n = 8 hours) by snow (DDsnow) and ice (DDice) melting factors. Here, the temperature threshold above which melt occurs is 0°C (Costi et al., 2018). We used the same routine with the PDD model that was made available by Temme et al. (2023). This routine was used by these authors to model the mass balance at the Monte Sarmiento Massif, Tierra del Fuego.

6.4.1.2 COSIPY model

COSIPY is a multi-layer physical model based on the SEB (Sauter et al., 2020) approach. The SEB model combines all energy fluxes impacting the glacier surface energy budget, i.e., SWin, surface albedo (ALBEDO), LWin and outgoing longwave radiation (QLWout), turbulent sensible (QH) and latent (QLE) heat fluxes, ground heat flux (QG), and rain heat flux (QRain). QSWin and QLWin can be provided in the input data, whereas QLWout, QH, QLE, QG and QRain are derived by solving the heat equation (Sauter et al., 2020). This model is widely used in several glaciological studies worldwide due to its user-friendly implementation and free access. COSIPY considers various accumulation and ablation processes to estimate the SMB at high temporal resolution (hourly), following equation 2.

$$SMB = ACCUM + MELT + SUB + DEP + EVA + subMELT + REFRE \quad (2)$$

We calculated the SMB, which considers accumulation (ACCUM), melting (MELT), sublimation (SUB), deposition (DEP) and evaporation (EVA), subsurface melting (SubMELT) and refreezing (REFRE). These components are determined from the available energy, resulting from the SEB, which integrates solar and atmospheric radiation, albedo, turbulent heat fluxes, ground heat and heat from rainfall. In COSIPY, the discharge is assumed to be the sum of the total water percolating through the snow/ice cover due to melting, condensation, and moisture content. More detailed information on COSIPY and its physical parameterisations can be found in Sauter et al. (2020).

6.4.1.3 RACMO model outputs

Additionally, we incorporated monthly SMB data from RACMO for comparison with our simulations. RACMO is a regional high spatial resolution atmospheric and glaciological product available for the entire AP at a 5.5 km horizontal resolution from 1979 to the present (van Wessem et al., 2016, van Wessem et al., 2018). RACMO outputs are used to force a glaciological firn densification model (FDM). The SMB in that FDM is calculated considering accumulation, melting, drifting snow and runoff processes, following equation 3.

$$SMB = PR - SU - SUs - SUds - ERds \quad (3)$$

where PR represents total precipitation (snowfall plus rain), SU denotes surface (SUs) plus drifting snow (SUds) sublimation, ERds corresponds to drifting snow erosion/deposition (caused by divergence/convergence in the horizontal drifting snow flux) and RU stands for meltwater runoff, the amount of liquid water (melt and rain) that is not retained or refrozen in the snowpack. More details on the FDM can be found in Ligtenberg et al. (2011). van Wessem et al. (2016) and van Wessem et al. (2018) found that while RACMO realistically simulates the strong spatial precipitation variability, significant biases remain as a result of the highly complex topography of the AP.

6.4.2 Bias correction of ERA5

To facilitate comparisons with in-situ observations and to force our glaciological models, we carried out preprocessing steps on ERA5 data. First, we applied a bias correction to ERA5 data at the precise locations of the AWS-FPG and AWS-KKS meteorological stations. Second, we also applied a bias correction to the forcing variables at the centroid of each of the three glaciers (Johnsons, Hurd and Bellingshausen) to force the PDD and COSIPY models.

The bias correction preprocessing involved T2, dewpoint temperature (T2D), PSFC and WS. For T2 and T2D, a temperature lapse rate was used to adjust the ERA5 T2 (1 °K/100 m) and T2D (0.9 °K/100 m) to values corresponding to the AWS and glaciers' centroid elevations. These temperature lapse rates showed a better fit than those observed at AWS-FPG (see Figs. S1, S2 and S3). Likewise, the ERA5 PSFC was adjusted to a value corresponding to the AWS and glaciers centroid elevations, using the barometric equation S1 in the supplementary material. The WS at ERA5, initially at 10 meters was adjusted to 2 m using the logarithmic wind profile, equation S2 in supplementary material. Finally, QSWin, QLWin, snowfall and total precipitation were obtained directly from ERA5 to compare and force glaciological models. Several studies indicated that the ERA5 dataset provides the most accurate depiction of the recent Antarctic climate (e.g., Gossart et al., 2019; Tetzner et al., 2019; Bozkurt et al., 2020; Hillebrand et al., 2021).

6.4.3 Glaciological modelling

Both glaciological models (PDD and COSIPY) were configured at a single point since a single ERA5 grid covers the entire glacier area. The average elevation for each glacier was obtained using the glacier outlines available from the Randolph Glacier Inventory (RGI, 2017) and a new high-resolution digital elevation model (DEM) from the gapless 100-m reference elevation model of Antarctica (Gapless-REMA100) as provided by Dong et al. (2022). To force the glaciological models, climate variables were extracted from the nearest ERA5 grid point for each glacier and averaged (QSWin, QLWin, T2, RH2, WS and PSFC) or summed (total precipitation and snowfall) over six-hour time steps. Therefore, the glaciological models were run at six-hour intervals to manage computational demands.

PDD requires only two atmospheric variables as input (temperature and precipitation or snowfall) and has very few free parameters requiring calibration. In contrast, COSIPY demands several atmospheric variables as input (QSWin, QLWin, T2, RH2, PSFC, WS and total precipitation and/or snowfall) and entails the calibration for multiple free parameters.

In both PDD and COSIPY, accumulation is directly derived from snowfall from ERA5, eliminating the need for free parameters like temperature thresholds commonly used to distinguish between solid and liquid precipitation in total precipitation. Additionally, snowfall in ERA5 is already provided in mm water equivalent (w.e.) and does not require conversion using snow/ice density, thus avoiding the use of density parameters. T2, RH2 and PSFC underwent a bias correction (see Sect. 6.4.2), adjusting for the average-elevation of each glacier. QSWin, QLWin, snowfall and total precipitation are also directly obtained from ERA5 without prior preprocessing. Several studies have employed these downscaling strategies to drive long-term glaciological models (e.g., Weidemann et al., 2018; Arndt et al., 2021; Temme et al., 2023). Finally, these three atmospheric datasets of each glacier were used in the experiment simulations.

PPD and COSIPY were optimized using a Randomized Grid Search (RGSearch) technique (e.g., Bergstra and Bengio, 2012). RGSearch, widely used in machine learning, combines Grid Search and Random Search. Instead of evaluating all possible combinations, it randomly samples a specified number of combinations from the free parameters space. Therefore, the free parameters of both PDD and COSIPY were varied randomly within their specified ranges (see Table S2) over 1000 model runs, similar to Mölg et al. (2012). The optimal combination of parameters was that with the minimum RMSE between the observed and modeled SMB during the period calibration (from 2002 to 2011). The validation of the simulations was carried out using an out-of-sample dataset from 2012 to 2019. In PDD, we focused solely on calibrating two free parameters, the DDFice and DDFsnow melt factors. In contrast, for COSIPY, we focused on eight key free parameters associated with the physical parameterization schemes of surface albedo and roughness.

We employed the default COSIPY configuration for the initial conditions, using three months as a spin-up period. In other words, although the simulations start on 1 January 1969, data from 1 April 1969 is used for the analysis. We have included the complete COSIPY configuration (parameterization options, initial conditions, etc.) in the Table S2 of the supplementary material.

6.4.4 SMB seasonal denominations, glaciological model intercomparison and statistical analysis

Throughout this study, we used the hydrological year in the Southern Hemisphere (SH), which starts on 1 April and ends on 31 March of the following year for the annual analysis. For seasonal analysis, winter was considered from 1 April to 30 November and summer was defined from 1 December to 31 March of the following year. To avoid confusion, we referred to these seasonal timescales as winter (April to November) or summer (December to March).

Given that PDD and COSIPY utilize a single point configuration, as opposed to RACMO's distributed configuration, we compared the SMB obtained with all three models. This comparison, summarized in the averaged SMB series named GLAS_PDD and GLAS_COSIPY for PDD and COSIPY, respectively, and GLAS_RACMO for RACMO, allows us to assess the impact of the model configuration on the annual and interannual SMB (Fig. S4b and c). We also obtained an averaged SMB series for all grids overlapping the SSI (Fig. S4a), called SSI_RACMO.

For the verification and validation between observations and modeling or reanalysis data, we used Pearson's or Spearman's correlation coefficient (r), bias (Bias), and root mean square error (RMSE). For the statistical analysis, Pearson's correlations and linear regression analyses were conducted, with significance testing (confidence level of 90%

and 95%) based on detrended time series. Finally, the Mann-Kendall test was used to evaluate trends with a confidence level of 95%.

6.4.5 Sensitivity analysis

Extensive sensitivity analyses were performed using the COSIPY model to ensure the robustness of the interannual variability of the SMB from 1980 to 2020. In our case, COSIPY presents two primary sources of uncertainty, stemming from the model itself and from the input climate data (Arndt et al., 2021).

Sensitivity to main model parameters. We examined the influence of eight key COSIPY model parameters (related to albedo scheme and surface roughness, Table S2) on SMB. Using the RGSearch-optimized parameters as a reference. We evenly spaced each parameter within 10 steps in a given interval. Next, each element was modified while keeping other parameters constant. We compared the resulting SMB series with the optimized series to assess correlation and standard deviation.

Sensitivity to the mean value of the meteorological input. We investigated whether potential biases in the average condition of meteorological input. Introducing an offset (ΔT) to temperature and weighting snowfall with a factor (P0), we ran the SMB model for each pair of values and compared it with the optimized SMB series. We also compared the resulting SMB series with the optimized series to assess correlation and standard deviation.

Sensitivity to the interannual variability of the meteorological input. We analyzed the sensibility of the modeled SMB to interannual variability of the meteorological variables (e.g., snowfall, temperature and insolation). We removed the annual variability from one of the meteorological variables while the other two remained unchanged, similar to Carrasco-Escaff et al. (2023). To do this, we calculated the annual cycle of each variable at a time resolution of 6h, and then used that cycle repeatedly to feed the SMB model. Rerunning COSIPY, we computed a new SMB time series and assessed dependence using squared correlation (R^2). A high R^2 suggests low dependence on year-to-year variations, while a low R^2 suggests high dependence in terms of interannual variability.

6.4.6 Large-, synoptic-, and regional- scale climate indices and AR data

The ENSO indices (such as El Niño 3, 3.4 and 4 regions) were obtained from the National Oceanic and Atmospheric Administration Climate Prediction Center (https://www.cpc.ncep.noaa.gov/) to assess potential tropical-polar teleconnections. We also constructed a customized climatic index DC-CPAC with a large-scale perspective, using a sector delineated in the central tropical Pacific (10–15°S, 170–165°W, see the pink box in Fig. 21) by Clem et al. (2022) to obtain a monthly time series of the area-averaged Outgoing Longwave Radiation (OLR). Recent studies have indicated that deep convection in the central tropical Pacific region triggers ARs making landfall at the AP (e.g., Clem et al., 2022).

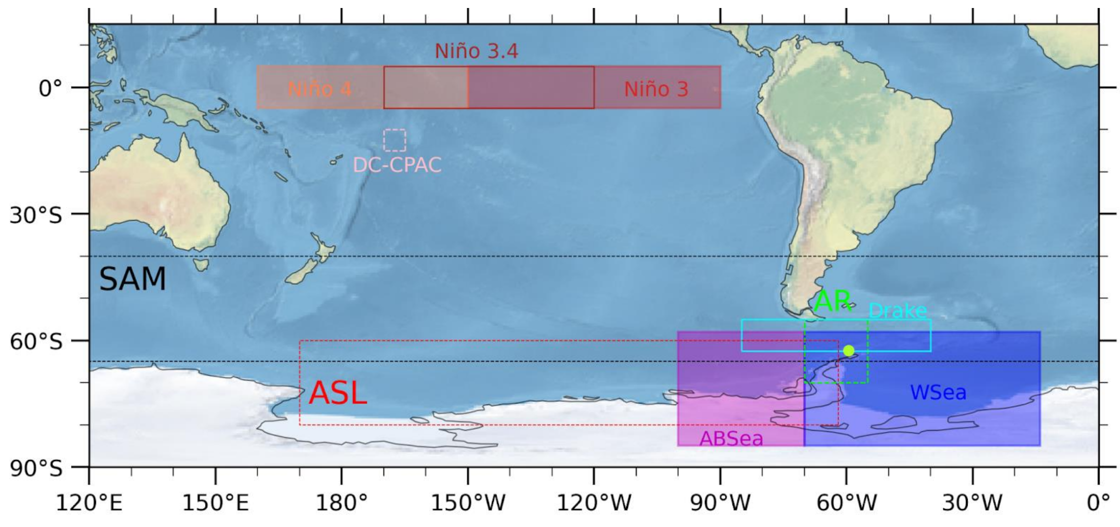

Figure 21. Regions used for the construction of climate indices. The green dot indicates the location of the SSI. Amundsen-Bellingshausen (100-70°W; 85-55°S) and Weddell (70-14; 85-55°S) Seas regions limits were obtained from Fogt et al. (2022). Deep convection over the central tropical Pacific (170W-165W; 15S-10S) region limit was obtained from Clem et al. (2022). ASL limit (170°E-298°E, 60°S-80°S) was obtained from Hosking et al. (2016). Drake region (85°W-40°W; 62.5°S-55°S) was obtained from correlation analysis between winter, annual and summer SMB and Z500. The lime dashed box (70°W-55°W; 55°S-70°S) indicates the area where the ARs frequency is selected and area-averaged.

The SAM and ASL are the large- and synoptic-scale atmospheric circulation which influence the climate changes in the AP. The SAM is characterized by pressure variability between the mid and high southern latitudes, influencing the strength and position of the midlatitude jet. ASL is a climatological low-pressure center located over the southern end of the Pacific Ocean, off the coast of West Antarctica. Both SAM (https://legacy.bas.ac.uk/met/gjma/sam.html; monitored using Marshall's (2003) observation-based index) and ASL (https://climatedataguide.ucar.edu/climate-data/amundsen-sea-low-indices) were obtained from National Center for Atmospheric Research Climate Data Guide.

In addition to the large- and synoptic-scale indices, we constructed regional-scale climate indices over three key sectors: the Drake Passage (hereafter Drake; aqua box in Fig. 21), the Amundsen-Bellingshausen Sea (hereafter ABSea; magenta box in Fig. 21) and the Weddell Sea (hereafter WSea; blue box in Fig. 21), which directly are associated with the climate in the SSI. Monthly time series of SIE and SST are obtained from ABSea and WSea as area-averaged due to their strong relationship with temperature in SSI (Torres et al., 2023).

We identified the Drake Passage (85°W-40°W, 62.5°S-55°S, aqua box in Fig. 21) from west to east with significant correlations between SMB and Z500 during winter, annual and summer timescales, respectively. From this region, monthly time series of MSLP, Z500, T500 and SST were obtained as area-average. This sector was also contrasted with previous studies indicating the different low-pressure systems over the AP and their associated impacts on temperature and precipitation phase (rainfall and snowfall) (Gonzalez et al., 2018; Wang et al., 2021; Torres et al., 2023).

All atmospheric and oceanographic variables (i.e., ORL, MSLP, Z500, T500, SST, SIE) used to construct our large and regional indices were obtained from the monthly ERA5 reanalysis dataset. Then, the monthly anomaly of each variable is calculated independently. The last procedure is also applied for ASL since we used the area-average sea level pressure over the sector (170°E-298°E, 60°S-80°S) defined by Hosking et al. (2016).

Finally, AR frequency was used to evaluate its impact on the glaciers over the SSI. AR frequency data were obtained from state-of-the-art AR tracking databases (1979-2018) available from Guan and Waliser (2019). Monthly time series for AR frequency were constructed for the area of 50W-80W and 55S-75S (green dashed box in Fig. 21). The AR frequency was calculated independently for each grid cell within the box by counting the number of 6-hourly time steps with AR conditions (i.e., grids within detected AR shape boundaries) and dividing by the total number of 6-hourly time steps during the analysis period. The AR frequency is expressed in units of days (i.e., one 6-h AR step = 0.25 days).

6.5 Results

6.5.1 SMB validation and intercomparison periods

Figure 22 shows the annual, winter (April to November), summer (December to March) time series of modelled SMB using different glaciological models (i.e., PPD, COSIPY and RACMO) from 1980 to 2019, alongside the observed SMB from 2002 to 2019, calculated as the average of the three glaciers. The same analysis also was attached for each glacier in supplementary material (Figs. S5 for annual, S6 for winter and S7 for summer). The PDD and COSIPY glaciological models were run using a set of optimal parameters (Table S2) determined through an RGSearch technique (Sect. 6.4.3, Figs. S8 and S9). The statistical indicators for calibration (2002 to 2011), validation (2012 to 2019) and comparison (2002 to 2019) periods are also included in Table S3. Additionally, Table S4 summarizes the mean, SD, minimum, and maximum of the SMB annual, winter and summer for calibration, validation and comparison periods.

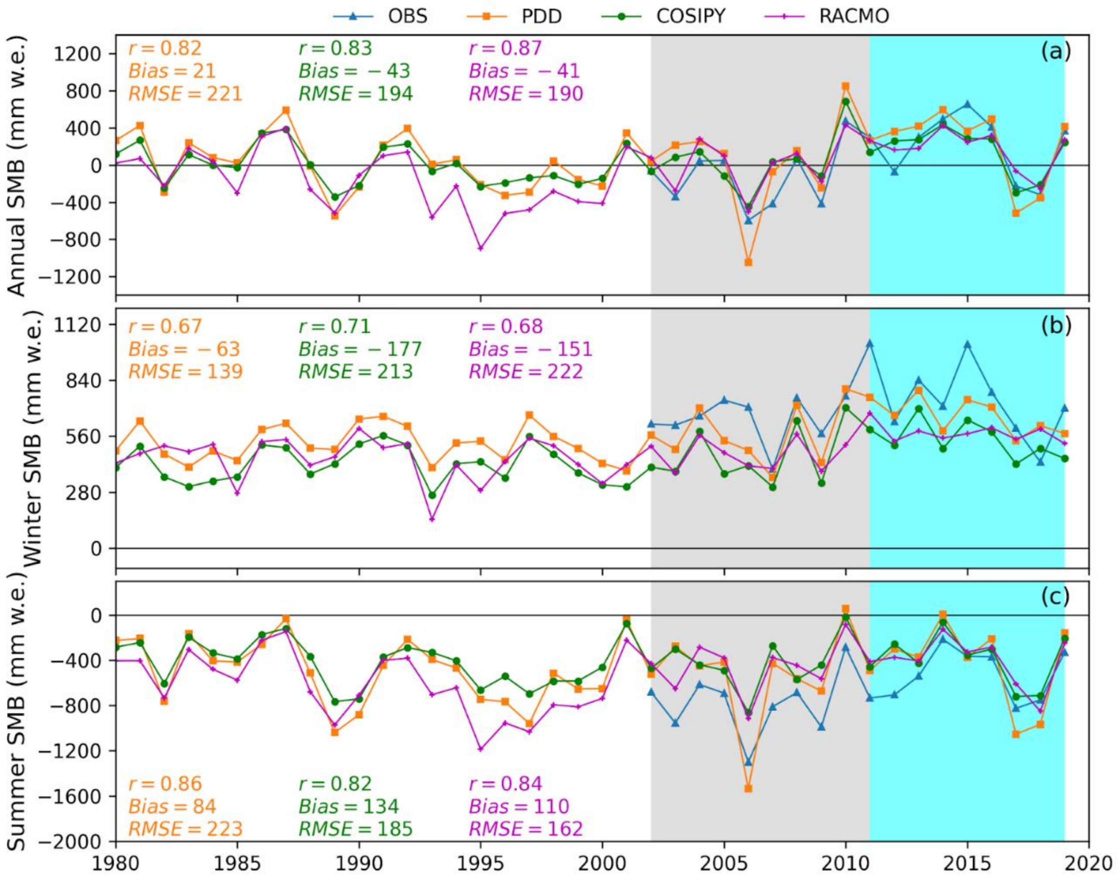

Figure 22**.** Annual (a), winter (b) and summer (c) surface mass balance intercomparison between observation and reconstruction from three glaciological models (blue line OBS, and orange line PDD, green line COSIPY and magenta line RACMO models). Both PDD and COSIPY models were forced using the global reanalysis ERA5-downscaled. Grey shaded areas indicate the calibration period (2002-2011) and aqua shared areas show validation period (2012-2019). Note all statistical indicators as well correlation coefficient (r), Bias and root mean square error (RMSE) were calculated for the validation period (2012-2019).

For the validation period (2012-2019), our results reveal that all models have good agreement with the annual, winter and summer observed SMB: RACMO (r = 0.90, Bias = 8 mm w.e. and RMSE = 149 mm w.e.), PDD (r = 0.82, Bias = 21 mm w.e., and RMSE = 221 mm w.e.) and COSIPY (r = 0.83, Bias = -43 mm w.e., and RMSE = 194 mm w.e.) for annual timescale.

For the comparison period (2002-2019), the mean annual SMB-modeled was more positive by PDD (129 ± 448 mm w.e., mean ± SD), followed by RACMO (125 ± 353 mm w.e.) and by COSIPY (93 ± 275 mm w.e.). The mean SMB-modeled by COSIPY is closer to the observed SMB (40 ± 371 mm w.e.) with a slight difference (53 mm w.e.) and no significant difference in SD. In terms of magnitude, all models underestimate the SMB during the annual, winter and summer timescales.

The time series GLAS_PDD, GLAS_COSIPY, GLAS_RACMO and SSI_RACMO were also used to analyze the correlation and differences between them (see Sect. 6.4.3). We find high correlations and no statistical differences (t-student test appended) between the different annual and seasonal SMB series, even when compared to the series from SSI_RACMO (Table S5). This indicated that SMB modeling shows a similar behavior across models. Therefore, whether using a single-point or distributed model configuration does not impact the final glacier-wide SMB results for the SSI. For the analysis of climatic influences and ARs on SMB, temperature, and snowfall, we utilized the time series from SSI_RACMO, which encompasses all SSI grids. Additionally, we used COSIPY outputs for more detailed analysis of ARs impact and SMB sensitivity.

6.5.2 SMB interannual variability and trends

Using the SSI_RACMO time series, the mean annual SMB was positive 109 ± 321 mm w.e./year, ranging from -688 to 747 mm w.e./year over the entire period (1980-2019) (Table S6). During winter, the modelled SMB increases up to 486 ± 77 mm w.e., while during summer it decreases down to -377 ± 300 mm w.e.

The trend of the annual SMB of SSI glaciers from 1980 through 2019 showed a signal break (Fig. 23), reflecting the surface temperature trends of the AP region (compared with Fig. 4 in Carrasco et al. 2021). During 1980-1997, the trend was negative (-315 mm w.e./decade), and during 1999-2014, it was positive (+425 mm w.e./decade), with both cases being statistically significant ($p<0.05$). The break in the trend influenced the analysis of the SMB trend for the entire period, showing a positive but statistically non-significant trend (+57 mm w.e./decade; not significant). However, a declining trend has emerged in recent years and this trend is clearly illustrated by the period from 2015 to 2019, where the SMB values once again turned negative (e.g., SMB = -89 mm w.e in 2017).

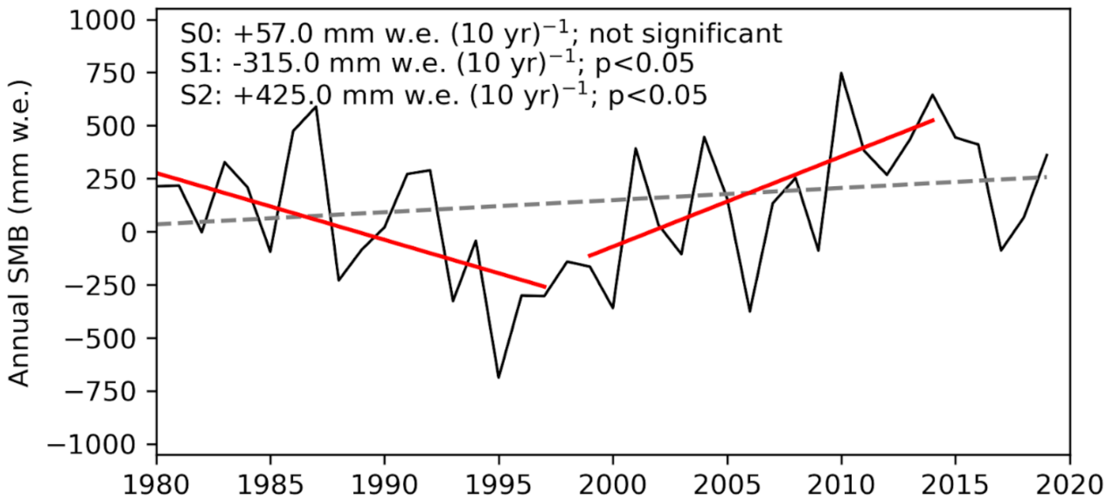

Figure 23. Annual (April to March) surface mass balance from 1980 to 2019 based on the SSI_RACMO time series. The red lines show the linear trends for the periods 1980–1997 and 1999–2014. S0 corresponds to the entire period. S1 (1980-1997) considers the years of warming, and S2 (1999-2014) considers the years of cooling that are well-documented over the region.

6.5.3 Local-scale control over the SMB

Figure 24 shows the annual time series of the modelled SMB, accumulation, ablation, precipitation, temperature, and insolation, calculated as the spatial average of SSI glaciers from RACMO (SSI_RACMO time series). Winter and summer time series of the same variables also are attached on supplementary material (Figs. S10 and S11). Furthermore, correlation analysis of annual, winter and summer SMB with accumulation, ablation, snowfall, temperature and solar insolation are presented in Table S7.

The annual SMB shows a high negative correlation with ablation (r = -0.95, $p<0.05$) and a moderate positive correlation with accumulation (r = 0.40, $p<0.05$). In contrast, winter SMB shows a high positive correlation with accumulation (r = 0.89, $p<0.05$) and a moderate negative correlation with ablation (r = -0.33, $p<0.05$). Similar to the annual SMB, summer SMB demonstrates a high negative correlation with ablation (r = -0.99, $p<0.05$) and a low correlation with accumulation (r = 0.26, no-significant). Additionally, from the correlation analysis between annual, winter and summer of the SMB for the period 1980-2019, we observed that the annual SMB is strongly related to the summer SMB (r = 0.97, $p<0.05$) and moderately related to the winter SMB (r = 0.46, $p<0.05$). These results indicate that the annual variability of the SMB is mainly controlled by ablation which is related to air temperature and moderately by accumulation which is related to snowfall.

To support the findings above, we have developed different sensitivity tests using the COSIPY model. We used these outputs to explain the impact of temperature and snowfall on the SEB and SMB components. One experiment involved adjusting the temperature by an offset and modifying the snowfall by a factor. The temperature varied by ±1°C and the snowfall by ±20%. We used five outputs with neutral (no changes in temperature and snowfall), cold (-1°C air temperature), warm (+1°C air temperature), dry (-20% snowfall) and wet (+20% snowfall) conditions. The results, presented in Table S8 in the supplementary material, show that glacier SEB and SMB are highly sensitive to changes in air temperature and less so to changes in snowfall. Small changes for the SEB components such as QLWout and QH and QLE were observed when introducing a temperature offset. Conversely, large changes for the SMB components, particularly surface melting, which increased by a factor of 10.6 with the temperature adjustment, were noted.

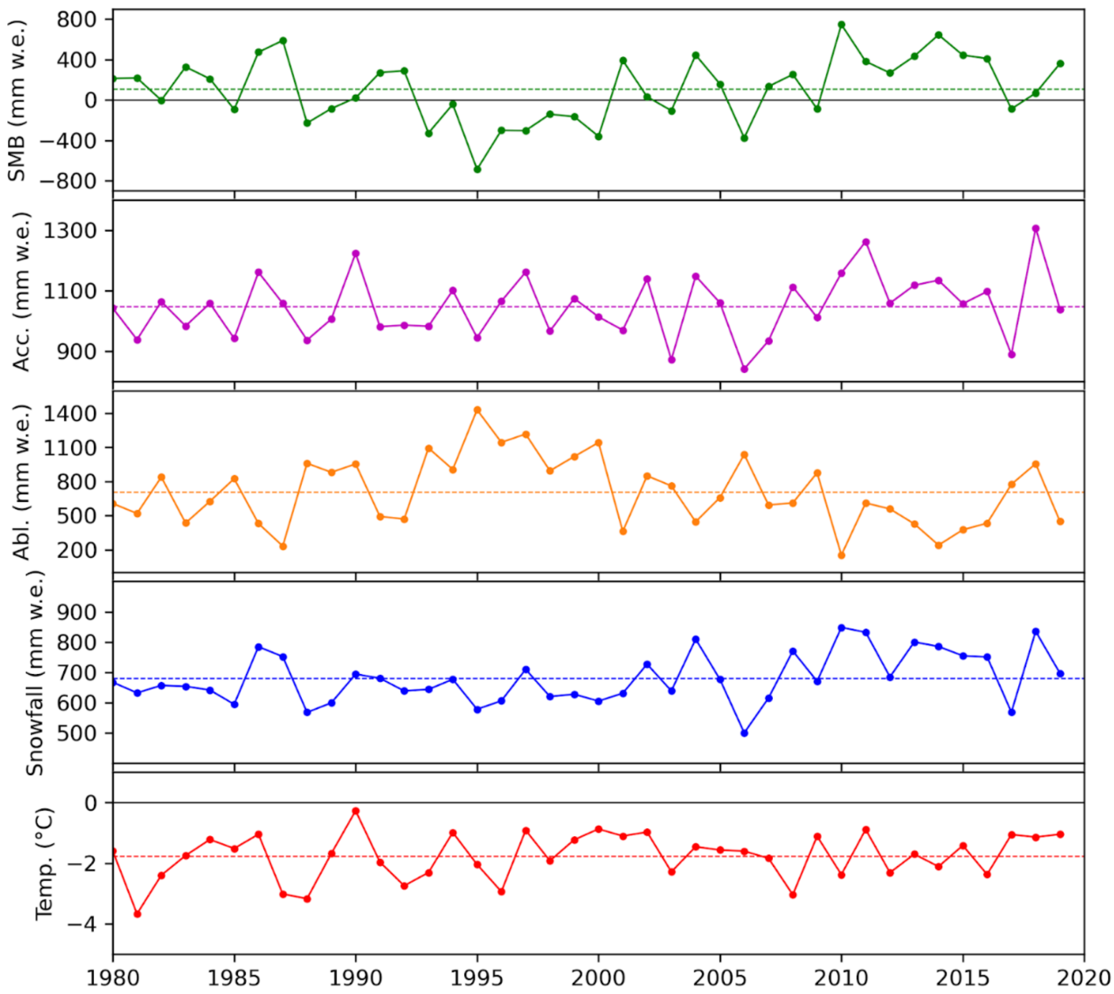

Figure 24. Annual (April to March) time series of spatially averaged (over the area of the SSI glaciers) fields from SSI_RACMO of (from top to bottom) SMB, accumulation, accumulated snowfall, ablation, mean near-surface temperature, and mean insolation. Each segmented line indicates the mean value of the series. The gray horizontal line corresponds to the SMB zero isoline.

6.5.4 Regional-scale control over the SMB

We conducted linear correlations and regressions analysis between the SMB from SSI_RACMO time series and different climate variables from ERA5 (i.e., precipitation, near-surface temperature, and horizontal wind at 10 m above ground level and 500 hPa) for the period 1980-2019 to assess the regional climate control on the variability of the SMB in the SSI during annual, winter, and summer timescales. Additionally, we computed latitudinal profiles of regressions of the annual, winter and summer SMB with the mean annual fields of zonal wind, geopotential height, and air temperature at a longitude of 58° W. The results are presented in Figures 25 for annual, 26 for winter, and 27 for summer. The same analysis was performed using GLAS_COSIPY time series (Fig. S12, S13 and S14). For simplicity, we focus our analysis on the years when the SMB is above the mean value (the analysis extends linearly to other cases).

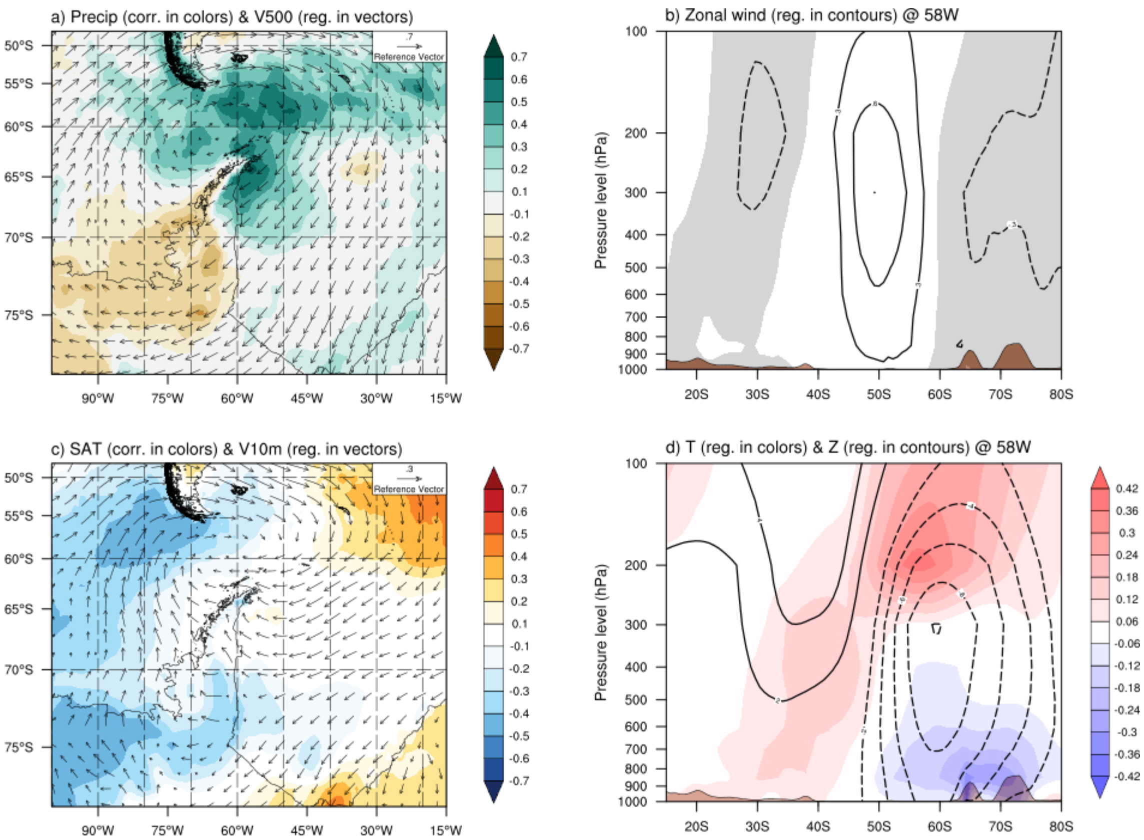

Figure 25**.** Regional correlation and linear regression maps of the annual (April to March) SMB from the SSI_RACMO time series and ERA5 reanalysis. (a) Regression with annual fields of horizontal wind at 500 hPa (vectors in m/s per SD) and correlation with accumulated precipitation (colors). (b) Latitudinal and atmospheric profile of the regression with annual fields of zonal wind (contours in m/s per SD) for a transect at 58°W. Negative regression values are shaded. (c) Regression with annual fields of horizontal wind at 10 m above ground level (vectors in m/s per SD) and correlation with the mean near-surface air temperature (colors). (d) Latitudinal and atmospheric profile of the regression with annual fields of geopotential height (contours in gpm per SD, where gpm stands for geopotential meters) and temperature (colors in ◦C per SD) for a transect at 80° W.

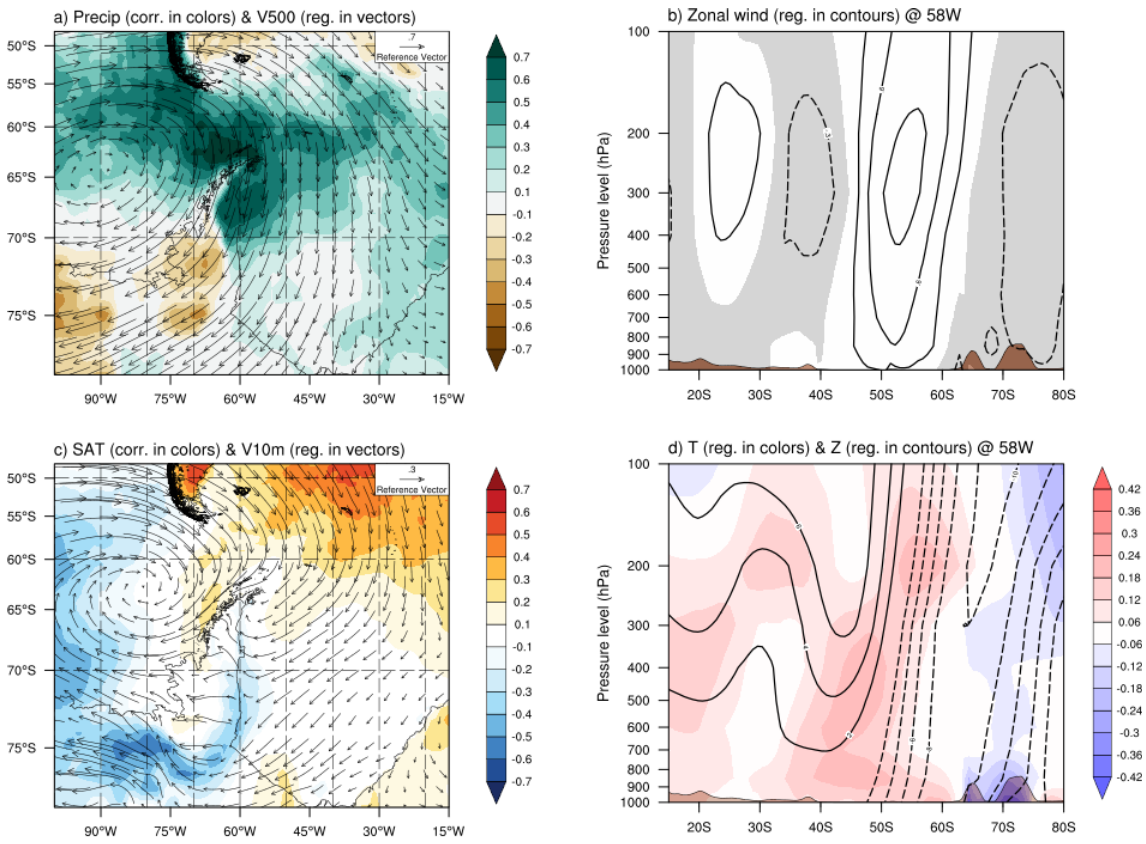

Figure 26**.** The same as in Fig. 25 but for the glaciological winter (April to November).

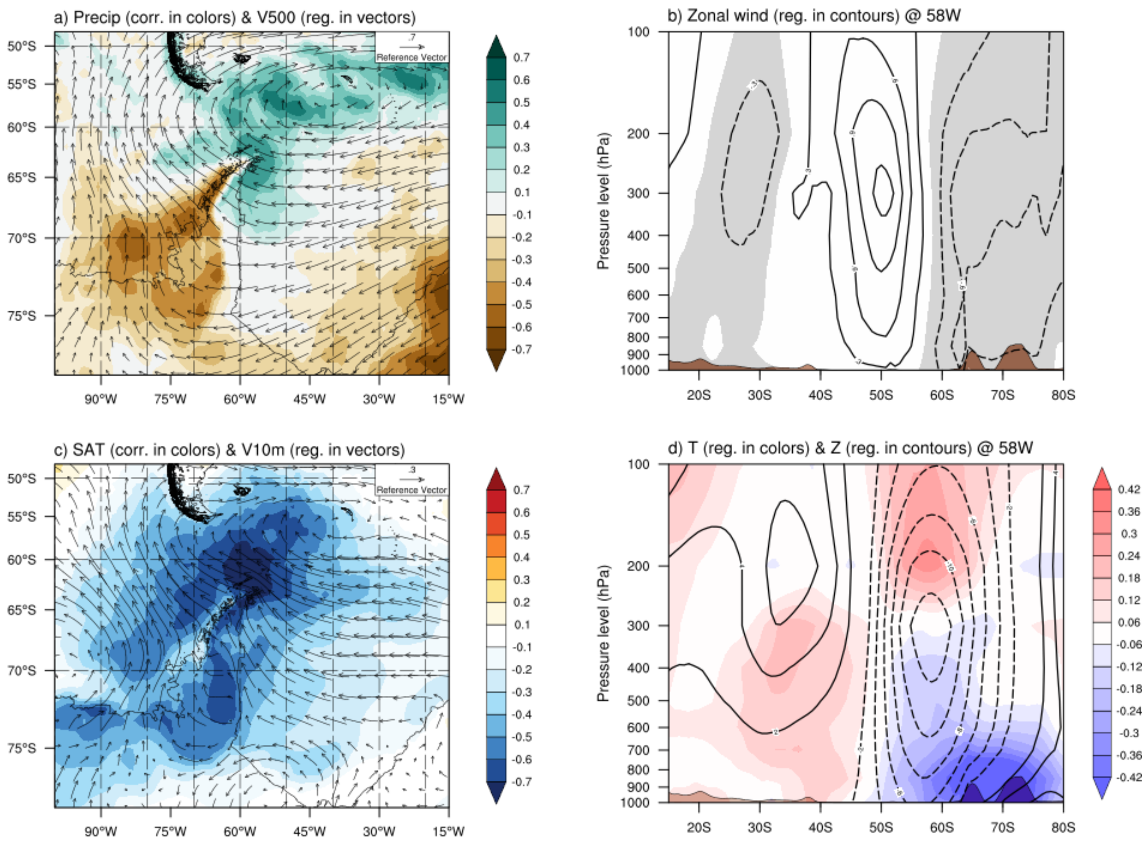

Figure 27**.** The same as in Fig. 25 but for the glaciological summer (December to March).

The results show positive correlations between annual SMB and precipitation over the Drake Passage and the western part of the South Atlantic Ocean (Fig. 25a), which extends over the SSI. The regression analysis between annual SMB and the zonal wind at 500 hPa indicates the presence of a cyclonic atmospheric circulation system over the Drake Passage (Drake low), with its core located in the north-western part of the SSI (Fig. 25a). This system favors convective processes, cloud formation, and precipitation over the Drake region. The Drake low has been identified as one of five atmospheric circulation patterns over the AP that have significant impacts on precipitation and moisture variability over the SSI (Gonzalez et al., 2018; Torres et al., 2023). Furthermore, the annual SMB shows a negative correlation with the temperature over the southeastern Pacific Ocean and the AP, which also extends over the SSI (Fig. 25c). The regression analysis between SMB and the zonal wind at 10 m also shows the presence of this cyclonic system over Drake, extending over northern Bellingshausen Sea and the northern Weddell Sea. This system favors the entry of cold and dry air masses from the Weddell Sea (Fig. 25c). In addition, according to annual latitudinal profiles regressions analysis, the westerlies show negative (positive) anomalies from 80°S to near 60°S (from 58°S to near 40°S), indicating a weakening of these winds over the AP and an increase over south of South America (Fig. 25b). Negative geopotential height anomalies are observed from 80°S to 45°S, reaching their maximum around 60°S, at all levels of the atmosphere (Fig. 25b).

Analyzing the seasonal differences, during winter, years with positive SMB are characterized by the stronger presence of a cyclonic circulation and a more pronounced increase in precipitation over the Drake region (Fig. 26a). Additionally, during summer, a cyclonic circulation system over the northern Weddell Sea favors a cooling regional effect on the northern AP and Bellingshausen-Drake Seas, caused by the entry of cold air from the southern Weddell Sea and AP (Fig. 27c).

6.5.5 Large-scale control over the SMB

In addition, we conducted linear correlations and regression analyses between the SMB from SSI_RACMO and different climatic variables from ERA5 (i.e., MSLP, near-surface temperature (SST in ocean area plus T2 in continental area), U500 and V500 wind components, geopotential height at 300 hPa, and OLR) for the period 1980-2019 to assess the large-scale climate control on the variability of SMB in the SSI during annual, winter, and summer timescales. The results are shown in Figures 28, 29 and 30. The same analysis also was performed using GLAS_COSIPY time series (Fig. S15, S16 and S17). As in the regional analysis, in this section, we also focus on the years with positive SMB.

Highly negative correlations are observed between the annual SMB and SST over the Drake Passage (Fig. 28a). The Drake Passage also is characterized by the presence of a low-pressure system, based on MLSP, extending longitudinally from the northern Bellingshausen Sea to the northern Weddell Sea (95°W-25°W) and latitudinally from southern AP to southern South America (75°S-45°S) (Fig. 28a). In addition, the regression analysis between SMB and the zonal wind at 500 hPa (V500) shows a cyclonic circulation system with a center located over the Drake Passage (Fig. 29b), extending over the same region as the low-pressure system. Thus, anomalies of the SST, and surface and atmospheric pressure over the Drake and surrounding regions can play an important role in the SSI SMB.

Conversely, a weak, non-significant positive correlation is shown between the annual SMB and SST over the tropical Pacific Ocean (140°W-70°W; 5°N-5°S). Thus, the ENSO-associated warming (cooling) of the central and eastern Pacific may favor years with relatively positive (negative) SMB over the SSI glaciers. According to Li et al. (2021), during El Niño events, there is typically a weakening of the ASL, which can induce cooling in the AP. However, depending on the type of ENSO it can influence the precipitation of the AP. During the eastern Pacific El Niño, precipitation decreases across the AP and the Amundsen-Bellingshausen seas, while during the central Pacific El Niño precipitation decreases mainly in the western AP and increases in the eastern AP (Chen et al., 2023). These different impacts on precipitation can inhibit the impact on the interannual SMB.

OLR over the west-central tropical Pacific (180°W-150°W; 28°S-5°S) also shows a weak but significant negative correlation with SMB. Specifically, negative OLR anomalies over the central tropical Pacific are related to positive SMB anomalies in SSI, similar to ENSO which are also associated with positive SMB anomalies over these islands. These OLR anomalies are accompanied by geopotential height anomalies at 300 hPa with the formation of a series of low, high, and low-pressure anomalies, as seen in Figure 28c, extending from the tropics to the extra-tropics as a result of high convective activity over the central tropical Pacific. These negative OLR anomalies generate stationary Rossby wave trains propagating eastward and poleward, inducing atmospheric circulation anomalies affecting temperature, precipitation, and SMB in northern AP.

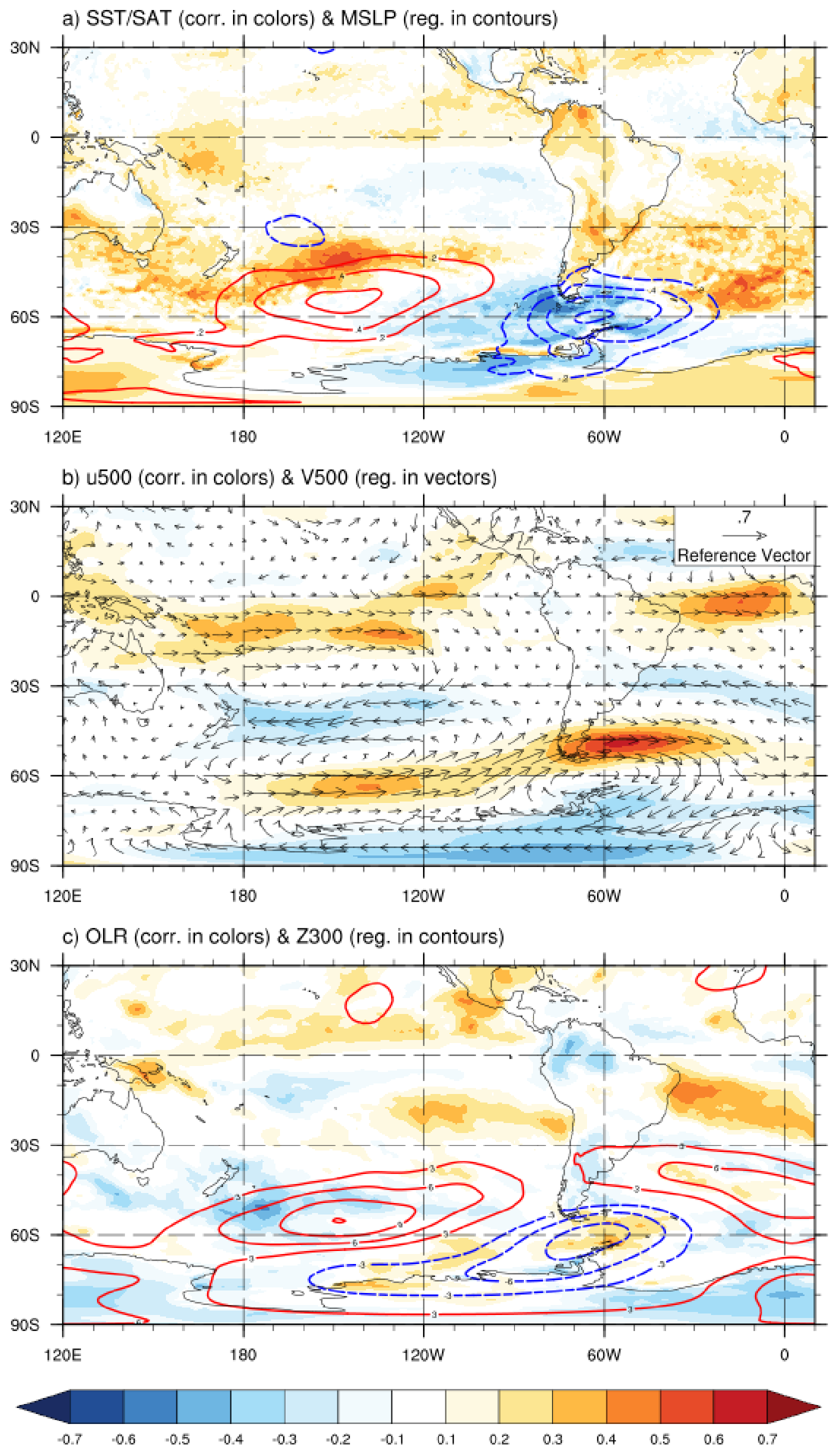

Figure 28. Large-scale correlation and linear regression maps of the annual (April to March) SMB from SSI_RACMO time series with fields obtained from the ERA5 reanalysis. (a) Regression with the annual field of mean sea level pressure (contours in hPa per SD) and correlation with the annual field of sea surface temperature (colors over ocean) and near-surface air temperature (colors over land). (b) Regression with the annual field of horizontal wind at 500 hPa (vectors in m/s per SD) and correlation with the annual field of zonal wind at 500 hPa (colors). (c) Regression with the annual field of geopotential height at 300 hPa (contours in gpm per SD) and correlation with the annual field of outgoing longwave radiation (colors).

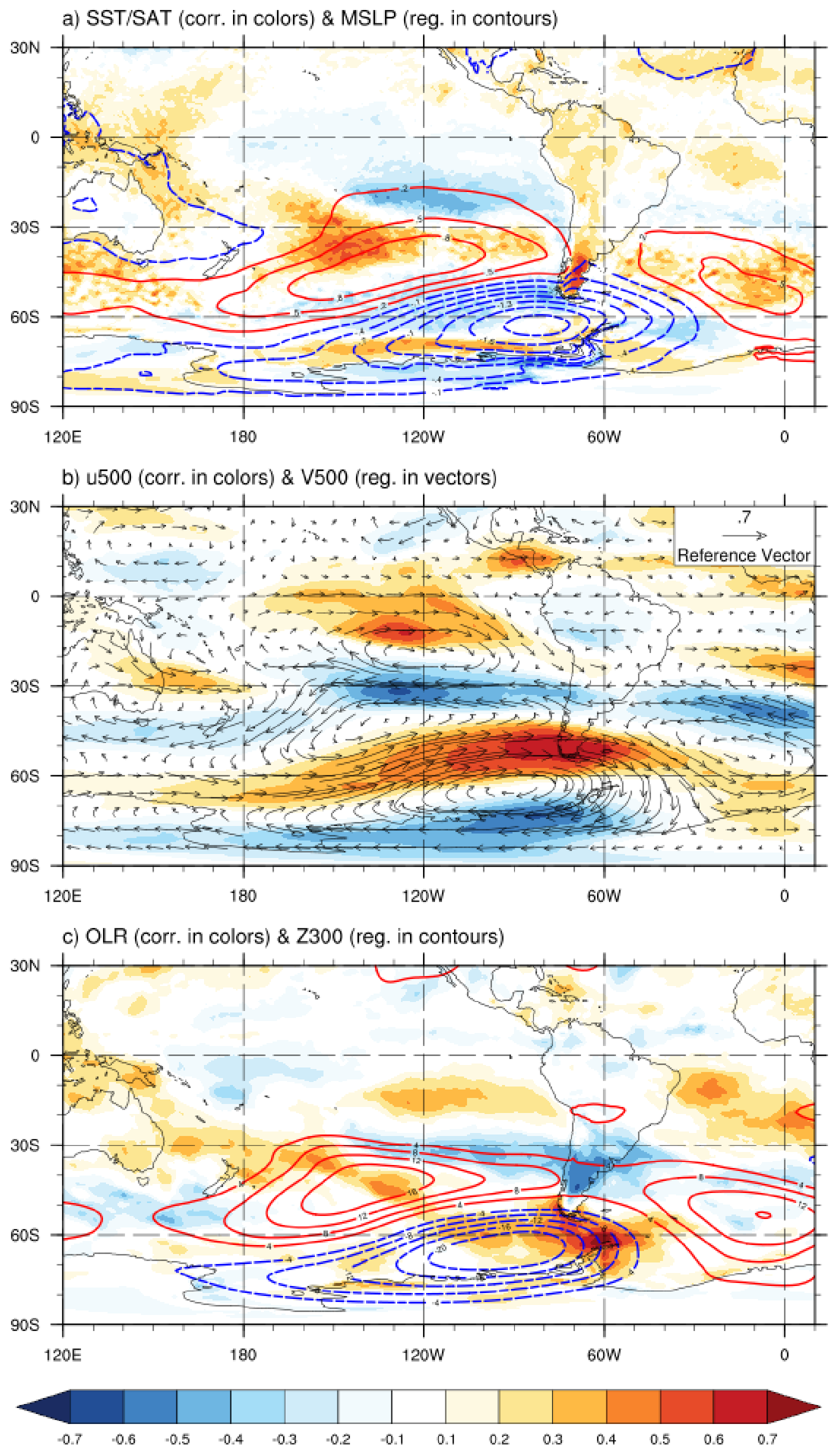

Figure 29. The same as in Fig. 28 but for the glaciological winter (April to November).

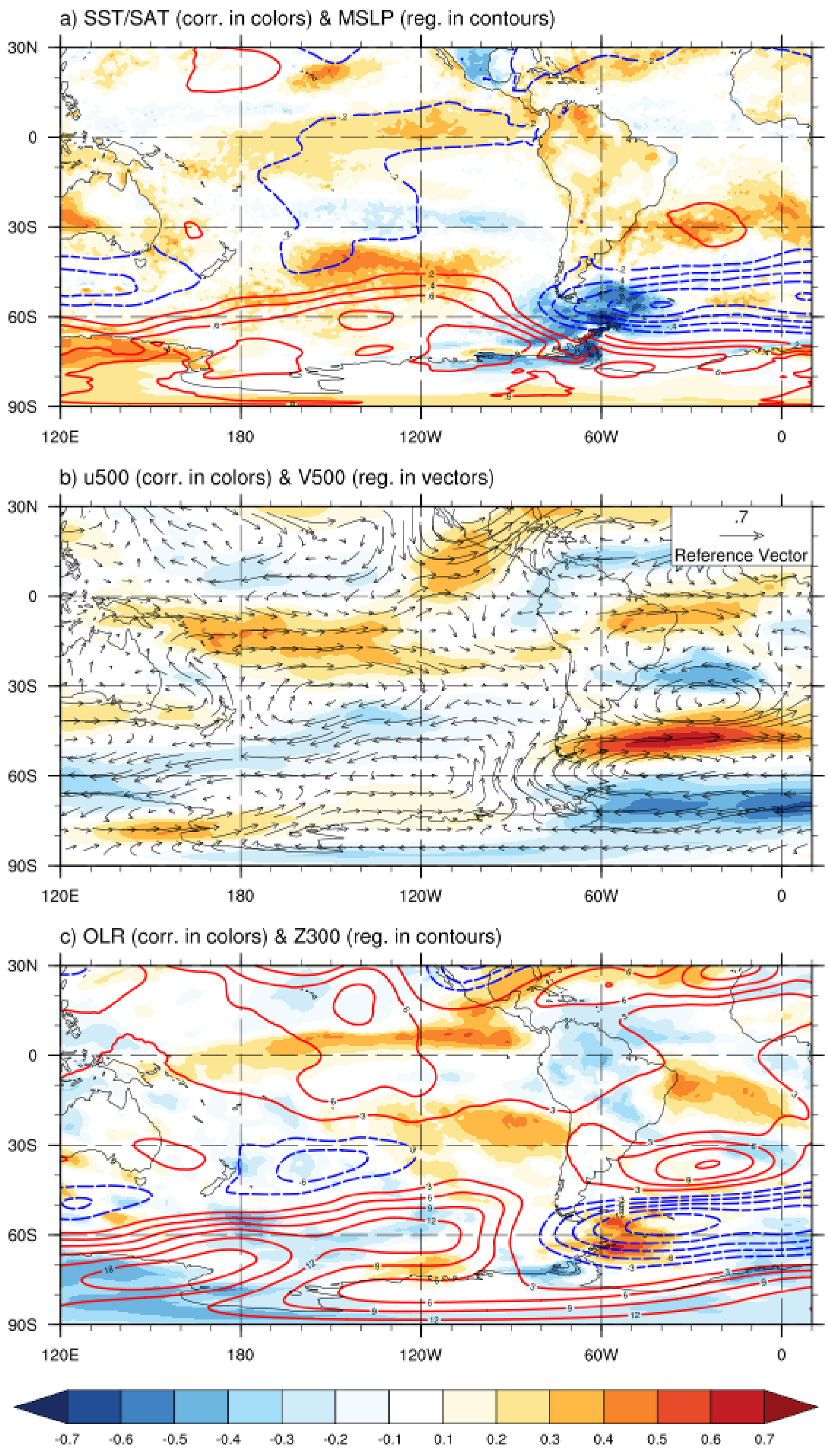

Figure 30. The same as in Fig. 28 but for the glaciological summer (December to March).

In winter, a deep low-pressure system extends from the Drake Passage to the Amundsen Sea and the western Weddell Sea (180°W-50°W), alongside a high-pressure system in the south-central Pacific Ocean (160°E-90°W; 60°S-30°S). These systems enhance westerly winds over southern South America (Fig. 29b), fostering cyclonic circulation over Drake Passage and precipitation over northern AP. Conversely, summer sees a high-pressure system over the Amundsen-Bellingshausen Sea and a low-pressure system in the southern Atlantic Ocean (Fig. 30a), promoting airflow from the Weddell Sea and regional cooling in the northern AP region.

6.5.6 Correlation with large and regional scales indices

Table 8 shows the correlations between different large-regional scale climate indices and the SMB, temperature, and snowfall from SSI_RACMO time series at annual, winter and summer timescales.

On an annual timescale, large-scale indices such as ENSO and SAM show low and statistically non-significant correlations with the SMB. In contrast, the DC-CPAC ($r = -0.32$, $p<0.05$) index, also considered a large-scale index, shows moderate but statistically significant negative correlations. Regional indices over the Drake Passage show high and moderate negative correlations such as Z500-Drake ($r = -0.46$, $p<0.05$) and SST-Drake ($r = -0.35$, $p<0.05$), followed by the indices over the Amundsen-Bellingshausen and Weddell Seas, such as SST-ABSea ($r = -0.36$, $p<0.05$) and SST-WSea ($r = -0.30$, $p<0.10$), respectively.

On the winter timescale, all of the large-scale indices show low and statistically non-significant correlations. Even several regional-scale indices associated with SST over the Amundsen-Bellingshausen, Weddell, and Drake Seas region show low correlations with the SMB. Only the regional Z500-Drake index shows a statistically moderate negative correlation ($r = -0.48$, $p<0.05$) with the winter SMB.

On the summer timescale, large-scale indices show statistically significant positive and negative correlations such as El Niño 3 ($r = 0.37$, $p<0.05$), El Niño 3.4 ($r = 0.36$, $p<0.05$), El Niño 4 ($r = 0.29$, $p<0.10$) and SAM ($r = -0.37$, $p<0.05$) with the summer SMB. In addition to the large-scale indices, regional-scale indices show high and moderate negative and positive correlations such as Z500-Drake SST-Drake (r = -0.60, p<0.05), (r = -0.35, p<0.05), SST-WSea (r = 0.43, p<0.05), SST-ABSea (r = -0.41, p<0.05) and, ASL (r = 0.33, p<0.05).

Applying an exponential filter to the SMB and climate indices, we observed that Drake-related indices increase their correlation, e.g. Z500-Drake (r = -0.53, p<0.05) and SST-Drake (r = -0.42, p<0.05) at the annual timescale (Table S9), indicating that on a decadal scale the SSI SMB variability is also mainly related to anomalies in the atmospheric circulation and SST over the Drake region. Thus, from annual to decadal timescales, negative atmospheric pressure anomalies over the Drake are related to positive SSI SMB anomalies. Conversely, positive SST anomalies over Drake lead to negative SSI SMB anomalies. DC-CPAC also increases its correlation with the annual SMB (i.e., r = -0.45, p<0.05), indicating that negative deep convection anomalies over the central tropical Pacific can drive positive SMB anomalies in SSI.

Table 8**.** Annual (April to March), winter (April to November) and summer (December to March) correlation analysis of surface mass balance (SMB), air temperature (Temp) and snowfall anomalies from SSI_RACMO time series with large-regional climatic indices from 1980 to 2019. Significance is indicated by an asterisk, where * (p<0.10) and ** (p<0.05).

	Annual correlation			Winter correlation			Summer correlation		
	SMB	TEMP	SNOWFALL	SMB	TEMP	SNOWFALL	SMB	TEMP	SNOWFALL
NIÑO 3	0.21	-0.34**	-0.08	-0.2	-0.24	-0.17	0.37**	-0.48**	0.25
NIÑO 3.4	0.21	-0.43**	-0.02	-0.2	-0.36**	-0.15	0.36**	-0.48**	0.24
NIÑO 4	0.13	-0.48**	-0.07	-0.23	-0.44**	-0.19	0.29*	-0.42**	0.21
DC-CPAC	-0.32**	-0.32**	-0.21	-0.19	-0.24	-0.13	-0.11	-0.05	-0.27*
SAM	-0.11	0.45**	0.21	0.06	0.54**	0.1	-0.37**	0.34**	-0.36**
ASL	0.17	-0.7**	-0.19	-0.19	-0.81**	-0.16	0.33**	-0.39**	0.22
SST-ABSea	-0.36**	0.26	-0.18	0.02	0.39**	-0.0	-0.41**	0.32**	-0.33**
SST-WSea	-0.3*	0.69**	-0.1	0.17	0.6**	0.14	-0.43**	0.53**	-0.01
Z500-Drake	-0.46**	0.28*	-0.54**	-0.48**	0.39**	-0.56**	-0.35**	0.21	-0.45**
SST-Drake	-0.35**	0.58**	-0.13	0.05	0.67**	0.06	-0.6**	0.5**	-0.24

6.5.7 Atmospheric rivers impact on SMB

To investigate the impact of ARs on the SSI SMB, we analyzed the correlation between AR frequency and SMB from SSI_RACMO time series during winter and summer from 1980 to 2019 (Fig. 31). The results reveal two distinct impacts of ARs on the glacier SMB of the SSI (Table 9). Firstly, during winter (Fig. 31a), a positive and significant correlation between AR frequency and SMB is observed ($r = 0.43$, $p<0.05$), indicating that ARs contribute to glacier accumulation through increased snowfall. However, higher correlations were observed when JJA ($r = 0.68$, $p<0.05$) is considered only. Secondly, during summer (Fig. 31b), a negative and significant correlation between AR frequency and SMB is observed ($r = -0.37$, $p<0.05$), suggesting that ARs intensify glacier melting in this season. Furthermore, when an exponential filter is applied to see decadal variations, the seasonal correlations increase (Table S10). These findings align with the regional temperature patterns: the winter temperatures during the ARs remain below the melting point, facilitating significant snowfall and glacier accumulation triggered by moisture transported by ARs. In contrast, summer temperatures approach or exceed the melting point, allowing ARs to amplify temperatures by means of sensible heat transport and enhance glacier melting. On an annual timescale, AR frequency and SMB present a negative but non-significant correlation ($r = -0.17$, non-significant), indicating that ARs contribute to glacier melting in this region.

For further analysis of the impact of ARs, we identified 20 cases associated with ARs based on the 99th percentile for winter snowfall and summer temperature from 1980 to 2019, using the daily GLAS_COSIPY time series. We then selected two cases out of these 20 with the highest positive and negative SMB values. These cases were observed on June 26, 1988, and January 23, 2006. Using ERA5 reanalysis data, we analyzed them to further illustrate the AR influences with the aid of the SMB, snowfall, rainfall, temperature, and sensible heat.

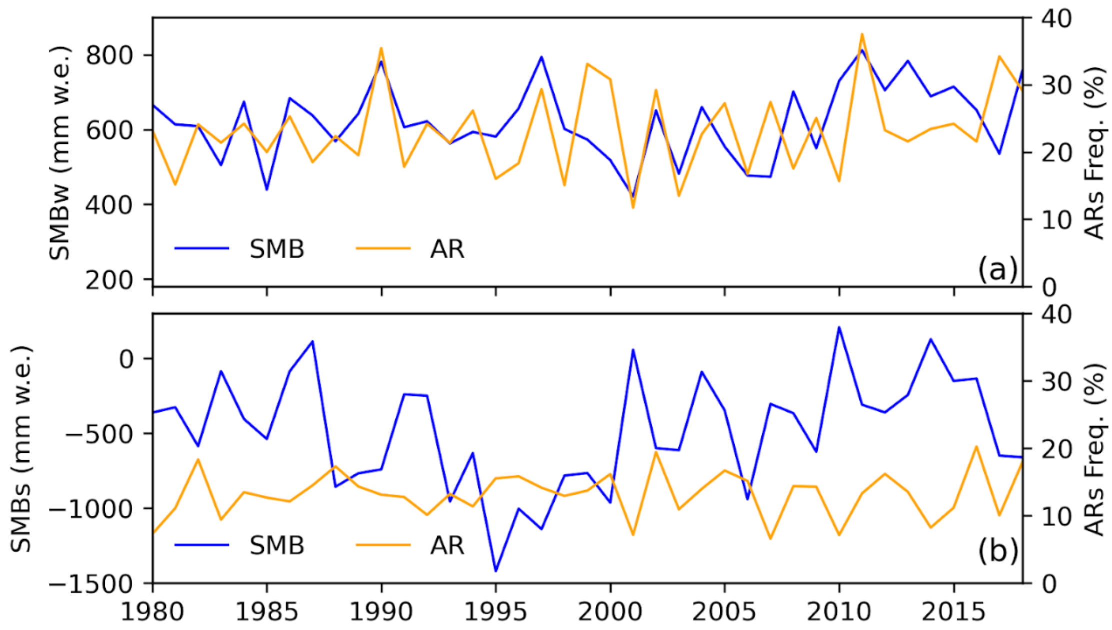

Figure 31. (a) winter (April to November) and (b) summer (December to March) surface mass balance (blue line) from SSI_RACMO time series vs Atmospheric Rivers Frequency (orange line) from 1980 to 2019.

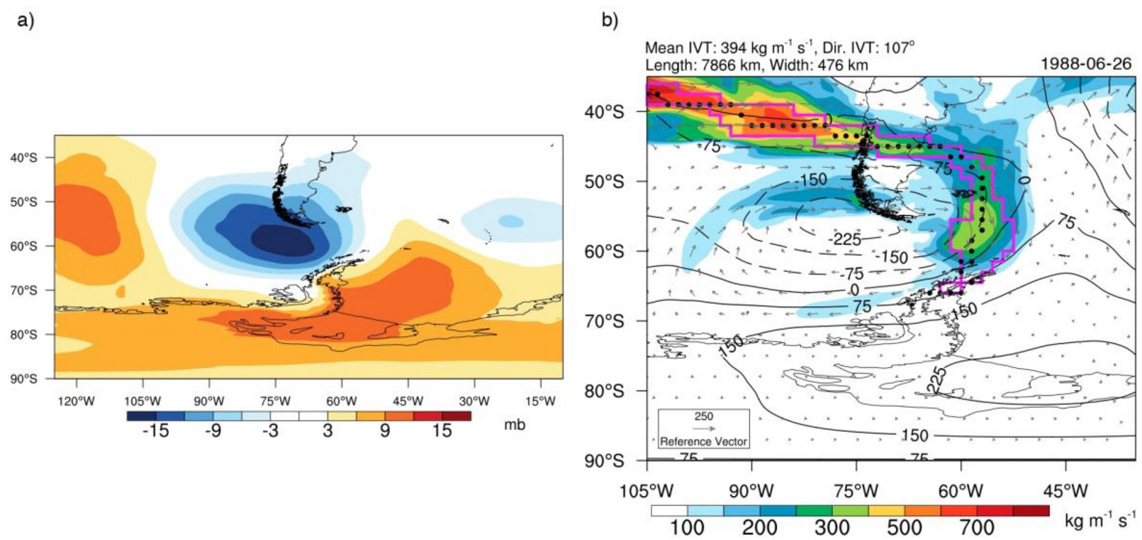

Figure 32. (a) Composite daily anomalies MSLP for the selected AR days in winter (April to November) for the 1970-2020 period. (b) Characteristics of the extreme AR event detected on June 26, 1988, 12:00 UTC with IVT (shaded), IVT vectors, and 500 hPa geopotential height anomalies (contours) on that day. Black full circles show the axis of the AR.

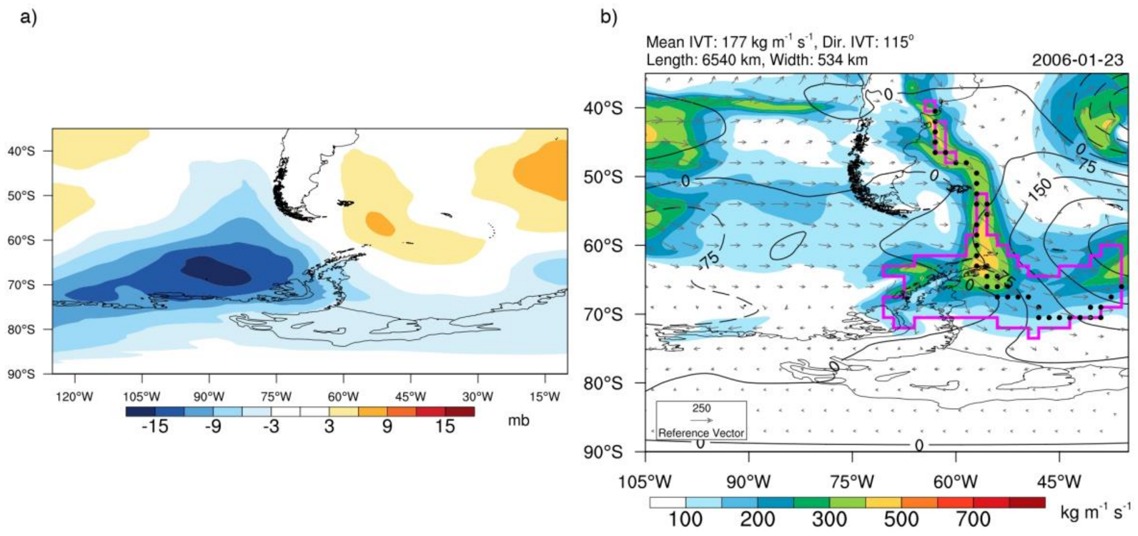

Figure 33. (a) Composite daily anomalies in MSLP for the selected AR days in summer (December to March) for the 1970-2020 period. (b) Characteristics of the extreme AR event detected on January 23, 2006, 12:00 UTC with IVT (shaded), IVT vectors, and 500 hPa geopotential height anomalies (contours) on that day. Black full circles show the axis of the AR.

During the June 1988 case, axes with the same tracking ID in the life cycle show that AR had a northern-southern propagation axis, starting in the eastern Pacific Ocean and ending mainly in the northern AP. In addition, the AR in the life cycle had a northwest-southwest orientation (IVT direction of 107°) with a mean IVT of 394 kg m^{1} s^{1} and a length of 7866 km (Fig. 32b). A low-pressure system over the Drake Passage and a high-pressure system over the northern Weddell Sea were observed during the AR event, which allowed the transport of moisture from the Pacific Ocean to the northern AP. We highlight that the high-pressure system over the Weddell Sea is of great importance for the AR to enter perpendicularly over the northern AP. The MSLP composite analysis for the selected winter days (see Table S11) shows the same synoptic circulation pattern (Fig. 32a). During this AR period, the daily SMB was positive with a value of 30 mm w.e./day, the total precipitation was only snowfall (31 mm w.e./day), the surface temperature was below the melting point (-2.67 °C), and the sensible heat flux decreased moderately (14 W/m^2) compared to mean daily climatological (27 W/m^2).

Table 9. Annual (April to March), winter (April to November) and summer (December to March) correlation for SMB, T2, and Snowfall from SSI_RACMO time series with ARs frequency from 1980 to 2019.

	Annual correlation	Winter correlation	Summer correlation	MAM	JJA	SON	DJF
SMB	-0.17	0.43**	-0.37**	-0.42**	0.68**	0.3*	-0.39**
TEMP	0.56**	0.67**	0.56**	0.75**	0.7**	0.61**	0.4**
SNOWFALL	0.21	0.42**	-0.22	-0.03	0.64**	0.22	-0.16

During the January 2006 case, axes with the same track ID in the life cycle show that AR had a northern-southern propagation axis, starting in the South American continent and ending mainly in northern AP and the Weddell Sea, unlike the June 1988 case which started in the Pacific Ocean. AR in the life cycle had a northwest-southwest orientation (IVT direction of 115°) with a mean IVT of 177 kg m^1 s^1 and a length of 6540 km (Fig. 33b). A high-pressure system over the northern Weddell Sea was also observed during the AR event, which allowed the transport of continental air masses from South America to the northern AP and Weddell Sea. The high-pressure system during the summer is also observed in the MSLP composite analysis (Fig. 33a). During this AR event, the environmental conditions were favorable for a very negative SMB of -34 mm w.e./day, accompanied by positive temperature (3.57 °C), null total precipitation (snowfall + rainfall) and the sensible heat flux increased considerably (71 W/m^2) compared to mean daily climatological (27 W/m^2) (Table S11).

The analysis of these two extreme cases suggests that ARs can influence the SMB of glaciers in the SSI. On the one hand, during winter, ARs can contribute to large amounts of snowfall, which favors positive SMB. On the other hand, during summer, ARs increase the temperature of the northern AP, combined with null precipitation and high sensible heat fluxes, creating favorable conditions for high melt rates and extremely negative SMB values.

Generally, the synoptic patterns of these two events are similar to the general pattern of the other extreme cases (20 cases, see Table S11), suggesting that the two selected main cases can be treated as representative of a larger sample size. During these events, there was typically a high-pressure center over the northern Weddell Sea (Figs. 32a and 33a) with a low-pressure center over the Drake Passage during winter or over the Amundsen-Bellingshausen Sea during summer.

6.6 Discussions

6.6.1 Glaciological modelling limitations

Despite uncertainties in the model and ERA5 climate data, PDD, COSIPY and RACMO effectively captured interannual and seasonal variability in glacier SMB. Sensitivity analysis revealed that COSIPY's key free parameters and uncertainties in meteorological inputs do not significantly affect the estimated SMB interannual variability (Tables S12, S13, and S14). Uncertainties in annual SMB variability may be associated with poor representation in the ERA5 reanalysis of precipitation fields across Antarctica (Roussel et al., 2020). Future atmospheric and glaciological modelling efforts should prioritize increasing the spatial resolution of the models to better represent local topography, orographic precipitation, and improve SMB modelling.

From the intercomparison of the different models (PDD, COSIPY, and RACMO), it is apparent that RACMO, despite its distributed configuration, does not exhibit significant changes in the interannual and seasonal variability of the SMB. Therefore, whether using a single-point or distributed model configuration does not impact the final glacier-wide SMB results for the SSI.

The SMB terminology is used to observe climate-related changes on glacier surfaces, excluding impacts from calving and/or frontal ablation processes (Cogley et al., 2011).

Therefore, SMB is expected to vary little from glacier-to-glacier over short distances like those on the SSI. This is noted with high annual and seasonal correlation of the SMB observed between the three glaciers (Johnsons, Hurd and Bellingshausen), indicating that the SMB's annual and seasonal variability is consistent across these glaciers (Table S15). However, if we consider the geodetic mass balance, variations in mass balance are significant and can highly influence glacier-to-glacier mass changes over the SSI and northern AP (e.g., Shahateet et al., 2021; Seehaus et al., 2023).

Several factors limit the feasibility of distributed glaciological simulations for the studied glaciers. First, the absence of point SMB observations for these three glaciers makes a spatial evaluation of the models impossible. Second, Johnsons, Hurd, and Bellingshausen glaciers are very small, and a single grid from ERA5 or RACMO covers the entire glacier. Consequently, local-scale atmospheric processes are not well represented in ERA5, as evidenced by systematic errors in some atmospheric variables such as RH2, WS, and total precipitation (see Figs. S1 and S2). Third, since most glaciers in the SSI are in equilibrium with small or negligible annual mass balances, using the centroid as a reference point to simulate the SMB for the entire glacier is a reasonable approach. Finally, our simulation covered 51 years, and conducting very high-resolution simulations (both spatially and temporally) over this period would be prohibitively costly. For meaningful distributed glaciological simulations, it is essential to represent local atmospheric processes more accurately, possibly using models like the PWRF. Or, a mass balance method based on machine learning can (1) help improve the downscaling of the variables distributed in a glacier, (2) implicitly include glacial ice dynamics processes and (3) accelerate the execution of the model to run it at high resolution. However, such detailed modelling or use of machine learning falls outside the scope of our current study.

Our results align with other SMB studies in the region, though there are some differences in the findings. For example, Navarro et al. (2013) reported a mean SMB value of -50 ± 100 mm w.e./year for Hurd and Johnsons glaciers during the 2002-2011 period, while our findings show SMB values of 158 ± 320 mm w.e./year for SSI in the same period. Recently, Shahateet et al. (2021) reported a slightly negative mass balance (-106 ± 7 mm w.e.) for 2013-2017, contrasting our positive SMB (368 ± 272 mm w.e.). This difference may arise from glacier mass losses due to calving, a factor not included in the glaciological models used in this study. However, given the relative difference, it is reasonable to conclude that mass balance changes in this region are primarily driven by surface processes influenced by climate. Thus, although glacier-wide SMB is also influenced by glacier hypsometry and ice dynamics over the SSI, the influence of climate can still be extracted from it (Zekollari et al., 2020; Bolibar et al., 2022).

6.6.2 SMB sensitivity and trends

Our sensitivity analysis reveals temperature, followed by snowfall, predominantly influences the interannual variability of these glacier's SMB (Tables S8 and S14). In contrast, solar radiation has a minimal effect. Correlation analysis indicates that ablation predominantly drives interannual SMB variations, followed by accumulation (Table S7). These findings are consistent with previous research highlighting the high sensitivity of these glaciers to small temperature fluctuations (e.g., Bintanja, 1995; Braun and Hock, 2004; Jonsell et al., 2012). For example, Jonsell et al. (2012) found that a temperature increase (decrease) of 0.5 °C implies an increase (decrease) in melting rates by approximately 56% (44%). This high sensitivity is attributed to the limited elevational range of these glaciers, resulting in temperatures near freezing during summer and thus a heightened response to minor temperature changes during melt seasons.

We identified a significant shift in the annual SMB trend around 1999. From 1980 to 1997, the SMB trend was significantly negative, indicating surface mass loss. However, from 1999 to 2014, the trend turned significantly positive, suggesting surface mass gain. However, a declining trend has emerged in recent years, from 2015 to 2019. These findings align with Oliva et al. (2017), who noted a slowed recession of marine and land-terminating glaciers in northern AP during the 2000s. This change in SMB trends aligns with documented regional temperature shifts, identified as the main driver of the glaciers' interannual variability (Turner et al., 2016, 2020; Oliva et al., 2017; Bozkurt et al., 2020; Bello et al., 2022). For example, Bello et al. (2022) reported warming and cooling periods before and after 2000 over King George Island, the largest island in SSI.

6.6.3 Relationship between large an regional climate indices and the SMB

We highlight that the Drake Passage significantly influences the annual SMB of SSI glaciers. At the annual timescale, regional climate indices such as Z500-Drake ($r = -0.46$, $p<0.05$) and SST-Drake ($r = -0.35$, $p<0.05$) show a moderate negative correlation with SMB. For winter, Z500-Drake ($r = -0.48$, $p<0.05$) emerges as a potential influencing factor of SMB variability. During summer, a high and moderate negative correlation exists between SMB and SST-Drake ($r = -0.60$, $p<0.05$) and Z500-Drake ($r = -0.35$, $p<0.05$). We suggest that low-pressure anomalies over the Drake region (known as the Drake low) is a key driver of precipitation variability affecting both the Patagonia Icefields and SSI (Fig. 26a). Recent studies have indicated that the Drake low is a major controller of SMB variability over Patagonia Icefields (Carrasco-Escaff et al., 2023) and precipitation over the SSI (Torres et al., 2023). In addition, we speculate that Drake low can control regional temperature variability over the SSI due to the advection of cold air from Weddell to the northern AP (Fig. 27c), when it positions itself east of SSI. Our findings gain support through a correlation analysis of SMB between the Patagonia

Icefields (time series from Carrasco-Escaff et al., 2023) and the SSI. We found a low correlation between SMB-Patagonia-Icefields and SMB-SSI during annual ($r = 0.30$, $p<0.05$) and summer ($r = 0.18$, $p<0.05$), while a high correlation is observed during winter ($r = 0.58$, $p<0.05$). These results suggest winter SMB may be largely governed by the Drake low, whereas in summer and annually, the Drake low positioned over the northern Weddell Sea and DC-CPAC also play significant roles.

The annual SMB of SSI glaciers moderately depends on DC-CPAC climate indices, but shows less dependence on larger-scale climate patterns like SAM and ENSO. Interestingly, the summer SMB has a moderate dependence on ENSO, suggesting its significant influence during this period. Similar to Donat-Magnin et al. (2020), who indicated that the summer SMB and surface melting over the drainage basins of the Amundsen Sea glaciers, West Antarctica, are low influenced by ENSO. ENSO also shows a seasonally varied effect with a negative correlation in winter and a positive correlation in summer with SSI SMB (see Table 8). However, it shows a low dependence on DC-CPAC ($r = -0.05$, not-significant) but a moderate dependence on Z500-Drake ($r = -0.45$, $p<0.05$). The correlation between summer surface melting on the SSI and DC-CPAC ($r = 0.13$, not-significant) exhibits low dependence. Compared to the results of Clem et al. (2022), who identified DC-CPAC as a major influence on surface melting at the Larsen C Ice Shelf in eastern AP, we suggest that in the complex climate of SSI, DC-CPAC's effects are likely overshadowed by other regional climate drivers, such as the low-pressure system over the Drake Passage.

Additionally, we used the observed and modelled SMB (COSIPY and RACMO) to relate to different climate indices (i.e., ENSO, SAM, ASL, Drake) from 2002 to 2019. The results indicate a similar correlation with these climate forcing indices (Table S16 and S17). For example, ENSO and SAM show low correlations with the observed and modelled SMB (either COSIPY or RACMO). Whereas, the Drake low indices (i.e., Z500-Drake and SST-Drake) indicate high-moderate correlations with both observed and modelled SMB. These analyses suggest that, regardless of whether the SMB is observed or modelled, the results and conclusions remain consistent.

6.6.4 ARs' impact on SMB

The impact of ARs on the SMB in the SSI varies with the season. During the austral winter months, ARs from the Pacific Ocean, carrying warm and moist air, increase snowfall and contribute positively to the SMB. In contrast, during the austral summer, ARs originating from the Pacific Ocean and southern South America with warm air masses can enhance surface melting on glaciers in this region due increase of the sensible heat flux. The direction of ARs is also crucial in which west-to-east ARs impact the northern AP less than the central-south AP. In contrast, northwest-to-southwest ARs dominated by meridional winds affect the entire AP significantly. For instance, on January 23, 2006, a high-pressure system over the northern Weddell Sea led to a high ablation rate in the SSI. This pattern aligns with findings by Zou et al. (2023), who noted the northern AP's vulnerability to ARs combined with atmospheric blocks over the Weddell Sea. Our study emphasizes the role of low-pressure systems in the Drake Passage and the Weddell Sea in enhancing SMB, whereas high-pressure systems in these areas can cause significant SMB reduction. Consistent with these results, Braun et al. (2001) reported that the SSI's highest surface melt rates (up to 20 mm w.e./day) occurred during northwestern advection events linked to low-pressure over the Bellingshausen Sea. They also found that easterly and southerly cold, dry air masses, influenced by high-pressure over the AP and low-pressure over the Weddell Sea, had minimal impact on ablation rates.

In addition, during summer, the presence of these high- or low-pressure systems can modulate the frequency of snowfall or rainfall over northern AP (Wang et al., 2021). When the low-pressure center is located over western Drake with a high-pressure system over the Falkland Islands, it can favor the frequency of rainfall over northern AP. When the low-pressure center is located west-central over Drake, accompanied by a low-pressure system over the Weddell Sea, it may favor more frequent snowfall over the SSI.

6.6.5 Tropical Forcings on the SSI environmental conditions

The interannual variability of SMB in the SSI is largely governed by surface and atmospheric pressure anomalies and SST anomalies over the Drake Passage, influenced by tropical forces like ENSO and DC-CPAC. It is plausible to suggest that tropical forcings alter sea surface and atmospheric conditions at regional scales over the AP, affecting the SSI’s SMB. Subsequently, these regional changes strongly control the SMB of the SSI. While our study does not delve into the specific mechanisms behind Drake pressure anomalies, they're probably impacted by tropical forces and regional temperature variations (e.g., Hoskins & Karoly 1981; Karoly 1989; Carrasco-Escaff et al., 2023; Clem et al., 2022; Gorodetskaya et al., 2023). Studies like Carrasco-Escaff et al. (2023) suggest that Drake low's formation is sensitive to SST anomalies in the tropical Pacific, influencing precipitation and SMB in the Patagonia Icefields. Recent findings, indicate complex interactions, like Rossby waves influencing the AP's climate through synoptic scale circulation anomalies such as intensification of ASL and strengthened high pressure over Drake Passage (e.g., Rondanelli et al., 2019; Clem et al., 2022; Gorodetskaya et al., 2023). These insights highlight the need for further research to fully understand the teleconnections affecting the Drake atmospheric circulation anomalies.

We found that at the interannual scale, ASL is strongly related to SAM ($r = -0.74$, $p<0.05$) (Table S18). However, at the decadal scale, ASL shows a stronger relationship with El Niño 4 ($r = 0.65$, $p<0.05$) (Table S19), indicating that positive surface temperature anomalies over the tropics lead to positive ASL anomalies. According to Li et al. (2021), during El Niño events, there is typically a weakening of the ASL, which can induce cooling in the AP of up to 1.5°C and positive anomalies in sea ice concentration of up to 10-20% in the vicinity of the Amundsen, Bellingshausen, and Weddell Seas. We also found that the Z500-Drake index shows low correlation with the large-scale climate indices (ENSO and SAM) but moderate and significant correlation with SST-ABSea ($r = 0.38$, $p<0.05$). This would indicate that pressure anomalies over Drake can be associated with sea surface temperature anomalies over the Bellingshausen Sea. However, further analysis of these relationships is needed to identify which drivers influence the atmospheric pressure anomalies over Drake.

6.7 Conclusions

This study explored the climatic influences on the SMB of SSI glaciers on seasonal and interannual timescales. Employing the RACMO and COSIPY glaciological models, we obtained robust SMB time series for SSI glaciers. We then analyzed detrended SMB anomaly time series against climate variables to understand their relationship with key atmospheric modes of variability at the interannual timescale. Additionally, we assessed the impact of AR events on the seasonal SMB of SSI glaciers, shedding light on various climate processes at different scales affecting SMB. Key conclusions include:

- **Interannual SMB Variability:** Near-surface temperature and precipitation mainly drive the interannual variability of SSI glaciers' SMB, while insolation has minimal impact.

- **Local-Scale Conditions:** Years with higher-than-average SMB correlate with increased annual accumulation and reduced summer ablation, linked to more annual precipitation and lowered summer near-surface temperatures. Lower-than average SMB years show the opposite conditions.
- **Break in SMB Trends:** A notable shift in the SMB trend aligns with regional warming and cooling trends of the AP. A significant negative SMB trend was observed in the 1970-1997 period, followed by a significant positive trend in the 1999-2014 period. Since 2015, there has been a trend towards extremely negative SMB rates.
- **Positive/Negative SMB years:** Positive SMB years are associated with low-pressure systems over Drake Passage (known as the Drake low), enhancing winter snowfall and cooling the northern AP in summer. Negative SMB years are linked to high-pressure systems over the Weddell Sea in summer, leading to increased surface ablation due to meridional winds.
- **Climate Variability Modes:** Interannual SMB variability shows little correlation with major climate modes like SAM and ENSO, though these may moderately influence summer SMB. ENSOs' effects on SMB vary seasonally. Interannually, ESNO positive (during El Niño events) and DC-CPAC (negative anomalies) are associated by slightly positive SMB anomalies in SSI.
- **AR Events Impact:** ARs' effects on SMB vary seasonally. Winter ARs typically lead to positive SMB conditions, while summer ARs can have a negative impact. Typically, these ARs feature low pressure anomalies over the Amundsen-Bellingshausen Sea in summer and the Drake Passage in winter, accompanied by high pressure over the Weddell Sea, leading to prevalent meridional winds.

Our study gives new insights into the complex interplay between current climate processes and cryospheric dynamics in island glaciers on the northern Antarctic Peninsula. We underscore that the interannual SMB variability in these glaciers is largely responsive to SST anomalies and surface and atmospheric pressure anomalies over the Drake Passage and northern Weddell Sea. Specifically, negative atmospheric pressure anomalies over the Drake Passage are correlated with positive SSI SMB anomalies. Conversely, positive SST anomalies over the Drake Passage result in negative SSI SMB anomalies. Furthermore, we highlighted the need for further glacier-climate studies to delve into the seasonal and intraseasonal impacts of various climate forcings and ARs on the AP environment, particularly on small-scale glaciers along the coastal zone.

Acknowledgments

We express gratitude to the Aperfeiçoamento de Pessoal de Nível Superior (CAPES) for supporting the Graduate Program in Oceanology at Universidade Federal do Rio Grande (FURG). The first author also acknowledges CAPES for the PhD scholarship. Special thanks to ECMWF for providing ERA5 data and JM van Wessem for RACMO data. We also appreciate Francisco Navarro for insightful discussions on this research. The data (KOPRI-KPDC-00000960) from King Sejong Station used in this work was provided by the Korea Polar Research Institute. Powered@NLHPC: This research/thesis was partially supported by the supercomputing infrastructure of the NLHPC (CCSS210001). DB acknowledges support from ANID-FONDECYT-1240190, ANID-FONDAP-1523A0002, and COPAS COASTAL ANID FB210021. Finally, we extend our thanks for the SCAR fellowships (https://www.scar.org/general-scar-news/2022-scar-fellows/) that enabled the first author to conduct a research exchange at the University of Valparaíso, Chile.

Author Contributions

Christian Torres: Conceptualization, Methodology, Software, Validation, Writing - original draft preparation **Deniz Bozkurt:** Conceptualization, Methodology, Software, Reviewing and Editing **Tomás Carrasco-Escaff:** Software, Reviewing and Editing **Jordi Bolibar:** Methodology, Reviewing and Editing **Jorge Arigony-Neto:** Conceptualization, Supervision, Reviewing and Editing.

Chapter VII: Summary of Discussion and Conclusions

In this section, we highlight the main points of discussions in the scientific articles presented in Chapters V and VI. Firstly, the articles will be discussed one by one, according to their topic. Then, the general conclusion of the Thesis is presented. Finally, final considerations and perspectives for future work also are presented.

7.1 Summary of Discussions

7.1.1 Temperature and precipitation and their climate relationship

The interannual variability of temperature over the SSI is mainly controlled by ASL and moderately controlled by large-scale climatic modes such as ENSO and SAM. Seasonally, we observed that the influence of ENSO on SSI temperature is most pronounced during winter and spring seasons, although correlations remain moderate, while SAM is most visible during autumn and can even reach correlations higher than ASL. In general, our results indicate that during El Niño (La Niña) conditions the SSI shows negative (positive) temperature anomalies. In contrast, during the positive (negative) phase of SAM, these islands exhibit positive (negative) temperature anomalies. In addition, the interannual and seasonal variability of temperature over SSI responds strongly to drivers associated with sea surface temperature and sea ice extent. For instance, changes in sea ice extent over the northwestern Weddell Sea region achieve high negative correlations with SSI temperature variability with values up to 93%. Our results are in line with previous studies (e.g., Turn et al., 2016; 2020, Bello et al., 2022).

Studies about the understanding of precipitation variability and its relationship with climatic forcing factors are limited on the SSI. Therefore, the results of this thesis provide new insights into the complex climate systems relationship. We found that the interannual variability of precipitation over this region is mainly controlled by a mesoscale low-pressure system located over the western Drake Passage. The interannual variability of precipitation is negatively correlated with surface or atmospheric pressure anomalies over the Drake region with values of up 70%, indicating that low-pressure systems over the Drake favour precipitation over the SSI. The Drake low represents the average synoptic-scale condition associated with passing frontal cyclones in the Drake Passage.

During spring, ENSO can moderately control precipitation variability with negative correlations, indicating that El Niño (La Niña) conditions can produce negative (positive) precipitation anomalies over SSI. Our results are contrary to those reported by Zhang et al. (2021) who indicated that precipitation decreases under negative ENSO and increases under positive ENSO in the AP and the West Antarctic Ice Sheet. However, recent studies have indicated that depending on the region, ENSO can influence precipitation of the AP. During eastern Pacific-El Niño, precipitation decreases over the entire AP and the Amundsen-Bellingshausen Seas, while during central Pacific-El Niño precipitation decreases mainly over the western AP and increases in the eastern AP (Chen et al., 2023).

On the other hand, SAM in its positive phase may moderately favour more precipitation over SSI during spring too.

7.1.2 SMB and their climate relationship

The SMB is a more complex variable to find high correlations with the climate indices used in this thesis. However, we highlight a low-pressure system that can strongly control the interannual variability of SMB, which is located over the Drake Passage. We find high negative correlations between atmospheric pressure anomalies over this region and the interannual variability of the SMB over SSI, indicating that negative atmospheric pressure anomalies over the Drake may favour a positive SMB of SSI glaciers. During the winter, the Drake low is located over the western Drake Passage, while during the summer this same system is located over the eastern Drake Passage. We argue that the Drake low located over the western favours precipitation over the SSI due to the advection of moist air from the southern Pacific Ocean that contributes to accumulation and the positive SMB over the SSI, while Drake low located in the eastern favours cooling over northern AP due to advection of cold air from the Weddell Sea inhibiting surface melt over SSI.

We found weak influence of ENSO and SAM on the interannual variability of the SSI SMB. Although, during summer these large-scale climate indices can have moderate significant influences on the SMB variability. Positive correlations between ENSO and SSI SMB during summer indicate that El Niño conditions can drive positive SMB on the SSI. Furthermore, the ENSO's effect on the SSI SMB varies seasonally. It is not clear why the signs of the correlation analysis change with negative correlation during winter and positive correlation during summer. The positive correlation can be explained by the AP cooling in El Niño conditions during spring, which can directly impact the temperature variability during the coming summer. However, the negative correlation during winter is not clear. Thus, the impact of ENSO on the precipitation and SMB of the entire AP needs to be analysed in more detail. Regarding SAM, this climatic index is negatively correlated with SSI SMB during summer, indicating that positive SAM (negative) exerts negative SMB (positive).

7.1.3 ARs' impacts on the SSI SMB

The impact of Atmospheric River (AR) events on interannual and seasonal SMB variability has been investigated during this thesis. The main results indicate a double effect on the SMB of these AR events. In winter, a positive correlation suggests ARs boost accumulation through increased snowfall. Conversely, in summer, a negative correlation indicates that ARs intensify glacier melting. Thus, these different impacts may even cancel each other out locally to cause insignificant influence during interannual variability.

7.1.4 What is the significance of the Drake Low?

To define the significance of the Drake Low, we analyzed surface pressure fields for typical days characterized by the presence of a low-pressure system. Know et al. (2019) identified a low-pressure system that moved across the Drake Passage on January 7, 2013. We utilized 6-hourly MSLP data from ERA5 to represent the synoptic conditions in the Drake region. Figure 34 illustrates the pattern of the MSLP fields starting at 00:00 UTC on January 6 and ending at 15:00 UTC on January 7.

The low-pressure system formed at the southern end of Chilean territory on January 6 during the passage of a preceding large low-pressure system moving from west to east (Figure 34a). When this large system collided with the South American continent, it created a small low-pressure system over the eastern part of the continent (Figure 34b). This newly generated low-pressure system then moved southeastward, deepening its central pressure over time, and reached the vicinity of the SSI on January 7. The surface pressure at this time was approximately 965-970 hPa, with densely distributed isobars near the SSI at 15:00 UTC on January 7 (Figure 34f).

Know et al. (2019) highlighted that the surface pressure pattern on January 7, 2013, shows large similarity with the MSLP composite map analysis in their Figure 5b. Consequently, we define the Drake Low as a typical synoptic-scale condition associated with passing frontal cyclones in the Drake Passage.

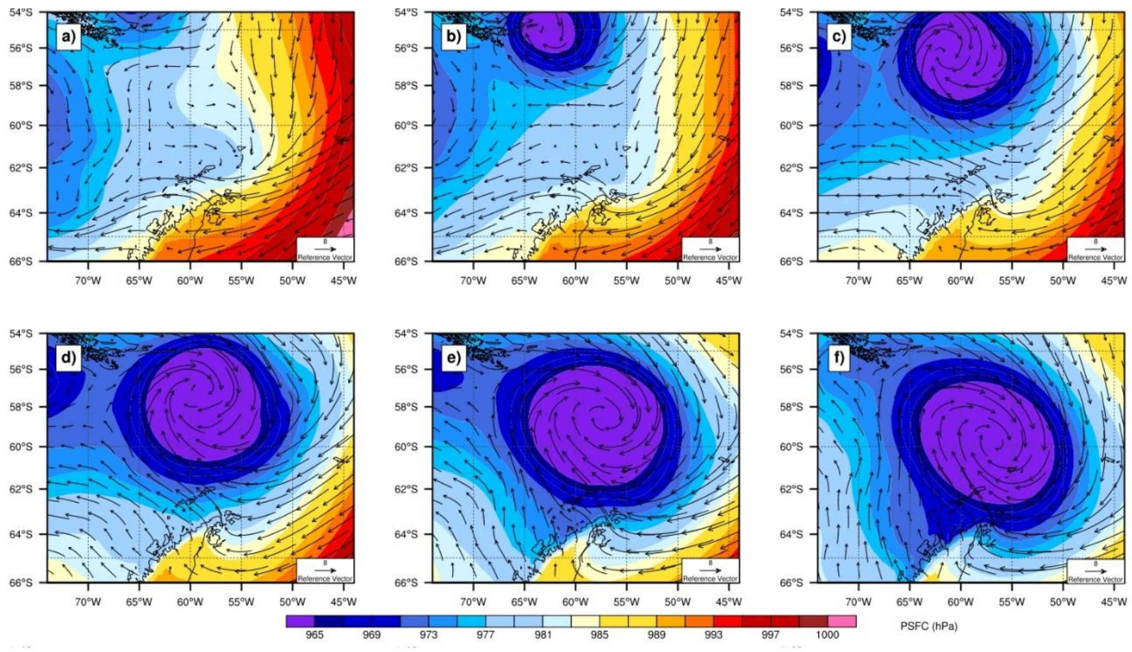

Figure 34. Sea-level pressure (shading, 2 hPa interval) with wind vectors at (a) 1200 and (b) 1800 UTC 6 January 2013, and (c) 0000, (d) 0600, (e) 1200 and (f) 1800 UTC 7 January 2013 from ERA5 reanalysis.

7.1.5 What is the impact of the Drake Low on the climate in the SSI?

We assessed the impact of the Drake Low on local surface meteorological conditions in the SSI using high spatial resolution (5 km horizontal resolution) outputs generated with the PWRF model. We analysed 2 m air temperature, total precipitation and wind speed fields for 15:00 UTC 6 January and 15:00 UTC 7 January (Fig. 35), during the presence of the low-pressure system that moved through the Drake Passage between 6 and 7 January 2013.

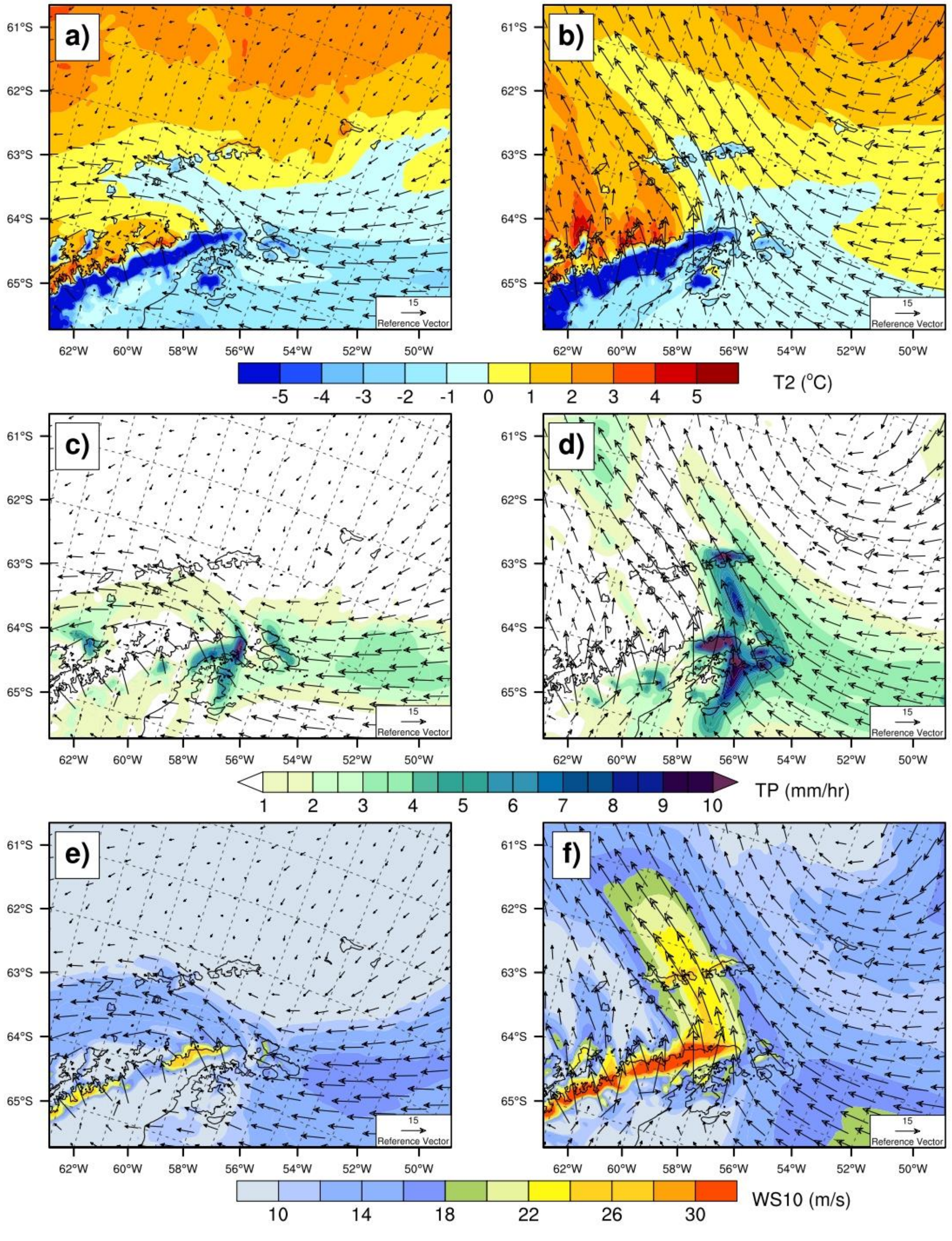

Figure 35. (a,b) 2 m air temperature, (c,d) total precipitation, and (e,f) wind speed with wind vector for a zoomed region over the SSI at (a,c,e) 1500 UTC on 6 January and (b,d,f) 1500 UTC on 7 January 2013 from PWRF simulation with 5 km grid resolution.

At 15:00 UTC on 6 January, the low-pressure system was located north of the SSI. The air temperature was below 0°C (Fig. 35a), mainly over the west of the SSI (Livingston), with precipitation present on the high peaks over the northern AP, including Joinville and James Ross Islands (Fig. 35c). Wind speeds indicated 18 m/s over the western part of the SSI with a predominantly east to west direction (Fig. 35e).

At 15:00 UTC on 7 January, the low-pressure system was positioned over the northeast of the SSI. The air temperature dropped to -2°C (Fig. 35b), with precipitation occurring mainly over the western part of the SSI (Fig. 35d), especially over King George Island, reaching up to 8 mm/h. Wind speed increased considerably, with magnitudes above 22 m/s over most of the SSI region with a predominantly northwesterly direction (Fig. 35f).

Thus, these low-pressure systems affected the meteorological conditions of the SSI, leading to decreased air temperature, intense precipitation, and strong winds. These conditions favoured strong positive surface mass balances of the SSI glaciers. The temperature decrease was attributed to the advection of cold air masses from Weddell Sea by these low-pressure systems when positioned east of the SSI. Meanwhile, the increase in precipitation and wind speed resulted from the combined effect of these synoptic-scale low-pressure systems with the local topography of the SSI and a small part of northern AP.

7.2 Conclusions and Perspectives

In relation to the hypothesis presented and tested in the development of this PhD Thesis, i.e., *"The interannual and seasonal variability of the temperature, precipitation, and surface mass balance (SMB) for glaciers on the Southern Shetland Islands (SSI) is primarily driven by regional-scale climatic forcing factors, notably the ASL and Drake, with low influence from large-scale climatic modes such as ENSO and SAM."*, we can conclude that it was partially accepted. Interannual and seasonal temperature variability is strongly controlled by ASL, and moderately controlled by SAM and ENSO. Whereas, interannual and seasonal precipitation variability is mainly controlled by the Drake low and low influence by SAM and ENSO. Similar to precipitation, the interannual and seasonal variability of SMB is mainly controlled by the Drake low, although during summer, SAM and ENSO may have a moderately significant control.

The glaciological models applied in the development of the thesis are of moderate complexity and may present large uncertainties due to the physical parameterisations and input data used to force them. The implementation of more complex glaciological models that can capture more complex relationships between local climate and glacier dynamics is necessary. Advances in the application of Machine Learning (ML) in glaciology have progressed in recent years. This tool offers an alternative to improve glaciological simulations of these highly dynamic glaciers. Therefore, we recommend the implementation of ML to better represent the changes of AP glaciers and their relationship with climate.

We defined the Drake low as an average synoptic-scale condition associated with passing frontal cyclones in the Drake Passage. These low-pressure systems favour precipitation and cooling over the northern AP including the SSI. Apparently these low-pressure systems are generated when ASL extends into the Bellingshausen Sea. At that time with interaction of westerly winds it generates cyclonic vortices that move across the Drake Passage. However, it is necessary to understand the mechanisms of origin of these low-pressure systems, and how they affect the environmental conditions of northern AP in more detail. Furthermore, it is necessary to better understand how these low-pressure systems relate to large-scale forcing factors such as ENSO and SAM.

Finally, our results on the impact of ENSO on interannual variability of precipitation are not in line with the regional behaviour reported in previous studies, which indicates that El Niño produces positive precipitation and SMB over the AP. It appears that specific regions of the AP such as the SSI show a different behaviour than the western AP. Therefore, a more spatially detailed analysis of the impact of ENSO on precipitation and SMB over AP is required.

Chapter XIII: Bibliography

Arndt, A., Scherer, D., & Schneider, C. (2021). Atmosphere driven mass-balance sensitivity of Halji Glacier, Himalayas. Atmosphere, 12(4), 426. https://doi.org/10.3390/atmos12040426

Bello, C., Suarez, W., & Lavado-Casimiro, W. (2022). Trends and space–time patterns of near-surface temperatures on Maxwell Bay, King George Island, Antarctica. International Journal of Climatology, 42(14), 7426-7442. https://doi.org/10.1002/joc.7661

Bergstra, J., & Bengio, Y. (2012). Random search for hyper-parameter optimization. Journal of machine learning research, 13(2).

Bintanja, R. (1995). The local surface energy balance of the Ecology Glacier, King George Island, Antarctica: measurements and modelling. Antarctic Science, 7(3), 315-325. https://doi.org/10.1017/S0954102095000435

Bozkurt, D., Rondanelli, R., Marín, J. C., & Garreaud, R. (2018). Foehn event triggered by an atmospheric river underlies record-setting temperature along continental Antarctica. Journal of Geophysical Research: Atmospheres, 123(8), 3871-3892.

Bozkurt, D., Bromwich, D. H., Carrasco, J., & Rondanelli, R. (2021). Temperature and precipitation projections for the Antarctic Peninsula over the next two decades: contrasting global and regional climate model simulations. Climate Dynamics, 56(11-12), 3853-3874. https://doi.org/10.1007/s00382-021-05667-2

Bozkurt, D., Bromwich, D. H., Carrasco, J., Hines, K. M., Maureira, J. C., & Rondanelli, R. (2020). Recent near-surface temperature trends in the Antarctic Peninsula from observed, reanalysis and regional climate model data. Advances in Atmospheric Sciences, 37, 477-493. https://doi.org/10.1007/s00376-020-9183-x

Braun, M., Saurer, H., Vogt, S., Simões, J. C., & Goßmann, H. E. R. M. A. N. N. (2001). The influence of large-scale atmospheric circulation on the surface energy balance of the King George Island ice cap. International Journal of Climatology: A Journal of the Royal Meteorological Society, 21(1), 21-36. https://doi.org/10.1002/joc.563

Braun, M., & Hock, R. (2004). Spatially distributed surface energy balance and ablation modelling on the ice cap of King George Island (Antarctica). Global and Planetary Change, 42(1-4), 45-58. https://doi.org/10.1016/j.gloplacha.2003.11.010

Braithwaite, R. J. (1995). Positive degree-day factors for ablation on the Greenland ice sheet studied by energy-balance modelling. Journal of Glaciology, 41(137), 153-160. https://doi.org/10.3189/S0022143000017846

Bromwich, D. H., Rogers, A. N., Kållberg, P., Cullather, R. I., White, J. W., & Kreutz, K. J. (2000). ECMWF analyses and reanalyses depiction of ENSO signal in Antarctic precipitation. Journal of Climate, 13(8), 1406-1420.

Bromwich, D. H., Nicolas, J. P., Monaghan, A. J., Lazzara, M. A., Keller, L. M., Weidner, G. A., & Wilson, A. B. (2013). Central West Antarctica among the most rapidly warming regions on Earth. Nature Geoscience, 6(2), 139-145. https://doi.org/10.1038/ngeo1671

Carrasco, J. F., Bromwich, D. H., & Liu, Z. (1997). Mesoscale cyclone activity over Antarctica during 1991, 1, Marie Byrd Land (Paper 97JD00905). Journal of Geophysical Research-Part D-Atmospheres-Printed Edition, 102(12), 13923-13938.

Carrasco, J. F., Bromwich, D. H., & Monaghan, A. J. (2003). Distribution and characteristics of mesoscale cyclones in the Antarctic: Ross Sea eastward to the Weddell Sea. Monthly Weather Review, 131(2), 289-301.

Carrasco, J. F., & Cordero, R. R. (2020). Analyzing precipitation changes in the northern tip of the Antarctic peninsula during the 1970–2019 period. Atmosphere, 11(12), 1270. https://doi.org/10.3390/atmos11121270

Carrasco, J. F., Bozkurt, D., & Cordero, R. R. (2021). A review of the observed air temperature in the Antarctic Peninsula. Did the warming trend come back after the early 21st hiatus?, Polar Sci., 28, 100653. https://doi.org/10.1016/j.polar.2021.100653

Carrasco-Escaff, T., Rojas, M., Garreaud, R. D., Bozkurt, D., & Schaefer, M. (2023). Climatic control of the surface mass balance of the Patagonian Icefields. The Cryosphere, 17(3), 1127-1149. https://doi.org/10.5194/tc-17-1127-2023

Chen, X., Li, S., & Zhang, C. (2023). Distinct impacts of two kinds of El Niño on precipitation over the Antarctic Peninsula and West Antarctica in austral spring. Atmospheric and Oceanic Science Letters, 16(5), 100387.

Costi, J., Arigony-Neto, J., Braun, M., Mavlyudov, B., Barrand, N. E., Da Silva, A. B., ... & Simoes, J. C. (2018). Estimating surface melt and runoff on the Antarctic Peninsula using ERA-Interim reanalysis data. Antarctic Science, 30(6), 379-393.https://doi.org/10.1017/S0954102018000391

Clem, K. R., & Fogt, R. L. (2013). Varying roles of ENSO and SAM on the Antarctic Peninsula climate in austral spring. Journal of Geophysical Research: Atmospheres, 118(20), 11-481.

Clem, K. R., Renwick, J. A., McGregor, J., & Fogt, R. L. (2016). The relative influence of ENSO and SAM on Antarctic Peninsula climate. Journal of Geophysical Research: Atmospheres, 121(16), 9324-9341.

Clem, K. R., Renwick, J. A., & McGregor, J. (2017). Large-scale forcing of the Amundsen Sea low and its influence on sea ice and West Antarctic temperature. Journal of Climate, 30(20), 8405-8424.

Clem, K. R., Bozkurt, D., Kennett, D., King, J. C., & Turner, J. (2022). Central tropical Pacific convection drives extreme high temperatures and surface melt on the Larsen C Ice Shelf, Antarctic Peninsula. Nature Communications, 13(1), 3906. https://doi.org/10.1038/s41467-022-31119-4

Cook, A. J., Holland, P. R., Meredith, M. P., Murray, T., Luckman, A., & Vaughan, D. G. (2016). Ocean forcing of glacier retreat in the western Antarctic Peninsula. Science, 353(6296), 283-286. https://doi.org/10.1126/science.aae0017

Cullather, R. I., Bromwich, D. H., & Van Woert, M. L. (1996). Interannual variations in Antarctic precipitation related to El Niño-Southern Oscillation. Journal of Geophysical Research: Atmospheres, 101(D14), 19109-19118.

Deb, P., Orr, A., Bromwich, D. H., Nicolas, J. P., Turner, J., & Hosking, J. S. (2018). Summer drivers of atmospheric variability affecting ice shelf thinning in the Amundsen Sea Embayment, West Antarctica. Geophysical Research Letters, 45(9), 4124-4133.

Ding Q, Steig E, Battisti D, Kuttel M (2011) Winter warming in West Antarctica caused by central tropical Pacific warming. Nat Geosci 4:398–403. https://doi.org/10.1038/ngeo1129

Dong, Y., Zhao, J., Li, C., & Liao, M. (2022). Gapless-REMA100: A gapless 100-m reference elevation model of Antarctica with voids filled by multi-source DEMs. ISPRS Journal of Photogrammetry and Remote Sensing, 186, 70-82. https://doi.org/10.1016/j.isprsjprs.2022.01.024

Donat-Magnin, M., Jourdain, N. C., Gallée, H., Amory, C., Kittel, C., Fettweis, X., ... & Agosta, C. (2020). Interannual variability of summer surface mass balance and surface melting in the Amundsen sector, West Antarctica. The Cryosphere, 14(1), 229-249.

Edwards, T. L., Nowicki, S., Marzeion, B., Hock, R., Goelzer, H., Seroussi, H., ... & Zwinger, T. (2021). Projected land ice contributions to twenty-first-century sea level rise. Nature, 593(7857), 74-82.

Falk, U., López, D. A., & Silva-Busso, A. (2018a). Multi-year analysis of distributed glacier mass balance modelling and equilibrium line altitude on King George Island, Antarctic Peninsula. The Cryosphere, 12(4), 1211-1232. https://doi.org/10.5194/tc-12-1211-2018

Fogt, R. L., Bromwich, D. H., & Hines, K. M. (2011). Understanding the SAM influence on the South Pacific ENSO teleconnection. Climate Dynamics, 36(7–8), 1555–1576. https://doi.org/10.1007/s00382-010-0905-0

Fogt, R. L., & Marshall, G. J. (2020). The Southern Annular Mode: Variability, trends, and climate impacts across the Southern Hemisphere. WIREs Climate Change, 11(4). https://doi.org/10.1002/wcc.652

Fogt, R. L., Sleinkofer, A. M., Raphael, M. N., & Handcock, M. S. (2022). A regime shift in seasonal total Antarctic sea ice extent in the twentieth century. Nature Climate Change, 12(1), 54-62. https://doi.org/10.1038/s41558-021-01254-9

Forsch, K. O., Hahn-Woernle, L., Sherrell, R. M., Roccanova, V. J., Bu, K., Burdige, D., ... & Barbeau, K. A. (2021). Seasonal dispersal of fjord meltwaters as an important source of iron and manganese to coastal Antarctic phytoplankton. Biogeosciences, 18(23), 6349-6375.

Genthon, C., Kaspari, S., & Mayewski, P. A. (2005). Interannual variability of the surface mass balance of West Antarctica from ITASE cores and ERA40 reanalyses, 1958–2000. Climate Dynamics, 24, 759-770.

Gonzalez, S., Vasallo, F., Recio-Blitz, C., Guijarro, J. A., & Riesco, J. (2018). Atmospheric patterns over the Antarctic Peninsula. Journal of Climate, 31(9), 3597-3608. https://doi.org/10.1175/JCLI-D-17-0598.1

Gossart, A., Helsen, S., Lenaerts, J. T. M., Broucke, S. V., Van Lipzig, N. P. M., & Souverijns, N. (2019). An evaluation of surface climatology in state-of-the-art reanalyses over the Antarctic Ice Sheet. Journal of Climate, 32(20), 6899-6915. https://doi.org/10.1175/JCLI-D-19-0030.1

Gorodetskaya, I. V., Tsukernik, M., Claes, K., Ralph, M. F., Neff, W. D., & Van Lipzig, N. P. (2014). The role of atmospheric rivers in anomalous snow accumulation in East Antarctica. Geophysical Research Letters, 41(17), 6199-6206.

Gorodetskaya, I.V., Durán-Alarcón, C., González-Herrero, S. et al. (2023). Record-high Antarctic Peninsula temperatures and surface melt in February 2022: a compound event with an intense atmospheric river. npj Clim Atmos Sci 6, 202. https://doi.org/10.1038/s41612-023-00529-6

Guo, Z., Bromwich, D. H., & Hines, K. M. (2004). Modeled antarctic precipitation. Part II: ENSO modulation over West Antarctica. Journal of climate, 17(3), 448-465.

Guan, B., & Waliser, D. E. (2019). Tracking atmospheric rivers globally: Spatial distributions and temporal evolution of life cycle characteristics. Journal of Geophysical Research Atmospheres, 124(23), 12523–12552. https://doi.org/10.1029/2019JD031205

Hersbach, H., Bell, B., Berrisford, P., Hirahara, S., Horanyi, A., Munoz-Sabater, J., et al. (2020). The ERA5 global reanalysis. Quarterly Journal of the Royal Meteorological Society, 146 (730), 1999–2049. https://doi.org/10.1002/qj.3803

Hillebrand, F. L., Bremer, U. F., Arigony-Neto, J., da Rosa, C. N., Mendes Jr, C. W., Costi, J., ... & Schardong, F. (2021). Comparison between atmospheric reanalysis models ERA5 and ERA-Interim at the North Antarctic Peninsula region. Annals of the American Association of Geographers, 111(4), 1147-1159. https://doi.org/10.1080/24694452.2020.1807308

Hoskins, B. J., & Karoly, D. J. (1981). The steady linear response of a spherical atmosphere to thermal and orographic forcing. Journal of the atmospheric sciences, 38(6), 1179-1196. https://doi.org/10.1175/1520-0469(1981)038<1179:TSLROA>2.0.CO;2

Hugonnet, R., McNabb, R., Berthier, E., Menounos, B., Nuth, C., Girod, L., ... & Kääb, A. (2021). Accelerated global glacier mass loss in the early twenty-first century. Nature, 592(7856), 726-731.

Jonsell, U. Y., Navarro, F. J., Bañón, M., Lapazaran, J. J., & Otero, J. (2012). Sensitivity of a distributed temperature-radiation index melt model based on AWS observations and surface energy balance fluxes, Hurd Peninsula glaciers, Livingston Island, Antarctica. The Cryosphere, 6(3), 539-552. https://doi.org/10.5194/tc-6-539-2012

Kwon, H., Park, S. J., Lee, S., Kim, B. M., Choi, T., & Kim, S. J. (2019). A numerical simulation of a strong wind event in January 2013 at King Sejong station, Antarctica. Quarterly Journal of the Royal Meteorological Society, 145(720), 1267-1280.

Karoly, D. J. (1989). Southern hemisphere circulation features associated with El Niño-Southern Oscillation events. Journal of Climate, 2(11), 1239-1252. https://doi.org/10.1175/1520-0442(1989)002<1239:SHCFAW>2.0.CO;2

Kerr, R., Mata, M. M., Mendes, C. R. B., & Secchi, E. R. (2018). Northern Antarctic Peninsula: a marine climate hotspot of rapid changes on ecosystems and ocean dynamics. Deep Sea Res. Part II Top. Stud. Oceanogr, 149, 4-9. https://doi.org/10.1016/j.dsr2.2018.05.006

Knap, W. H., Oerlemans, J., & Cabée, M. (1996). Climate sensitivity of the ice cap of king George Island, South Shetland Islands, Antarctica. Annals of Glaciology, 23, 154-159. https://doi.org/10.3189/S0260305500013380

King, J. C., & Turner, J. (1997). Antarctic meteorology and climatology (p. 425)

Li, X., Cai, W., Meehl, G. A., Chen, D., Yuan, X., Raphael, M., ... & Song, C. (2021). Tropical teleconnection impacts on Antarctic climate changes. Nature Reviews Earth & Environment, 2(10), 680-698.

Ligtenberg, S. R. M., Helsen, M. M., & Van den Broeke, M. R. (2011). An improved semi-empirical model for the densification of Antarctic firn. The Cryosphere, 5(4), 809-819. https://doi.org/10.5194/tc-5-809-2011

Lu, H., Orr, A., King, J. C., Phillips, T., Gilbert, E., Colwell, S., Bracegirdle, T. (2023). Extreme warm events in the South Orkney Islands, Southern Ocean: Compounding influence of atmospheric rivers and föhn conditions. Quarterly Journal of the Royal Meteorological Society, 149(757), 3645-3668, https://doi.org/10.1002/qj.4578

Marshall, G. J. (2003). Trends in the Southern Annular Mode from observations and reanalyses. Journal of climate, 16(24), 4134-4143. https://doi.org/10.1175/1520-0442(2003)016<4134:TITSAM>2.0.CO;2

Marshall, G. J. (2007). Half-century seasonal relationships between the Southern Annular mode and Antarctic temperatures. International Journal of Climatology, 27(3), 373–383. https://doi.org/10.1002/joc.1407

Molina, C., Navarro, F. J., Calvet, J., García-Sellés, D., & Lapazaran, J. J. (2007). Hurd Peninsula glaciers, Livingston Island, Antarctica, as indicators of regional warming: ice-volume changes during the period 1956–2000. Annals of Glaciology, 46, 43-49. https://doi.org/10.3189/172756407782871765

Mölg, T., Maussion, F., Yang, W., & Scherer, D. (2012). The footprint of Asian monsoon dynamics in the mass and energy balance of a Tibetan glacier. The Cryosphere, 6(6), 1445-1461. https://doi.org/10.5194/tc-6-1445-2012

Navarro, F. J., Jonsell, U. Y., Corcuera, M. I., & Martín-Español, A. (2013). Decelerated mass loss of Hurd and Johnsons Glaciers, Livingston Island, Antarctic Peninsula. Journal of Glaciology, 59(213), 115-128. https://doi.org/10.3189/2013JoG12J144

Navarro, F., Recio-Blitz, C., Rodríguez-Cielos, R., Otero, J., Shahateet, K., De Andrés, E., ... & Muñoz-Hermosilla, J. M. (2023). Surface mass balance monitoring of the peripheral glaciers of the Antarctic Peninsula in the context of regional climate change. Annals of Glaciology, 1-6. https://doi.org/10.1017/aog.2023.18

Nicolas, J. P., Vogelmann, A. M., Scott, R. C., Wilson, A. B., Cadeddu, M. P., Bromwich, D. H., ... & Wille, J. D. (2017). January 2016 extensive summer melt in West Antarctica favoured by strong El Niño. Nature communications, 8(1), 15799.

Oliva, M., Navarro, F., Hrbáček, F., Hernandéz, A., Nývlt, D., Pereira, P., ... & Trigo, R. (2017). Recent regional climate cooling on the Antarctic Peninsula and associated impacts on the cryosphere. Science of the Total Environment, 580, 210-223. https://doi.org/10.1016/j.scitotenv.2016.12.030

Osmanoğlu, B., Braun, M., Hock, R., & Navarro, F. J. (2013). Surface velocity and ice discharge of the ice cap on King George Island, Antarctica. Annals of Glaciology, 54(63), 111-119. https://doi.org/10.3189/2013AoG63A517

Pętlicki, M., Sziło, J., MacDonell, S., Vivero, S., & Bialik, R. J. (2017). Recent deceleration of the ice elevation change of Ecology Glacier (King George Island, Antarctica). Remote Sensing, 9(6), 520. https://doi.org/10.3390/rs9060520

Pudełko, R., Angiel, P. J., Potocki, M., Jędrejek, A., & Kozak, M. (2018). Fluctuation of glacial retreat rates in the eastern part of Warszawa Icefield, King George Island, Antarctica, 1979–2018. Remote Sensing, 10(6), 892. https://doi.org/10.3390/rs10060892

Raphael, M. N., Marshall, G. J., Turner, J., Fogt, R. L., Schneider, D., Dixon, D. A., ... & Hobbs, W. R. (2016). The Amundsen sea low: Variability, change, and impact on Antarctic climate, B. Am. Meteorol. Soc., 97, 111–121.

Rignot, E., Mouginot, J., Scheuchl, B., Van Den Broeke, M., Van Wessem, M. J., & Morlighem, M. (2019). Four decades of Antarctic Ice Sheet mass balance from 1979–2017. Proceedings of the National Academy of Sciences, 116(4), 1095-1103.

Rückamp, M., Blindow, N., Suckro, S., Braun, M., & Humbert, A. (2010). Dynamics of the ice cap on King George Island, Antarctica: field measurements and numerical simulations. Annals of Glaciology, 51(55), 80-90. https://doi.org/10.3189/172756410791392817

Rückamp, M., Braun, M., Suckro, S., & Blindow, N. (2011). Observed glacial changes on the King George Island ice cap, Antarctica, in the last decade. Global and Planetary Change, 79(1-2), 99-109. https://doi.org/10.1016/j.gloplacha.2011.06.009

RGI Consortium. (2017). Randolph Glacier Inventory - A Dataset of Global Glacier Outlines, Version 6 [Data Set]. Boulder, Colorado USA. National Snow and Ice Data Center.

Roussel, M. L., Lemonnier, F., Genthon, C., & Krinner, G. (2020). Brief communication: Evaluating Antarctic precipitation in ERA5 and CMIP6 against CloudSat observations. The Cryosphere, 14(8), 2715-2727. https://doi.org/10.5194/tc-14-2715-2020

Rondanelli, R., Hatchett, B., Rutllant, J., Bozkurt, D., & Garreaud, R. (2019). Strongest MJO on record triggers extreme Atacama rainfall and warmth in Antarctica. Geophysical Research Letters, 46(6), 3482-3491. https://doi.org/10.1029/2018GL081475

Sauter, T., Arndt, A., & Schneider, C. (2020). COSIPY v1. 3–an open-source coupled snowpack and ice surface energy and mass balance model. Geoscientific Model Development, 13(11), 5645-5662. https://doi.org/10.5194/gmd-13-5645-2020

Silva, A. B., Arigony-Neto, J., Braun, M. H., Espinoza, J. M. A., Costi, J., & Jaña, R. (2020). Spatial and temporal analysis of changes in the glaciers of the Antarctic Peninsula. Global and Planetary Change, 184, 103079. https://doi.org/10.1016/j.gloplacha.2019.103079

Simões, J. C., Dani, N., Bremer, U. F., Aquino, F. E., & Arigony Neto, J. (2004). Small cirque glaciers retreat on Keller Peninsula, Admiralty Bay, King George Island, Antarctica. https://doi.org/10.31789/pab.v4n1.005

Sobota, I., Kejna, M., & Araźny, A. (2015). Short-term mass changes and retreat of the Ecology and Sphinx glacier system, King George Island, Antarctic Peninsula. Antarctic Science, 27(5), 500-510. https://doi.org/10.1017/S0954102015000188

Scott Yiu, Y., Y., and Maycock, A., C. (2019). On the Seasonality of the El Niño Teleconnection to the Amundsen Sea Region, J. Climate, 32, 4829–4845, https://doi.org/10.1175/JCLI-D-18-0813.1

Shahateet, K., Seehaus, T., Navarro, F., Sommer, C., & Braun, M. (2021). Geodetic mass balance of the South Shetland Islands ice caps, Antarctica, from differencing TanDEM-X DEMs. Remote Sensing, 13(17), 3408. https://doi.org/10.3390/rs13173408

Setzer, A. W., Kayano, M. T., Oliveira, M. R., Ceron, W. L., & Rosa, M. B. (2022). Increase in the number of explosive low–level cyclones around King George Island in the last three decades. Anais da Academia Brasileira de Ciências, 94, e20210633.

Tetzner, D., Thomas, E., & Allen, C. (2019). A validation of ERA5 reanalysis data in the Southern Antarctic Peninsula—Ellsworth land region, and its implications for ice core studies. Geosciences, 9(7), 289. https://doi.org/10.3390/geosciences9070289

Temme, F., Farías-Barahona, D., Seehaus, T., Jaña, R., Arigony-Neto, J., Gonzalez, I., ... & Fürst, J. J. (2023). Strategies for regional modeling of surface mass balance at the Monte Sarmiento Massif, Tierra del Fuego. The Cryosphere, 17(6), 2343-2365.

Torres, C., Bozkurt, D., & Arigony-Neto, J. (2023). Large-scale and regional climatic influences on surface temperature and precipitation in the South Shetland Islands, northern Antarctic Peninsula. Anais da Academia Brasileira de Ciências, 95, e20230685. https://doi.org/10.1590/0001-3765202320230685

Turner, J., Chenoli, S. N., Abu Samah, A., Marshall, G., Phillips, T., & Orr, A. (2009). Strong wind events in the Antarctic. Journal of Geophysical Research: Atmospheres, 114(D18).

Turner, J., Lu, H., White, I., King, J. C., Phillips, T., Hosking, J. S., ... & Deb, P. (2016). Absence of 21st century warming on Antarctic Peninsula consistent with natural variability. Nature, 535(7612), 411-415. https://doi.org/10.1038/nature18645

Turner, J., Marshall, G. J., Clem, K., Colwell, S., Phillips, T., & Lu, H. (2020). Antarctic temperature variability and change from station data. International Journal of Climatology, 40(6), 2986-3007. https://doi.org/10.1002/joc.6378

Turner, J., Lachlan-Cope, T., Colwell, S., & Marshall, G. J. (2005). A positive trend in western Antarctic Peninsula precipitation over the last 50 years reflecting regional and Antarctic-wide atmospheric circulation changes. Annals of Glaciology, 41, 85-91. https://doi.org/10.3189/172756405781813177

Turner, J., Colwell, S. R., & Harangozo, S. (1997). Variability of precipitation over the coastal western Antarctic Peninsula from synoptic observations. Journal of Geophysical Research: Atmospheres, 102(D12), 13999-14007.

Thomas, E. R., Marshall, G. J., & McConnell, J. R. (2008). A doubling in snow accumulation in the western Antarctic Peninsula since 1850. Geophysical research letters, 35(1).

Thompson, D. W., & Solomon, S. (2002). Interpretation of recent Southern Hemisphere climate change. Science, 296(5569), 895-899

Van Wessem, J. M., Ligtenberg, S. R. M., Reijmer, C. H., van de Berg, W. J., van den Broeke, M. R., Barrand, N. E., Thomas, E. R., Turner, J., Wuite, J., Scambos, T. A., and van Meijgaard, E .(2016). The modelled surface mass balance of the Antarctic Peninsula at 5.5 km horizontal resolution. The Cryosphere, 10, 271–285. https://doi.org/10.5194/tc-10-271-2016

Van Wessem, J. M., Van De Berg, W. J., Noël, B. P., Van Meijgaard, E., Amory, C., Birnbaum, G., ... & Van Den Broeke, M. R. (2018). Modelling the climate and surface mass balance of polar ice sheets using RACMO2–Part 2: Antarctica (1979–2016). The Cryosphere, 12(4), 1479-1498.

Vaughan, D. G. (2006). Recent trends in melting conditions on the Antarctic Peninsula and their implications for ice-sheet mass balance and sea level. Arctic, Antarctic, and Alpine Research, 38(1), 147-152. https://www.jstor.org/stable/4095837

Velicogna, I., Sutterley, T. C., & Van Den Broeke, M. R. (2014). Regional acceleration in ice mass loss from Greenland and Antarctica using GRACE time-variable gravity data. Geophysical Research Letters, 41(22), 8130-8137.

Vignon, É., Roussel, M.-L., Gorodetskaya, I., Genthon, C., and Berne, A. (2021). Present and Future of Rainfall in Antarctica, Geophys. Res. Lett., 48, e2020GL092281. https://doi.org/10.1029/2020GL092281

Wallis, B. J., Hogg, A. E., van Wessem, J. M., Davison, B. J., & van den Broeke, M. R. (2023). Widespread seasonal speed-up of west Antarctic Peninsula glaciers from 2014 to 2021. Nature Geoscience, 16(3), 231-237. https://doi.org/10.1038/s41561-023-01131-4

Weidemann, S. S., Sauter, T., Malz, P., Jaña, R., Arigony-Neto, J., Casassa, G., & Schneider, C. (2018). Glacier mass changes of lake-terminating grey and tyndall glaciers at the southern patagonia icefield derived from geodetic observations and energy and mass balance modeling. Frontiers in Earth Science, 6, 81. https://doi.org/10.3389/feart.2018.00081

Wille, J. D., Favier, V., Dufour, A., Gorodetskaya, I. V., Turner, J., Agosta, C., & Codron, F. (2019). West Antarctic surface melt triggered by atmospheric rivers. Nature Geoscience, 12(11), 911-916. https://doi.org/10.1038/s41561-019-0460-1

Wille, J. D., Favier, V., Gorodetskaya, I. V., Agosta, C., Kittel, C., Beeman, J. C., ... & Codron, F. (2021). Antarctic atmospheric river climatology and precipitation impacts. Journal of Geophysical Research: Atmospheres, 126(8), e2020JD033788. https://doi.org/10.1029/2020JD033788

Wille, J. D., Favier, V., Jourdain, N. C., Kittel, C., Turton, J. V., Agosta, C., ... & Berchet, A. (2022). Intense atmospheric rivers can weaken ice shelf stability at the Antarctic Peninsula. Communications Earth & Environment, 3(1), 90. https://doi.org/10.1038/s43247-022-00422-9

Zemp, M., Huss, M., Thibert, E., Eckert, N., McNabb, R., Huber, J., ... & Cogley, J. G. (2019). Global glacier mass changes and their contributions to sea-level rise from 1961 to 2016. Nature, 568(7752), 382-386.

Zou, X., Rowe, P. M., Gorodetskaya, I., Bromwich, D. H., Lazzara, M. A., Cordero, R. R., ... & Bai, L. S. (2022). Strong Warming over the Antarctic Peninsula during Combined Atmospheric River and Foehn Events: Contribution of Shortwave Radiation and Turbulence. Journal of Geophysical Research: Atmospheres, e2022JD038138. https://doi.org/10.1029/2022JD038138

Wang, S., Liu, G., Ding, M., Chen, W., Zhang, W., & Lv, J. (2021). Potential mechanisms governing the variation in rain/snow frequency over the northern Antarctic Peninsula during austral summer. Atmospheric Research, 263, 105811.

Appendices IX

9.1 Supplementary information of the manuscript 2

Supplementary information

New insights on the interannual surface mass balance variability on the South Shetland Islands glaciers, northern Antarctic Peninsula

Christian Torres[1,2]; Deniz Bozkurt[2,3,4]; Tomás Carrasco-Escaff[3], Jordi Bolibar[5]; Jorge Arigony-Neto[1]

[1]Institute of Oceanography, Federal University of Rio Grande, Brazil
[2]Department of Meteorology, University of Valparaíso, Chile
[3]Center for Climate and Resilience Research, Chile
[4]Center for Oceanographic Research COPAS COASTAL, Universidad de Concepción, Chile
[5]Department of Civil Engineering and Geosciences, Delft University of Technology, Netherlands

1 Equation

Barometric equation used in this study:

$$PSFC = P0\left(1 - \frac{a}{T0}h\right)^{\frac{Mg}{aR}} \tag{S1}$$

where $P0$ is atmospheric pressure at reference height, a is thermal gradient, $T0$ is air temperature at reference height, h is height difference, M is average molar mass of air (0.02897 kg/mol), g is gravitational acceleration (9.80665 m/s^2) and R is gas constant (8.314462 kg m^2 / s^2 mol K).

Logarithmic wind profile equation used in this study:

$$WS_2 = WS_{10}\frac{\ln\frac{2}{z_0}}{\ln\frac{10}{z_0}} \tag{S2}$$

where z_0 is surface roughness and WS_{10} is wind speed at 10 m obtained from ERA5. We used a value of 2.12 mm for z_0, which is the mean between the upper and lower boundary condition (firn: 4 mm [Brock et al., 2006] and fresh snow: 0.24 mm [Gromke et al., 2011]) in the surface roughness parametrizations of COSIPY.

2 Tables

Table S1. List of climatological stations considered in the study.

Station	Operation nation	Available data	Latitude	Longitude	Elevation (m)
AWS-FPG	Argentina	2010-2015	62.24° S	58.61° W	195
AWS-KKS	Korea	1996-2020	62.23° S	58.77° W	11
Bellingshausen	Russian Federation	1969-2020	62.20° S	58.97° W	16
Ferraz	Brazil	1986-2005	62.10° S	58.40° W	20
Carlini	Argentina	1986-2020	62.24° S	58.67° W	4
Arturo Prat	Chile	1966-2020	62.50° S	59.70° W	5

Table S2. List of key parameters and the range of values tested in PPD and COSIPY model sensibility.

Model	Parameter/ Method	Value range (min-max)	Units	Optimal setting/ Method	References
PDD	DDFice	3.0-10.0	mm/d°C	7.00	Assumption
	DDFsnow	3.0-7.0	mm/d°C	6.00	Assumption
COSIPY	Densification	-	-	Boone	Boone (2002)
	Roughness	-	-	Moelg12	Mölg et al. (2012)
	Stability correction	-	-	Monin-Obukhov	Default
	Initial snow layer	-	m	0.10	Default
	Initial top density snowpack	-	kg/m^3	300	Default
	Initial bottom density snowpack	-	kg/m^3	600	Default
	Initial temperature bottom	-	°K	268.16	Default
	Ice density	-	kg/m^3	917	Default
	Albedo fresh snow	0.80-0.95	-	0.85	Oerlemans and Knap (1998)
	Albedo firn	0.55-0.80	-	0.68	Oerlemans and Knap (1998)
	Albedo ice	0.30-0.55	-	0.30	Oerlemans and Knap (1998)
	Albedo time scaling factor	1-50	d	22.00	Oerlemans and Knap (1998)
	Albedo depth scaling factor	1-30	cm	3.00	Oerlemans and Knap (1998)
	Roughness length fresh snow	0.24-0.5	mm	0.24	Mölg et al. (2012)
	Roughness length firn	0.7-2.7	mm	1.70	Mölg et al. (2012)
	Roughness length ice	2.4-5.0	mm	4.00	Mölg et al. (2012)

Table S3. Correlation coefficient, Bias and RMSE between SMB observed and modeled for calibration (2002-2011), validation (2012-2019) and comparison (2002-2019) periods.

		Calibration period (2002-2011)			Validation period (2012-2019)			Comparison period (2002-2019)		
		PDD	COSIPY	RACMO	PDD	COSIPY	RACMO	PDD	COSIPY	RACMO
Annual	r	0.83	0.77	0.91	0.82	0.83	0.87	0.82	0.80	0.89
	Bias	144.00	130.00	124.00	21.00	-43.00	-41.00	89.00	53.00	51.00
	RMSE	295.00	245.00	186.00	221.00	194.00	190.00	264.00	224.00	188.00
Winter	r	0.77	0.65	0.78	0.67	0.71	0.68	0.70	0.65	0.67
	Bias	-101.00	-212.00	-196.00	-63.00	-177.00	-151.00	-84.00	-196.00	-176.00
	RMSE	143.00	245.00	220.00	139.00	213.00	222.00	141.00	231.00	221.00
Summer	r	0.84	0.72	0.97	0.86	0.82	0.84	0.80	0.72	0.85
	Bias	245.00	343.00	321.00	84.00	134.00	110.00	174.00	250.00	227.00
	RMSE	329.00	386.00	329.00	223.00	185.00	162.00	286.00	313.00	268.00

Table S4. Mean, standard deviation (SD), minimum (Min) and maximum (Max) of the SMB observed and modeled (PDD, COSIPY and RACMO) for calibration (2002-2011), validation (2012-2019) and comparison (2002-2019) periods.

		Calibration period (2002-2011)				Validation period (2012-2019)				Comparison period (2002-2019)			
		OBS	PDD	COSIPY	RACMO	OBS	PDD	COSIPY	RACMO	OBS	PDD	COSIPY	RACMO
Annual	mean	-90.0	54.0	41.0	34.0	202.0	223.0	158.0	161.0	40.0	129.0	93.0	91.0
	std	343.0	480.0	287.0	281.0	359.0	415.0	263.0	220.0	371.0	448.0	275.0	257.0
	min	-595.0	-1046.0	-448.0	-502.0	-320.0	-517.0	-299.0	-255.0	-595.0	-1046.0	-448.0	-502.0
	max	475.0	852.0	686.0	432.0	655.0	594.0	435.0	424.0	655.0	852.0	686.0	432.0
Winter	mean	684.0	583.0	472.0	488.0	714.0	651.0	537.0	564.0	698.0	613.0	501.0	522.0
	std	162.0	150.0	142.0	98.0	175.0	89.0	95.0	30.0	163.0	128.0	125.0	83.0
	min	395.0	354.0	306.0	375.0	430.0	537.0	421.0	523.0	395.0	354.0	306.0	375.0
	max	1024.0	796.0	702.0	675.0	1020.0	790.0	698.0	602.0	1024.0	796.0	702.0	675.0
Summer	mean	-774.0	-530.0	-432.0	-453.0	-513.0	-428.0	-379.0	-403.0	-658.0	-485.0	-408.0	-431.0
	std	268.0	404.0	217.0	221.0	226.0	381.0	233.0	228.0	277.0	386.0	219.0	219.0
	min	-1300.0	-1534.0	-861.0	-914.0	-825.0	-1054.0	-720.0	-850.0	-1300.0	-1534.0	-861.0	-914.0
	max	-285.0	55.0	-17.0	-84.0	-215.0	7.0	-62.0	-126.0	-215.0	55.0	-17.0	-84.0

Table S5. Annual and seasonal correlation analysis of surface mass balance modeled using PDD, COSIPY and RACMO models. Significance difference ($p<0.05$) using t-student test is indicated by an asterisk.

		GLAS_PDD	GLAS_COSIPY	GLAS_RACMO	SSI_RACMO
Annual	GLAS_PDD	-	0.95	0.83	0.83
	GLAS_COSIPY	-	-	0.84	0.84
	GLAS_RACMO	-	-	-	0.96*
	SSI_RACMO	-	-	-	-
Winter	GLAS_PDD	-	0.96	0.7*	0.78
	GLAS_COSIPY	-	-	0.66*	0.76
	GLAS_RACMO	-	-	-	0.86*
	SSI_RACMO	-	-	-	-
Summer	GLAS_PDD	-	0.96	0.85	0.85
	GLAS_COSIPY	-	-	0.87	0.87
	GLAS_RACMO	-	-	-	0.98
	SSI_RACMO	-	-	-	-

Table S6. Mean, standard deviation (SD), minimum (Min) and maximum (Max) values of the annual (April to March), winter (April to November) and summer (December to March) time series of the spatially averaged SMB from 1980 to 2019.

		SMB	Accumulation	Ablation	Snowfall	Temperature	Insolation
Mean	Annual	109.0	1048.0	707.0	681.0	-1.77	130.0
	Winter	486.0	703.0	51.0	524.0	-2.98	84.0
	Summer	-377.0	345.0	656.0	157.0	0.66	221.0
SD	Annual	321.0	103.0	301.0	84.0	0.77	2.0
	Winter	77.0	91.0	34.0	68.0	1.09	2.0
	Summer	300.0	43.0	294.0	41.0	0.38	7.0
Min	Annual	-688.0	842.0	152.0	500.0	-3.67	125.0
	Winter	331.0	514.0	9.0	391.0	-5.78	79.0
	Summer	-1140.0	275.0	134.0	92.0	-0.22	209.0
Max	Annual	747.0	1306.0	1432.0	848.0	-0.27	136.0
	Winter	628.0	878.0	157.0	677.0	-0.97	88.0
	Summer	168.0	449.0	1376.0	240.0	1.39	240.0

Table S7. Correlation between pairs of annual (April to March), winter (April to November) and summer (December to March) time series of the spatially averaged SMB from 1980 to 2019. Significance is indicated by an asterisk, where * ($p<0.10$) and ** ($p<0.05$).

		SMB	Accumulation	Ablation	Snowfall	Temperature	Insolation
Annual	SMB	1.0**	0.4**	-0.95**	0.72**	-0.09	0.42**
	Accumulation	0.4**	1.0**	-0.13	0.81**	0.32**	-0.11
	Ablation	-0.95**	-0.13	1.0**	-0.53**	0.2	-0.48**
	Snowfall	0.72**	0.81**	-0.53**	1.0**	0.13	0.01
	Temperature	-0.09	0.32**	0.2	0.13	1.0**	-0.19
	Insolation	0.42**	-0.11	-0.48**	0.01	-0.19	1.0**
Winter	SMB	1.0**	0.89**	-0.33**	0.88**	0.1	-0.3*
	Accumulation	0.89**	1.0**	0.07	0.92**	0.33**	-0.4**
	Ablation	-0.33**	0.07	1.0**	-0.13	0.53**	-0.24
	Snowfall	0.88**	0.92**	-0.13	1.0**	0.2	-0.33**
	Temperature	0.1	0.33**	0.53**	0.2	1.0**	-0.28*
	Insolation	-0.3*	-0.4**	-0.24	-0.33**	-0.28*	1.0**
Summer	SMB	1.0**	0.26	-0.99**	0.76**	-0.85**	0.32**
	Accumulation	0.26	1.0**	-0.14	0.68**	-0.12	-0.38**
	Ablation	-0.99**	-0.14	1.0**	-0.68**	0.84**	-0.37**
	Snowfall	0.76**	0.68**	-0.68**	1.0**	-0.62**	-0.01
	Temperature	-0.85**	-0.12	0.84**	-0.62**	1.0**	-0.32**
	Insolation	0.32**	-0.38**	-0.37**	-0.01	-0.32**	1.0**

Table S8. Sensitivity of the surface energy (SEB) and mass (SMB) balance components using the COSIPY model when an offset (ΔT) to temperature and weighting snowfall by a factor (P0). We used five configurations with neutral (no changes in temperature and snowfall), cold (-1 °C air temperature), warm (+1 °C air temperature), dry (-20% snowfall) and wet (+20% snowfall) conditions.

		Normal	Cold	Warm	Dry	Wet
SEB (W/m^2)	QME	2.72	0.67	7.09	2.68	2.75
	QSWin	101.79	101.79	101.79	101.79	101.79
	ALBEDO	0.88	0.88	0.88	0.88	0.88
	QLWin	267.88	267.88	267.88	267.88	267.88
	QLWout	-292.28	-288.88	-295.48	-292.30	-292.27
	QH	22.65	19.25	26.96	22.65	22.66
	QLE	-6.32	-8.34	-3.34	-6.27	-6.36
	QG	-0.61	-0.56	-0.48	-0.67	-0.54
SMB (mm w.e.)	SMB	434.21	610.56	39.88	284.28	584.67
	SNOWFALL	767.08	767.08	767.08	613.66	920.49
	SURFACE MELTING	252.49	61.59	661.30	249.26	255.61
	SUBLIMATION	-94.14	-105.42	-84.23	-94.07	-94.20
	DEPOSITION	19.09	12.61	28.19	19.54	18.80
	EVAPORATION	-1.27	-0.97	-1.64	-1.20	-1.31
	SUBSURFACE MELTING	5.91	2.20	12.01	5.55	6.31
	REFREEZE	1.85	1.05	3.79	1.15	2.82

Table S9. The same as in Table 1 but applying an exponential filter.

	Annual correlation			Winter correlation			Summer correlation		
	SMB	TEMP	SNOWFALL	SMB	TEMP	SNOWFALL	SMB	TEMP	SNOWFALL
NIÑO 3	0.06	-0.16	-0.05	-0.17	-0.13	-0.1	0.14	-0.26	0.05
NIÑO 3.4	0.01	-0.25	-0.07	-0.19	-0.25	-0.17	0.11	-0.27*	0.0
NIÑO 4	-0.05	-0.3*	-0.11	-0.18	-0.3*	-0.21	0.1	-0.29*	-0.04
DC-CPAC	-0.45**	-0.3*	-0.38**	-0.16	-0.28*	-0.21	-0.23	-0.04	-0.36**
SAM	-0.06	0.44**	0.08	0.04	0.47**	0.14	-0.4**	0.41**	-0.45**
ASL	-0.08	-0.55**	-0.13	-0.23	-0.61**	-0.22	0.22	-0.32**	0.18
SST-ABSea	-0.26	0.19	-0.22	-0.19	0.3*	-0.18	-0.46**	0.26	-0.22
SST-WSea	-0.26	0.64**	-0.2	-0.04	0.59**	-0.0	-0.39**	0.54**	0.0
Z500-Drake	-0.53**	0.39**	-0.63**	-0.66**	0.46**	-0.66**	-0.46**	0.23	-0.45**
SST-Drake	-0.42**	0.58**	-0.3*	-0.18	0.62**	-0.09	-0.59**	0.44**	-0.17

Table S10. The same as in Table 2 but applying an exponential filter.

	Annual	Winter correlation	Summer correlation	MAM	JJA	SON	DJF
SMB	-0.07	0.52**	-0.34**	-0.32**	0.67**	0.18	-0.41**
TEMP	0.5**	0.56**	0.63**	0.78**	0.69**	0.65**	0.33**
SNOWFALL	0.24	0.52**	-0.34**	0.02	0.6**	0.22	-0.07

Table S11. Extreme SMB, Snowfall, Temperature at 2 m (T2), Rainfall and Sensible Heat Flux (QH) days events associated with ARs from 1980 to 2019.

Time	SMB mm w.e./day	T2 °C	SNOWFALL mm/day	RAINFALL mm/day	QH W/m²
1988-06-04	17.0	-8.23	18.0	0.0	0.0
1988-06-11	20.0	-3.38	20.0	0.0	6.0
1988-06-26	30.0	-2.67	31.0	0.0	14.0
1988-09-24	16.0	-1.76	16.0	0.0	8.0
1997-05-02	17.0	-1.96	17.0	0.0	22.0
1997-06-21	22.0	-5.92	22.0	0.0	-6.0
1997-10-08	16.0	-5.98	17.0	0.0	12.0
1998-03-04	15.0	-0.20	15.0	0.0	14.0
2002-02-05	-26.0	2.32	0.0	2.0	71.0
2002-02-08	-26.0	2.46	3.0	11.0	59.0
2002-02-11	-25.0	2.58	0.0	5.0	77.0
2002-02-25	-33.0	2.83	0.0	4.0	66.0
2006-01-22	-32.0	3.79	0.0	0.0	77.0
2006-01-23	-34.0	3.57	0.0	0.0	84.0
2006-02-07	-32.0	3.25	0.0	3.0	64.0
2006-03-16	-31.0	3.22	0.0	7.0	71.0
2009-06-17	15.0	-0.51	15.0	0.0	27.0
2009-07-15	19.0	-3.75	19.0	0.0	15.0
2009-09-24	16.0	-4.11	16.0	0.0	11.0
2009-11-30	20.0	-1.65	20.0	0.0	14.0

Table S12. Sensitivity of the modeled SMB to the main COSIPY model parameters. X and S are the mean value and standard deviation (measured in mm w.e.) of the annual SMB time series obtained from each experiment, respectively. X0 and S0 correspond to the same statistics but for the control time series. r represents the correlation between the annual SMB time series obtained from each experiment and the control time series.

	Albedo fresh snow					
	Value	X	S	X-X0	S/S0	r
1	0.800000	-192.0	287.0	-240.0	1.15	0.99
2	0.816667	-135.0	280.0	-183.0	1.12	1.00
3	0.833333	-81.0	272.0	-129.0	1.09	1.00
4	0.850000	-32.0	264.0	-80.0	1.06	1.00
5	0.866667	14.0	257.0	-34.0	1.02	1.00
6	0.883333	56.0	249.0	8.0	0.99	1.00
7	0.900000	95.0	242.0	47.0	0.97	1.00
8	0.916667	130.0	236.0	82.0	0.94	1.00
9	0.933333	162.0	229.0	114.0	0.92	1.00
10	0.950000	191.0	224.0	143.0	0.89	1.00

	Albedo firn					
	Value	X	S	X-X0	S/S0	r
1	0.550000	43.0	253.0	-5.0	1.01	1.0
2	0.577778	44.0	252.0	-4.0	1.01	1.0
3	0.605556	46.0	252.0	-2.0	1.00	1.0
4	0.633333	47.0	251.0	-1.0	1.00	1.0
5	0.661111	49.0	250.0	1.0	1.00	1.0
6	0.688889	50.0	250.0	2.0	1.00	1.0
7	0.716667	51.0	249.0	3.0	0.99	1.0
8	0.744444	53.0	248.0	5.0	0.99	1.0
9	0.772222	54.0	248.0	6.0	0.99	1.0
10	0.800000	56.0	247.0	8.0	0.99	1.0

	Albedo ice					
	Value	X	S	X-X0	S/S0	r
1	0.300000	48.0	250.0	0.0	1.0	1.0
2	0.327778	48.0	250.0	0.0	1.0	1.0
3	0.355556	48.0	250.0	0.0	1.0	1.0
4	0.383333	48.0	250.0	0.0	1.0	1.0
5	0.411111	48.0	250.0	0.0	1.0	1.0
6	0.438889	48.0	250.0	0.0	1.0	1.0
7	0.466667	48.0	250.0	0.0	1.0	1.0
8	0.494444	48.0	250.0	0.0	1.0	1.0
9	0.522222	48.0	250.0	0.0	1.0	1.0
10	0.550000	48.0	250.0	0.0	1.0	1.0

	Albedo time scaling factor					
	Value	X	S	X-X0	S/S0	r
1	1.000000	-61.0	294.0	-109.0	1.17	0.98
2	6.444444	24.0	261.0	-24.0	1.04	1.00
3	11.888889	39.0	255.0	-9.0	1.02	1.00
4	17.333333	45.0	252.0	-3.0	1.01	1.00
5	22.777778	48.0	250.0	0.0	1.00	1.00
6	28.222222	51.0	249.0	3.0	1.00	1.00
7	33.666667	52.0	249.0	4.0	0.99	1.00
8	39.111111	53.0	248.0	5.0	0.99	1.00
9	44.555556	54.0	248.0	6.0	0.99	1.00
10	50.000000	54.0	248.0	6.0	0.99	1.00

	Albedo depth scaling factor					
	Value	X	S	X-X0	S/S0	r
1	1.000000	48.0	250.0	0.0	1.0	1.0
2	4.222222	48.0	250.0	0.0	1.0	1.0
3	7.444444	48.0	250.0	0.0	1.0	1.0
4	10.666667	48.0	250.0	0.0	1.0	1.0
5	13.888889	48.0	250.0	0.0	1.0	1.0
6	17.111111	48.0	250.0	0.0	1.0	1.0
7	20.333333	48.0	250.0	0.0	1.0	1.0
8	23.555556	48.0	250.0	0.0	1.0	1.0
9	26.777778	48.0	250.0	0.0	1.0	1.0
10	30.000000	48.0	250.0	0.0	1.0	1.0

	Roughness length fresh snow					
	Value	X	S	X-X0	S/S0	r
1	0.240000	48.0	250.0	0.0	1.00	1.0
2	0.268889	32.0	254.0	-16.0	1.02	1.0
3	0.297778	18.0	258.0	-30.0	1.03	1.0
4	0.326667	4.0	262.0	-44.0	1.04	1.0
5	0.355556	-9.0	265.0	-57.0	1.06	1.0
6	0.384444	-21.0	268.0	-69.0	1.07	1.0
7	0.413333	-32.0	271.0	-80.0	1.08	1.0
8	0.442222	-44.0	274.0	-92.0	1.09	1.0
9	0.471111	-54.0	276.0	-102.0	1.10	1.0
10	0.500000	-65.0	279.0	-113.0	1.11	1.0

	Roughness length firn					
	Value	X	S	X-X0	S/S0	r
1	0.700000	48.0	250.0	-0.0	1.0	1.0
2	0.922222	48.0	250.0	0.0	1.0	1.0
3	1.144444	48.0	250.0	0.0	1.0	1.0
4	1.366667	48.0	250.0	0.0	1.0	1.0
5	1.588889	48.0	250.0	0.0	1.0	1.0
6	1.811111	48.0	250.0	0.0	1.0	1.0
7	2.033333	48.0	250.0	0.0	1.0	1.0
8	2.255556	48.0	250.0	0.0	1.0	1.0
9	2.477778	48.0	250.0	0.0	1.0	1.0
10	2.700000	48.0	250.0	0.0	1.0	1.0

	Roughness length ice					
	Value	X	S	X-X0	S/S0	r
1	2.400000	48.0	250.0	0.0	1.0	1.0
2	2.688889	48.0	250.0	0.0	1.0	1.0
3	2.977778	48.0	250.0	0.0	1.0	1.0
4	3.266667	48.0	250.0	0.0	1.0	1.0
5	3.555556	48.0	250.0	0.0	1.0	1.0
6	3.844444	48.0	250.0	0.0	1.0	1.0
7	4.133333	48.0	250.0	0.0	1.0	1.0
8	4.422222	48.0	250.0	0.0	1.0	1.0
9	4.711111	48.0	250.0	0.0	1.0	1.0
10	5.000000	48.0	250.0	0.0	1.0	1.0

Table S13. The same as in Table S12 but for the sensitivity of the modeled SMB to the mean value of the near-surface air temperature and snowfall forcing.

Temperature °K	Snowfall %	X	S	X-X0	S/S0	r
-1.0	0.8	460.0	97.0	412.0	0.39	0.80
-1.0	0.9	536.0	106.0	488.0	0.43	0.77
-1.0	1.0	612.0	116.0	564.0	0.46	0.75
-1.0	1.1	688.0	125.0	639.0	0.50	0.74
-1.0	1.2	763.0	135.0	715.0	0.54	0.72
-0.5	0.8	396.0	120.0	348.0	0.48	0.90
-0.5	0.9	472.0	127.0	424.0	0.51	0.88
-0.5	1.0	547.0	136.0	499.0	0.54	0.86
-0.5	1.1	622.0	144.0	574.0	0.58	0.85
-0.5	1.2	698.0	153.0	650.0	0.61	0.83
0.0	0.8	289.0	151.0	241.0	0.60	0.96
0.0	0.9	363.0	157.0	315.0	0.63	0.95
0.0	1.0	438.0	164.0	390.0	0.66	0.94
0.0	1.1	513.0	172.0	465.0	0.69	0.93
0.0	1.2	588.0	180.0	540.0	0.72	0.92
0.5	0.8	126.0	191.0	78.0	0.76	0.99
0.5	0.9	201.0	196.0	153.0	0.78	0.99
0.5	1.0	275.0	202.0	227.0	0.81	0.99
0.5	1.1	351.0	208.0	303.0	0.83	0.98
0.5	1.2	426.0	215.0	378.0	0.86	0.97
1.0	0.8	-102.0	243.0	-150.0	0.97	1.00
1.0	0.9	-28.0	247.0	-76.0	0.99	1.00
1.0	1.0	48.0	250.0	0.0	1.00	1.00
1.0	1.1	123.0	255.0	75.0	1.02	1.00
1.0	1.2	197.0	260.0	149.0	1.04	1.00

Table S14. The same as in Table S12 but for the sensitivity of the modeled SMB to the interannual variability of the meteorological input. R^2 corresponds to the squared correlation.

		X	S	X-X0	S/S0	r	R^2
Temp	Annual	457.0	107.0	409.0	0.43	0.77	59.0
	Winter	551.0	79.0	73.0	0.84	0.87	76.0
	Summer	-94.0	79.0	336.0	0.34	0.84	71.0
Snowfall	Annual	59.0	207.0	11.0	0.83	0.91	84.0
	Winter	471.0	58.0	-7.0	0.61	0.49	24.0
	Summer	-412.0	189.0	18.0	0.82	0.98	97.0
Insolation	Annual	-39.0	259.0	-87.0	1.03	1.00	99.0
	Winter	462.0	97.0	-16.0	1.03	1.00	99.0
	Summer	-500.0	236.0	-71.0	1.02	1.00	99.0

Table S15. Annual and seasonal correlation analysis of surface mass balance (SMB) observed at Johnsons, Hurd and Bellingshausen glaciers.

		JOHNSONS	HURD	BELLINGSHAUSEN
Annual	JOHNSONS	1.00	0.91	0.74
	HURD	0.91	1.00	1.00
	BELLINGSHAUSEN	0.74	1.00	1.00
Winter	JOHNSONS	1.00	0.86	0.90
	HURD	0.86	1.00	0.71
	BELLINGSHAUSEN	0.90	0.71	1.00
Summer	JOHNSONS	1.00	0.90	0.46
	HURD	0.90	1.00	0.94
	BELLINGSHAUSEN	0.46	0.94	1.00

Table S16. Similar to Table 1 but for surface mass balance (SMB) from observed (OBS) and modeled (RACMO and COSIPY) for the period 2002-2019. Significance is indicated by an asterisk, where * (p<0.10) and ** (p<0.05).

	Annual correlation			Winter correlation			Summer correlation		
	OBS	RACMO	COSIPY	OBS	RACMO	COSIPY	OBS	RACMO	COSIPY
NIÑO 3	0.28	0.21	0.31	0.11	-0.32	-0.05	0.37	0.49**	0.5**
NIÑO 3.4	0.24	0.19	0.25	0.12	-0.26	-0.03	0.5**	0.55**	0.51**
NIÑO 4	0.28	0.25	0.22	0.08	-0.26	-0.1	0.58**	0.6**	0.48**
DC-CPAC	-0.01	0.01	-0.06	-0.18	0.23	0.11	0.22	0.34	0.38
SAM	0.17	0.12	-0.1	0.05	0.36	-0.06	0.14	0.03	-0.12
ASL	-0.16	-0.17	0.24	-0.06	-0.34	0.12	0.24	0.33	0.49**
SST-ABSea	-0.64**	-0.59**	-0.5**	-0.49**	-0.07	-0.33	-0.55**	-0.55**	-0.31
SST-WSea	-0.64**	-0.47*	-0.64**	-0.39	-0.21	-0.19	-0.5**	-0.53**	-0.55**
Z500-Drake	-0.26	-0.31	-0.41*	-0.23	-0.42*	-0.62**	-0.04	-0.15	-0.46*
SST-Drake	-0.7**	-0.6**	-0.66**	-0.31	-0.14	-0.29	-0.82**	-0.76**	-0.59**

Table S17. The same as in Table S16 but applying an exponential filter.

	Annual correlation			Winter correlation			Summer correlation		
	OBS	RACMO	COSIPY	OBS	RACMO	COSIPY	OBS	RACMO	COSIPY
NIÑO 3	0.04	-0.12	-0.06	-0.12	-0.34	-0.18	0.2	0.04	0.05
NIÑO 3.4	0.08	-0.09	-0.04	-0.19	-0.27	-0.24	0.32	0.12	0.13
NIÑO 4	0.03	-0.14	-0.17	-0.21	-0.25	-0.28	0.44*	0.09	0.1
DC-CPAC	-0.09	-0.07	-0.28	-0.36	-0.07	-0.25	0.03	0.1	0.05
SAM	0.16	0.15	-0.04	0.14	0.51**	0.09	0.19	0.11	0.0
ASL	-0.22	-0.2	0.01	-0.25	-0.53**	-0.17	0.35	0.35	0.55**
SST-ABSea	-0.78**	-0.65**	-0.55**	-0.59**	-0.32	-0.39	-0.72**	-0.6**	-0.6**
SST-WSea	-0.58**	-0.57**	-0.58**	-0.37	-0.1	-0.21	-0.49**	-0.68**	-0.7**
Z500-Drake	-0.58**	-0.66**	-0.8**	-0.5**	-0.5**	-0.71**	-0.15	-0.24	-0.5**
SST-Drake	-0.79**	-0.67**	-0.58**	-0.58**	-0.37	-0.45*	-0.86**	-0.8**	-0.8**

Table S18. Correlation analysis between the annual climate indices used in this study.

	NIÑO 3	NIÑO 3.4	NIÑO 4	DC-CPAC	SAM	ASL	SST-ABSea	SST-WSea	Z500-Drake	SST-Drake
NIÑO 3	-	0.95**	0.86**	-0.03	-0.04	0.41**	-0.26	-0.29*	0.03	-0.28*
NIÑO 3.4	-	-	0.96**	0.08	-0.13	0.49**	-0.32**	-0.37**	0.02	-0.35**
NIÑO 4	-	-	-	0.22	-0.24	0.55**	-0.35**	-0.44**	0.04	-0.41**
DC-CPAC	-	-	-	-	-0.29*	0.27*	0.28*	-0.37**	0.2	-0.12
SAM	-	-	-	-	-	-0.74**	0.01	0.31*	-0.08	0.24
ASL	-	-	-	-	-	-	-0.26	-0.52**	-0.06	-0.44**
SST-ABSea	-	-	-	-	-	-	-	0.47**	0.37**	0.76**
SST-WSea	-	-	-	-	-	-	-	-	0.23	0.7**
Z500-Drake	-	-	-	-	-	-	-	-	-	0.32**
SST-Drake	-	-	-	-	-	-	-	-	-	-

Table S19. The same as in Table S18 but applying an exponential filter.

	NIÑO 3	NIÑO 3.4	NIÑO 4	DC-CPAC	SAM	ASL	SST-ABSea	SST-WSea	Z500-Drake	SST-Drake
NIÑO 3	-	0.9**	0.75**	0.02	0.02	0.37**	-0.18	-0.28*	0.07	-0.18
NIÑO 3.4	-	-	0.94**	0.24	-0.2	0.57**	-0.15	-0.38**	0.1	-0.21
NIÑO 4	-	-	-	0.42**	-0.27*	0.65**	-0.17	-0.48**	0.12	-0.24
DC-CPAC	-	-	-	-	-0.39**	0.47**	0.22	-0.46**	0.26	-0.08
SAM	-	-	-	-	-	-0.59**	-0.12	0.3*	-0.08	0.24
ASL	-	-	-	-	-	-	-0.25	-0.61**	0.04	-0.37**
SST-ABSea	-	-	-	-	-	-	-	0.43**	0.38**	0.74**
SST-WSea	-	-	-	-	-	-	-	-	0.27*	0.67**
Z500-Drake	-	-	-	-	-	-	-	-	-	0.43**
SST-Drake	-	-	-	-	-	-	-	-	-	-

3 Figures

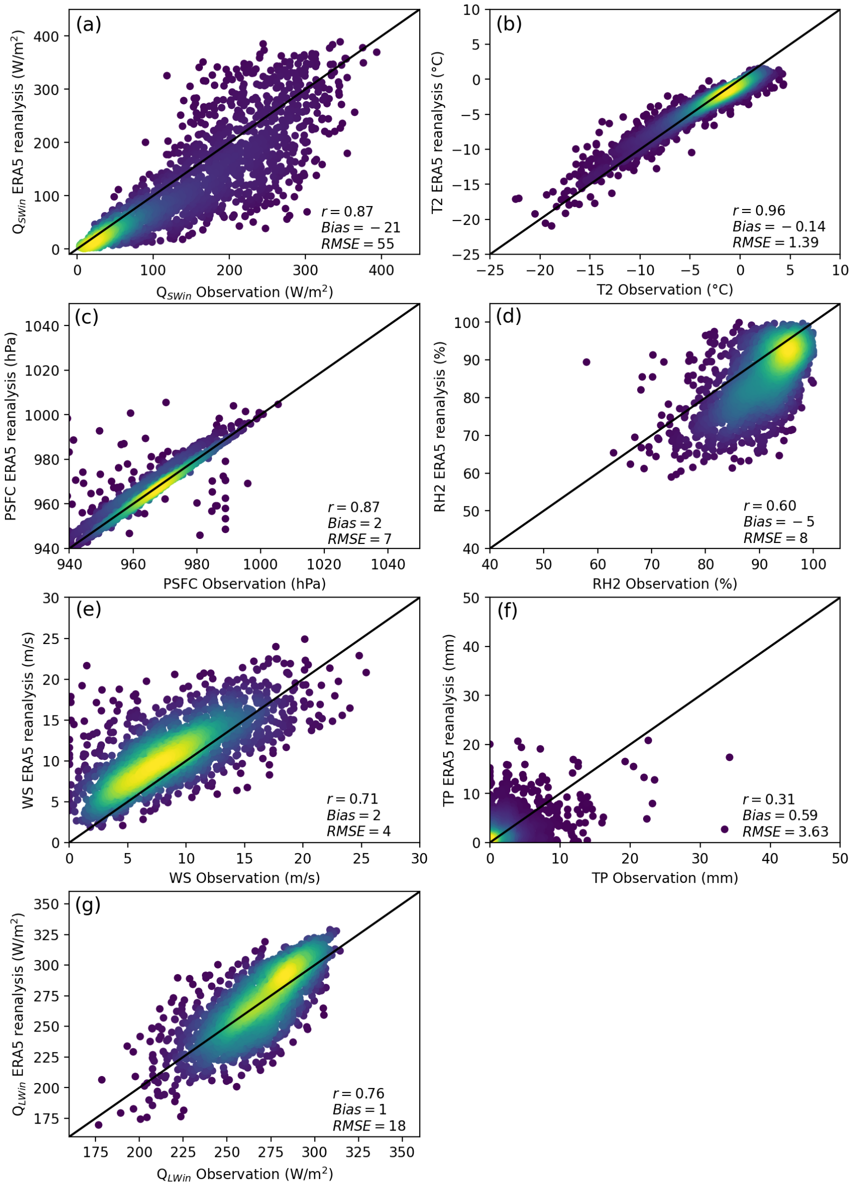

Figure S1. Daily density scatter plot between observations at Fourcade Glacier and ERA5 reanalysis (a) solar radiation, (b) air temperature, (c) surface pressure, (d) relativity humidity, (e) wind speed, (f) total precipitation, and (g) atmospheric longwave radiation from november 2010 to november 2015.

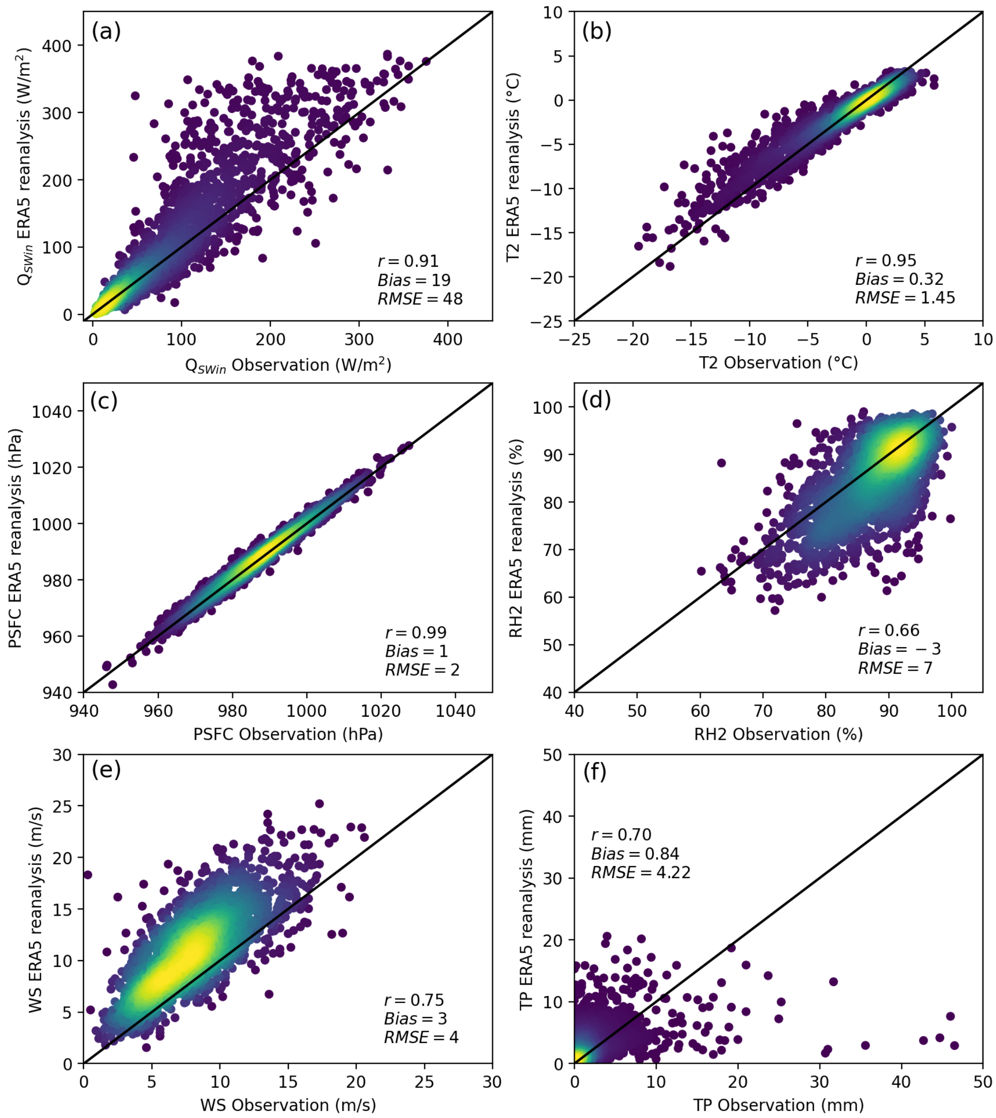

Figure S2. Daily density scatter plot between Korean King Sejong Station climatological observations and ERA5 reanalysis (a) solar radiation, (b) air temperature, (c) surface pressure, (d) relativity humidity, (e) wind speed, and (f) total precipitation from january 1996 to december 2019.

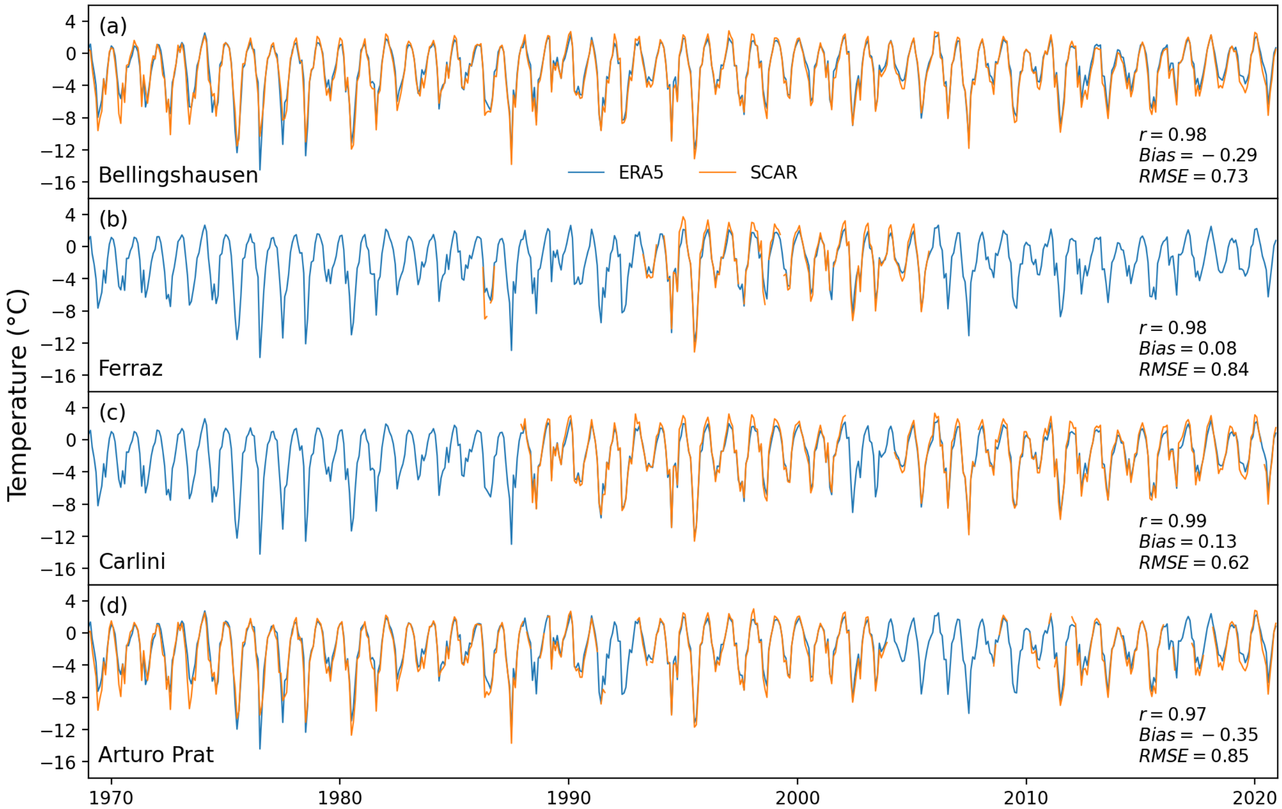

Figure S3. Monthly time series observations (orange line) and ERA5 reanalysis (blue line) of air temperature at 2 m over the last 62 years (1969-2020), (a) Bellingshausen Station, (b) Ferraz Station, (c) Carlini Station, (d) Arturo Prat Station.

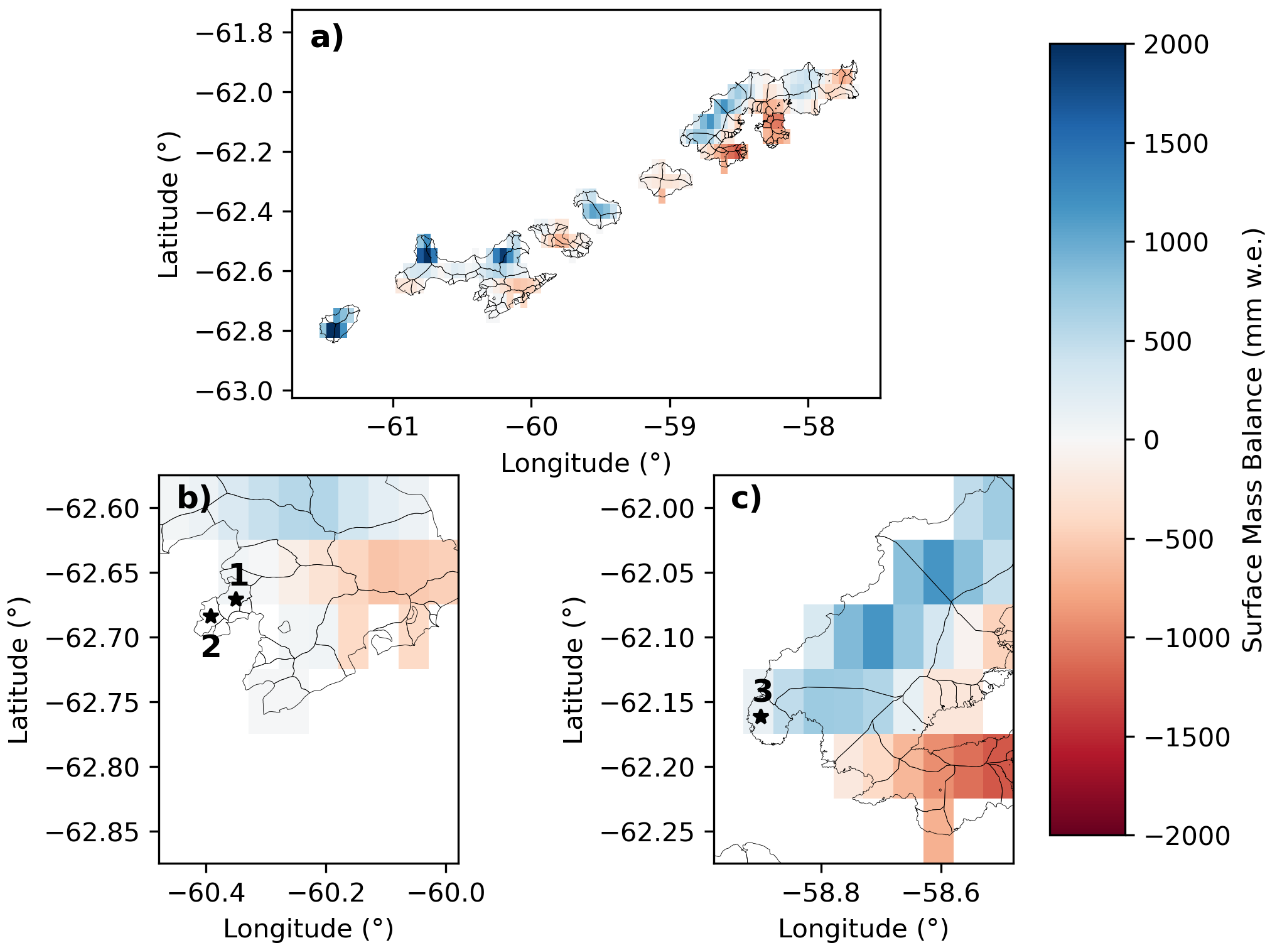

Figure S4. Annual mean surface mass balance over (a) the entire South Shetland Islands glaciers, (b) zoomed for the Johnsons and Hurd glaciers, and (c) zoomed for the Bellingshausen glacier. Surface mass balance was obtained from RACMO 5.5 km for the time period 1980-2019. Black asterisks indicate the centroid of glaciers with in-situ surface mass balance observations (i.e., (1) Johnsons, (2) Hurd, and (3) Bellingshausen Glaciers). The back outlines represent the glacier contours obtained from the Randolph Glacier Inventory, (RGI, 2017).

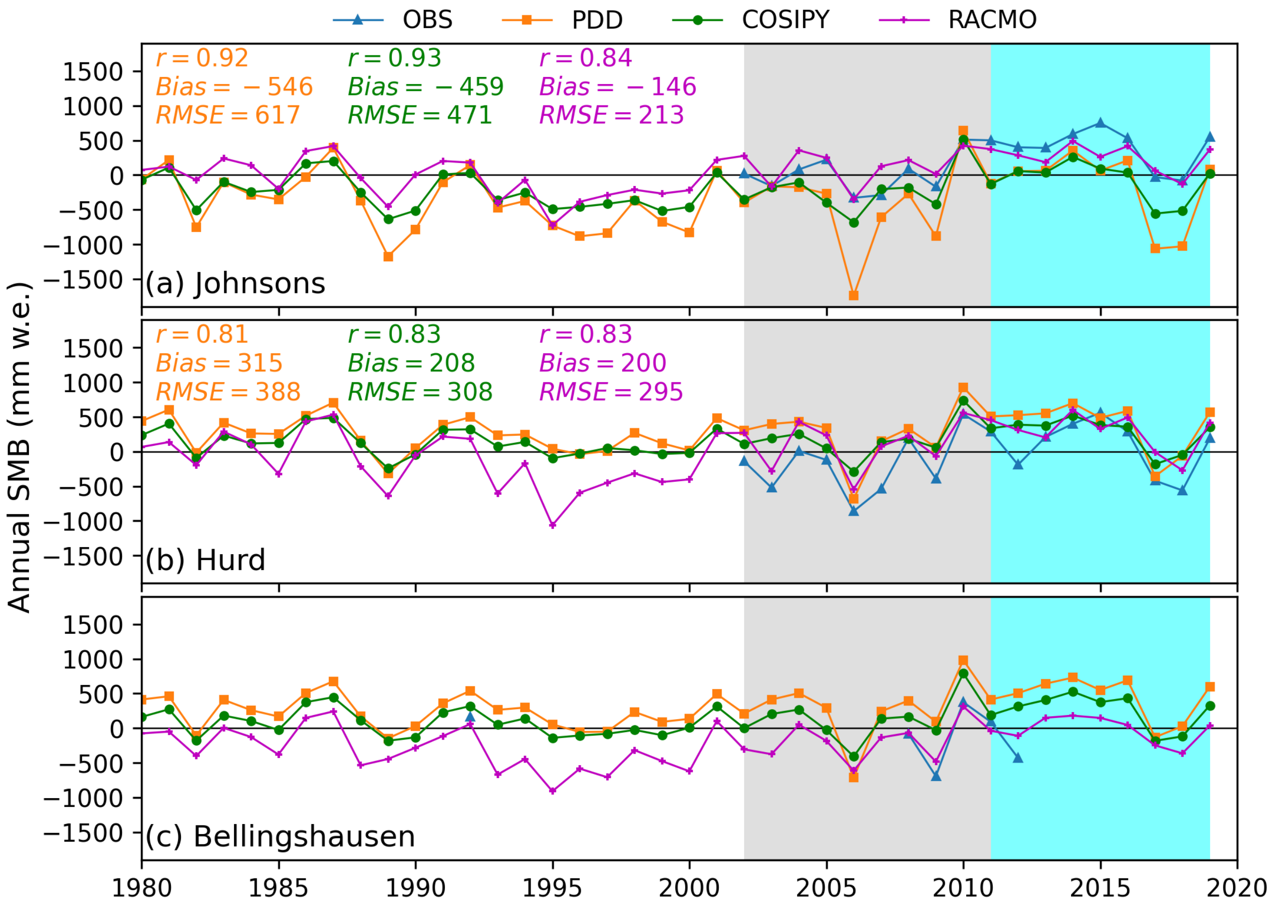

Figure S5. Annual surface mass balance intercomparison between observation and reconstruction from three glaciological models (blue line OBS, and orange line PDD, green line COSIPY and magenta line RACMO models) at (a) Jonhnsons Glacier, (b) Hurd Glacier, and (c) Bellingshausen Glacier. Both PDD and COSIPY models were forced using the global reanalysis ERA5-downscaled. Grey shaded areas indicate the calibration period (2002-2011) and aqua shared areas show validation period (2012-2019). Note all statistical indicators as well correlation coefficient (r), Bias and root mean square error (RMSE) were calculated for the validation period (2012-2019).

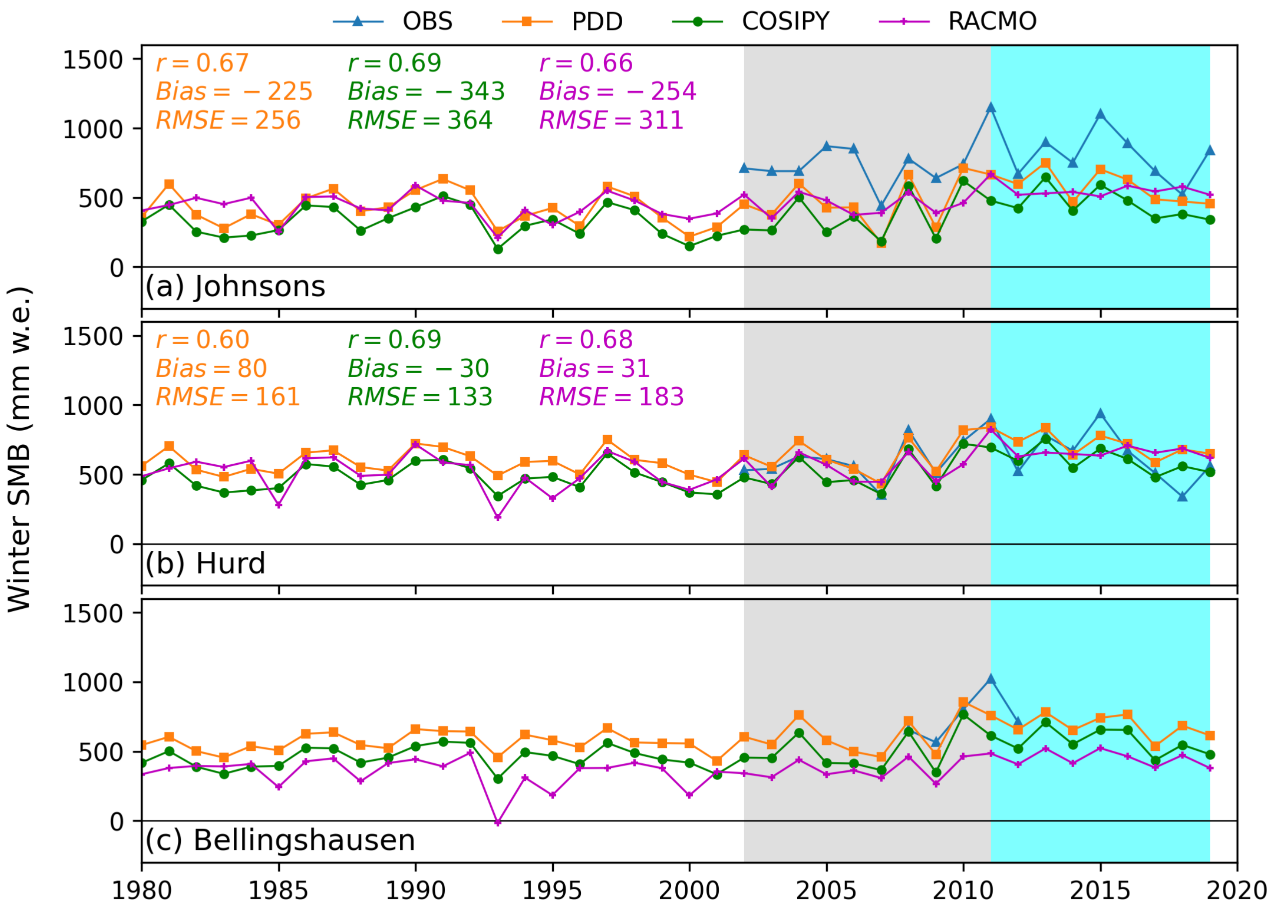

Figure S6. The same as in Fig. S5 but for the winter (April to November).

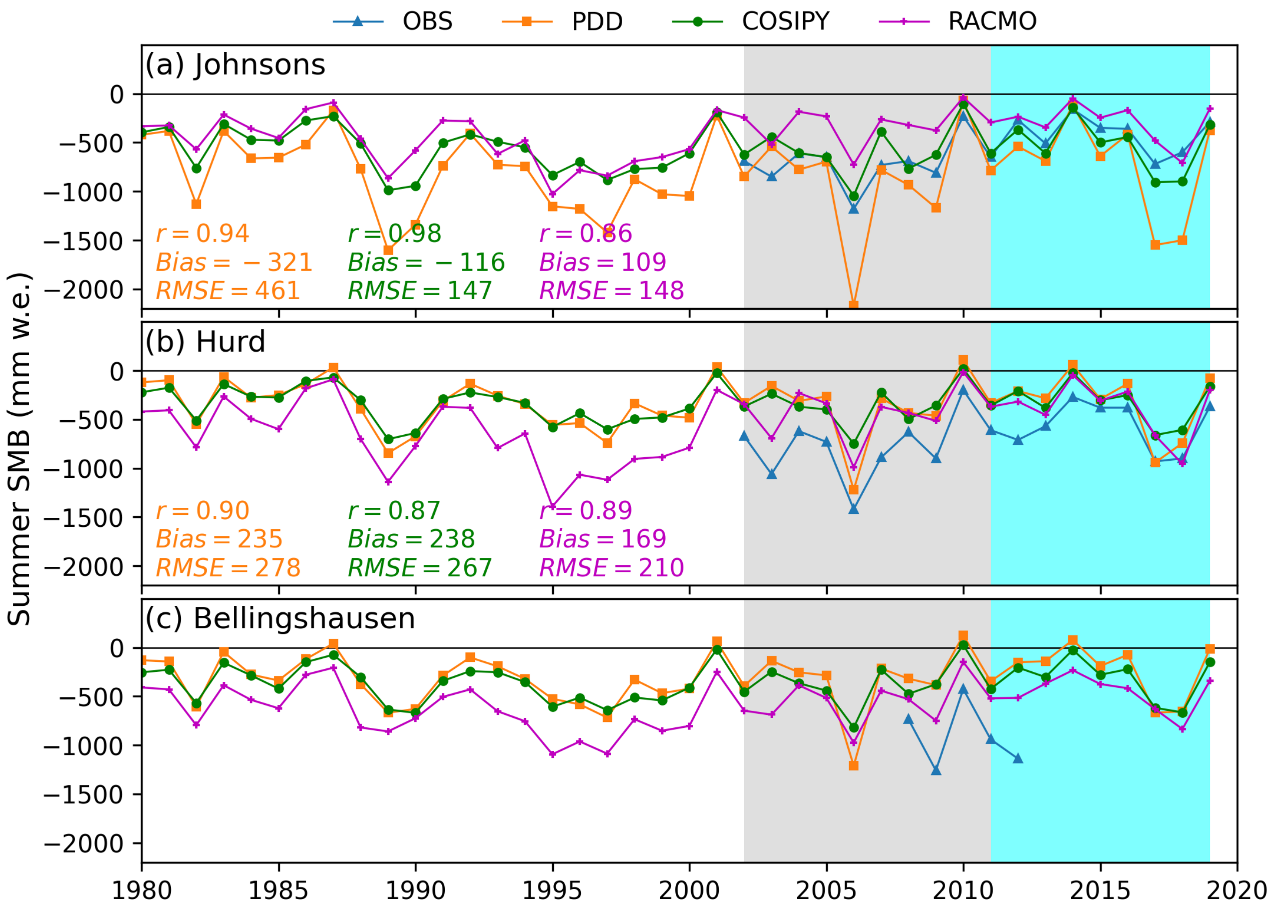

Figure S7. The same as in Fig. S5 but for the summer (December to March).

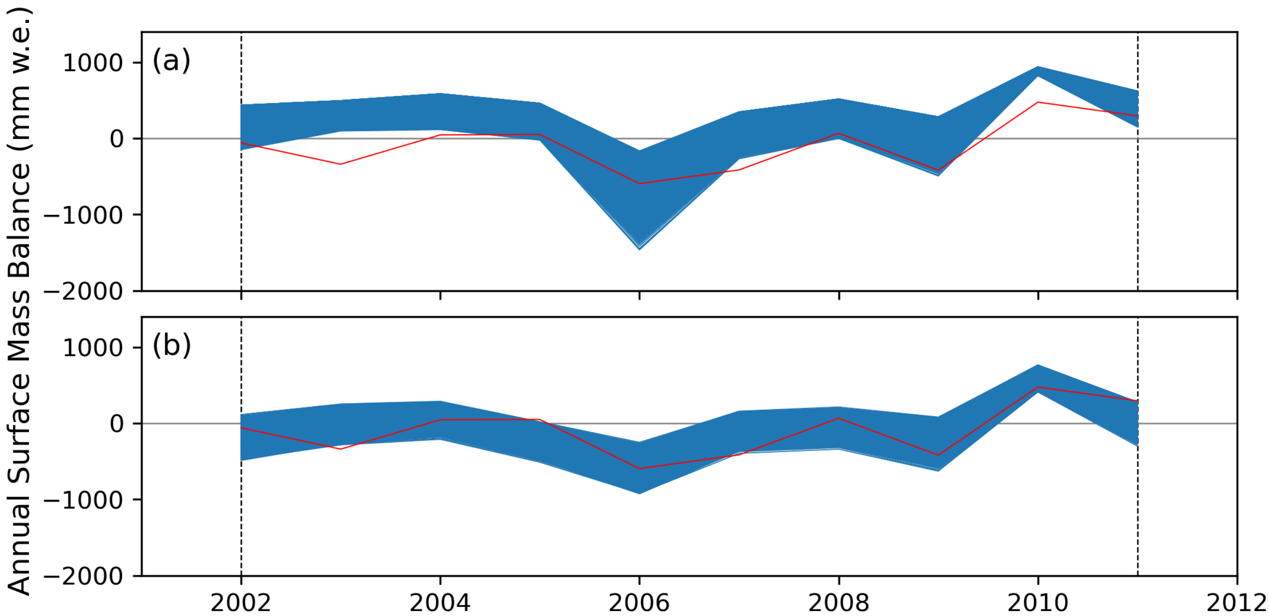

Figure S8. Annual SMB modeled with (a) PPD and (b) COSIPY models for the calibration period (2002-2011) using Randomized Grid Search technique (1000 model runs). Note that the red line indicates the observed SMB and the blue lines indicate the modeling.

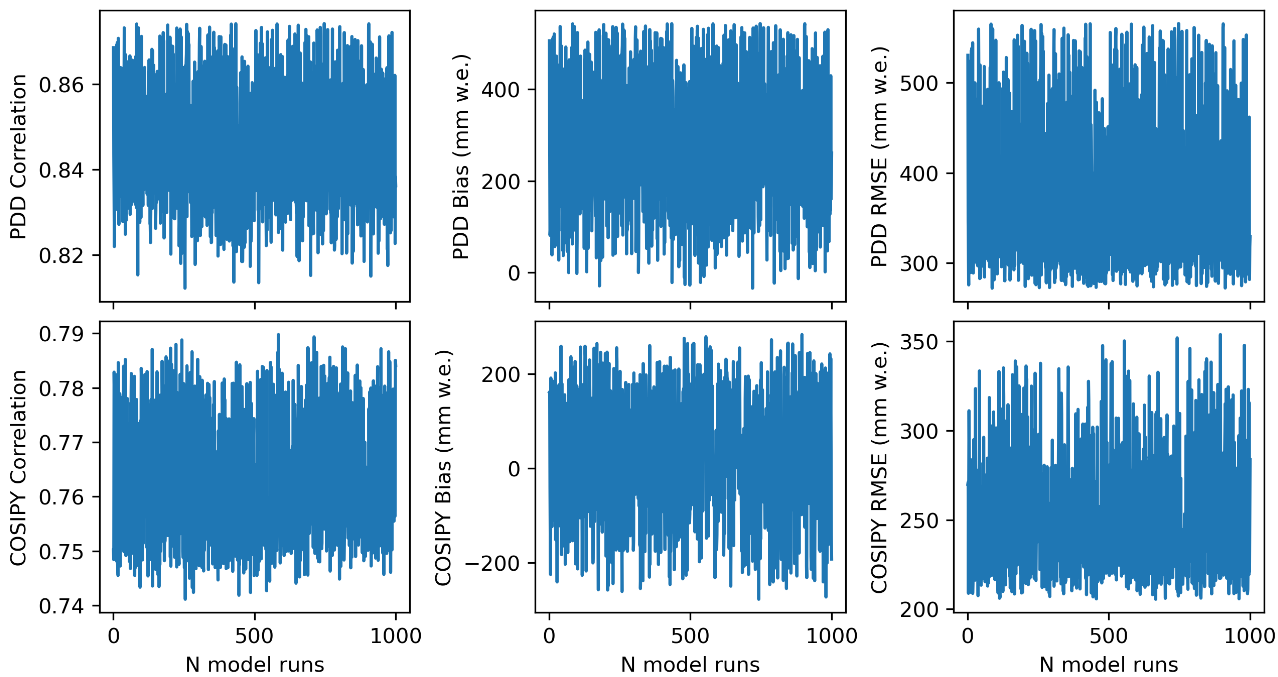

Figure S9. Correlation coefficient (r), bias (Bias), and root mean square error (RMSE) for the calibration period (2002-2011) using Randomized Grid Search technique (1000 model runs). Upper for PPD and lower for COSIPY.

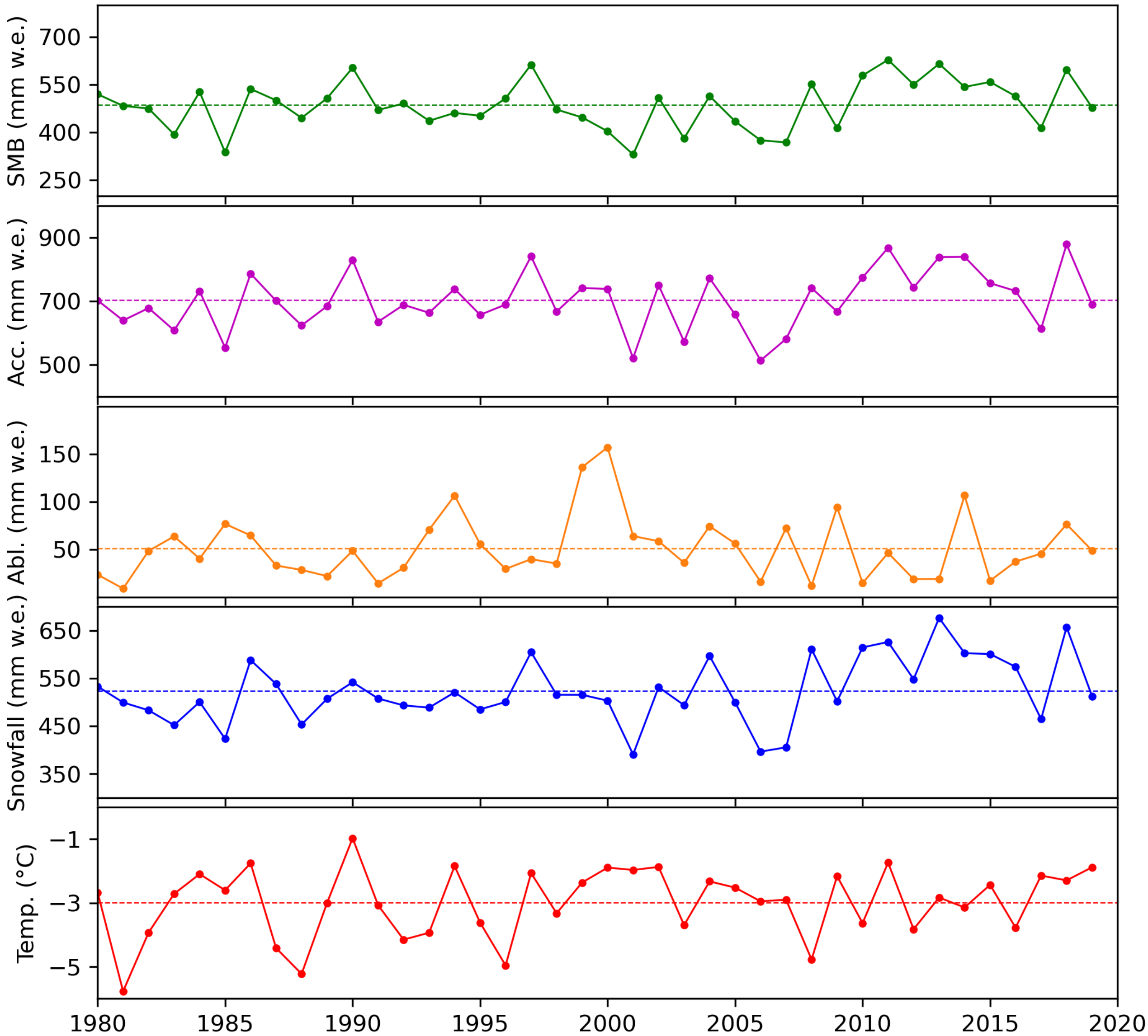

Figure S10. The same as in Fig. 5 but for the winter (April to November).

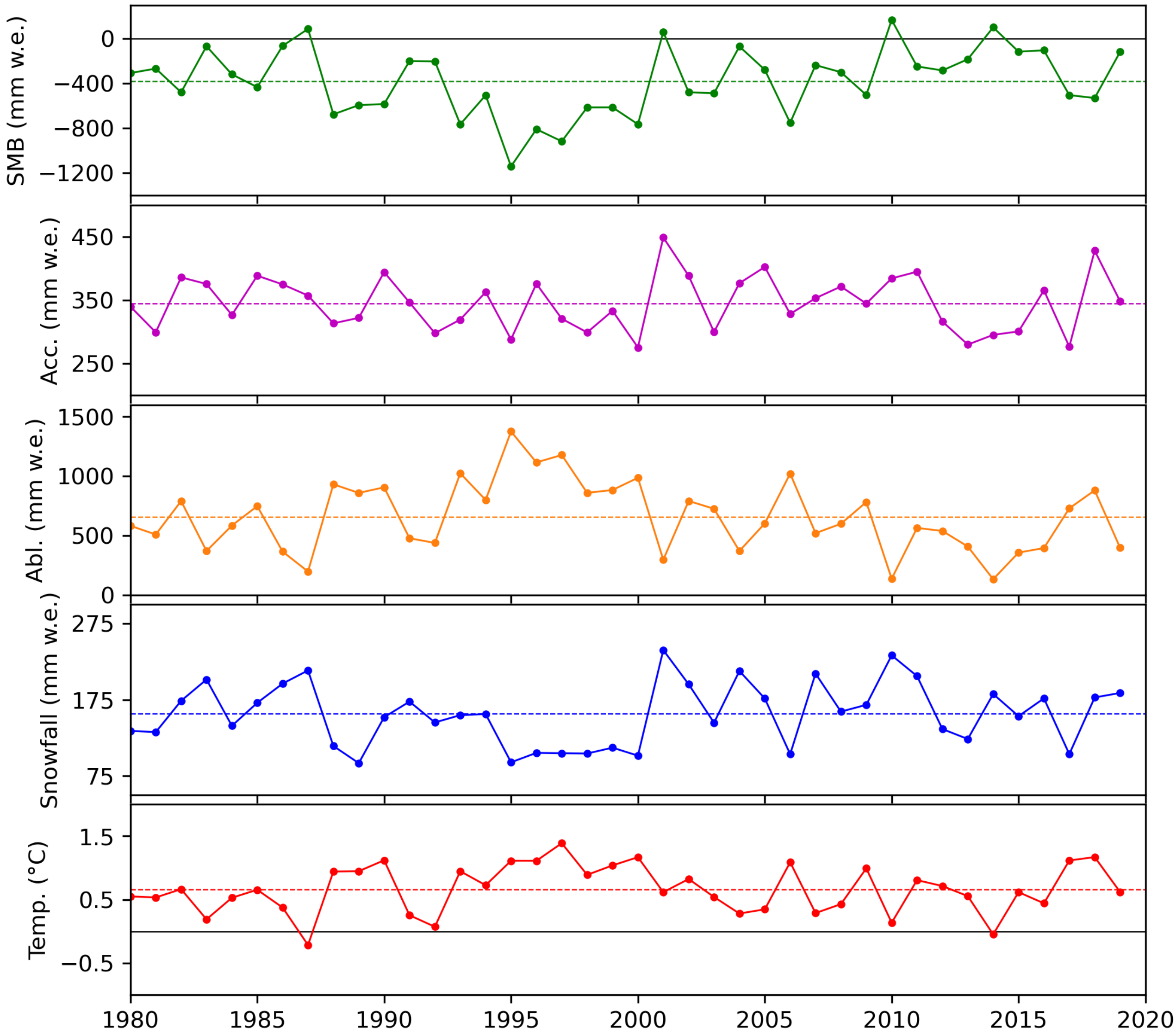

Figure S11. The same as in Fig. 5 but for the summer (December to March).

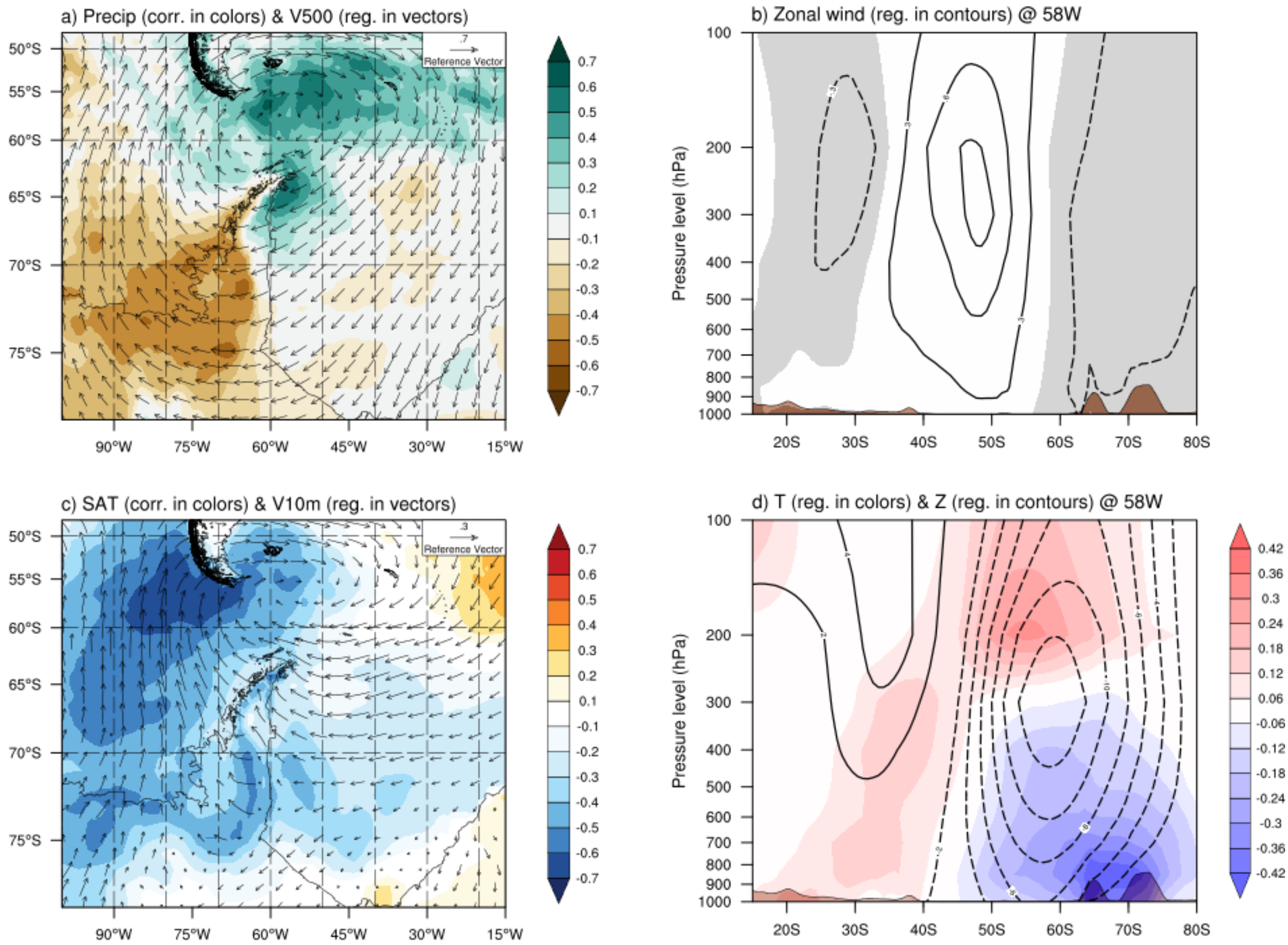

Figure S12. The same as in Fig. 6 but using GLAS_COSIPY time series.

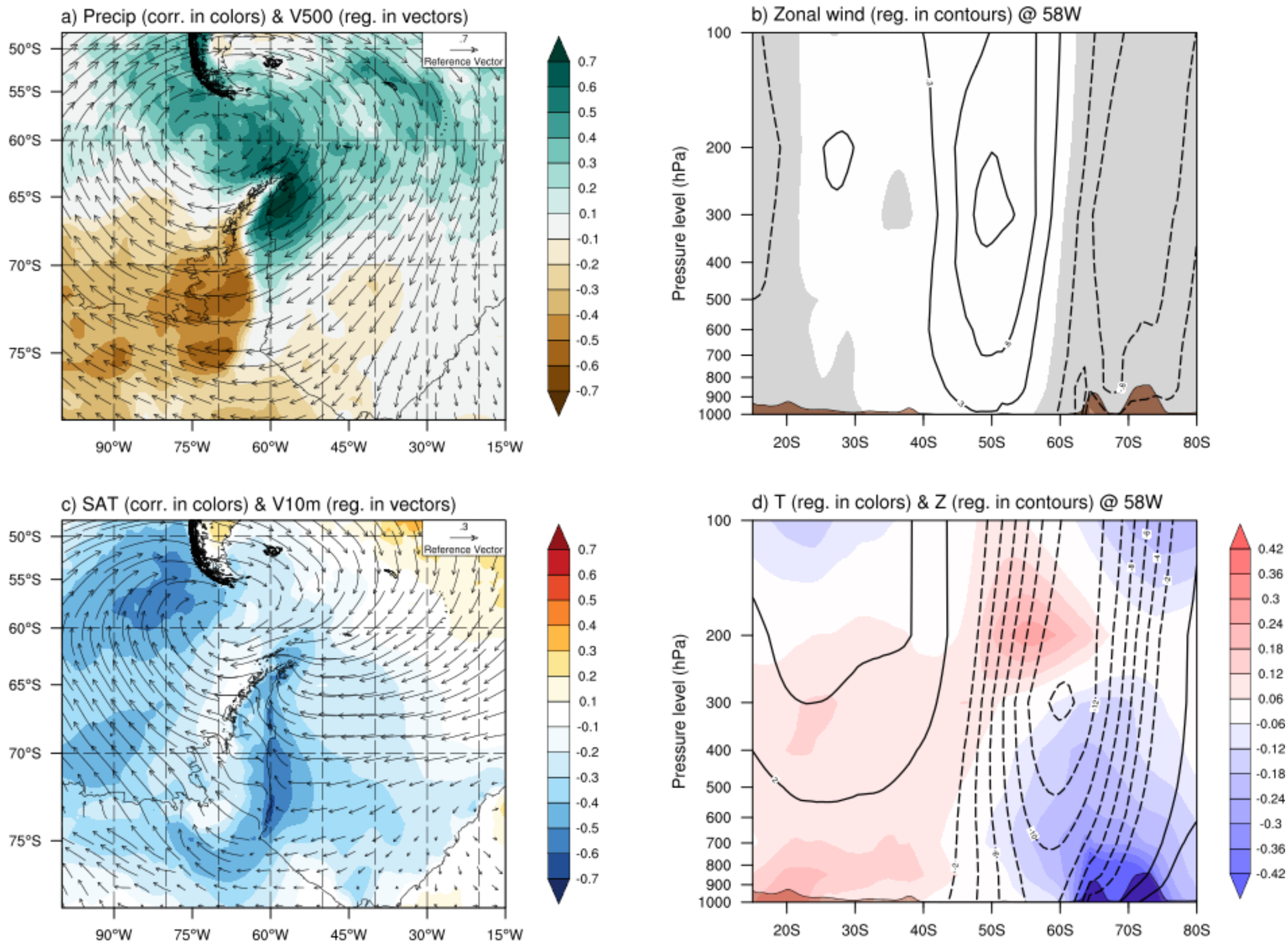

Figure S13. The same as in Fig. 7 but using GLAS_COSIPY time series.

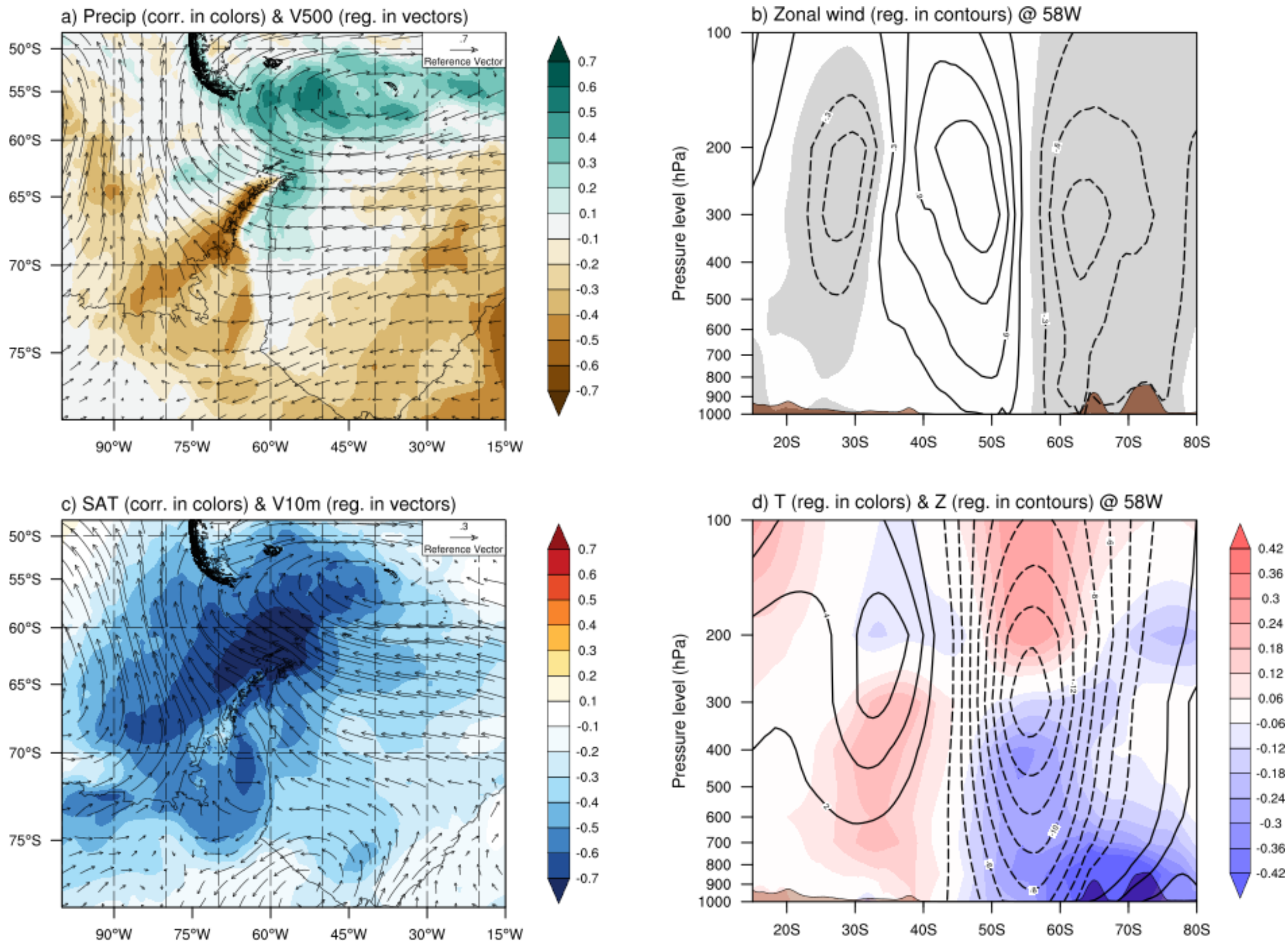

Figure S14. The same as in Fig. 8 but using GLAS_COSIPY time series.

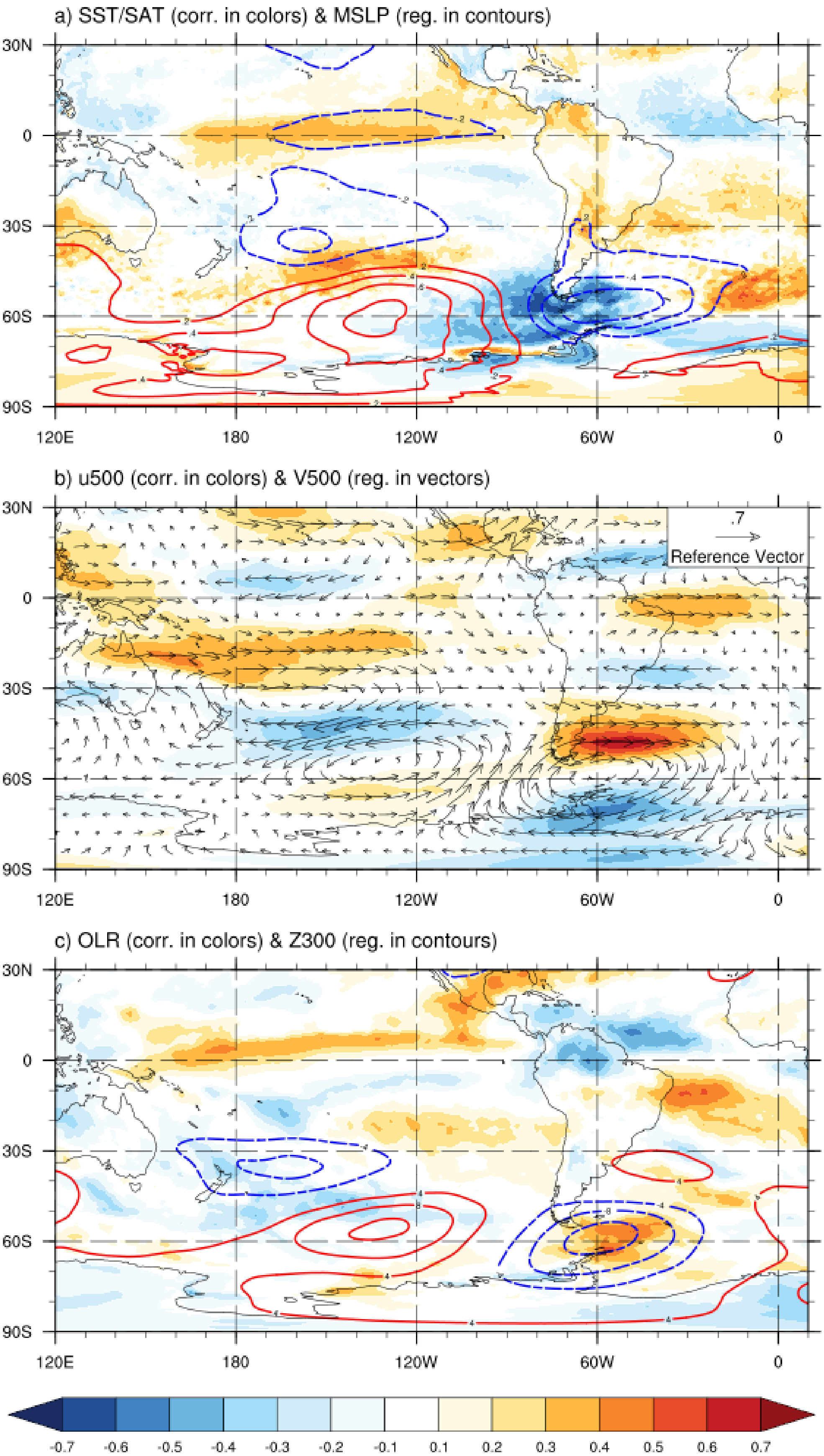

Figure S15. The same as in Fig. 9 but using GLAS_COSIPY time series.

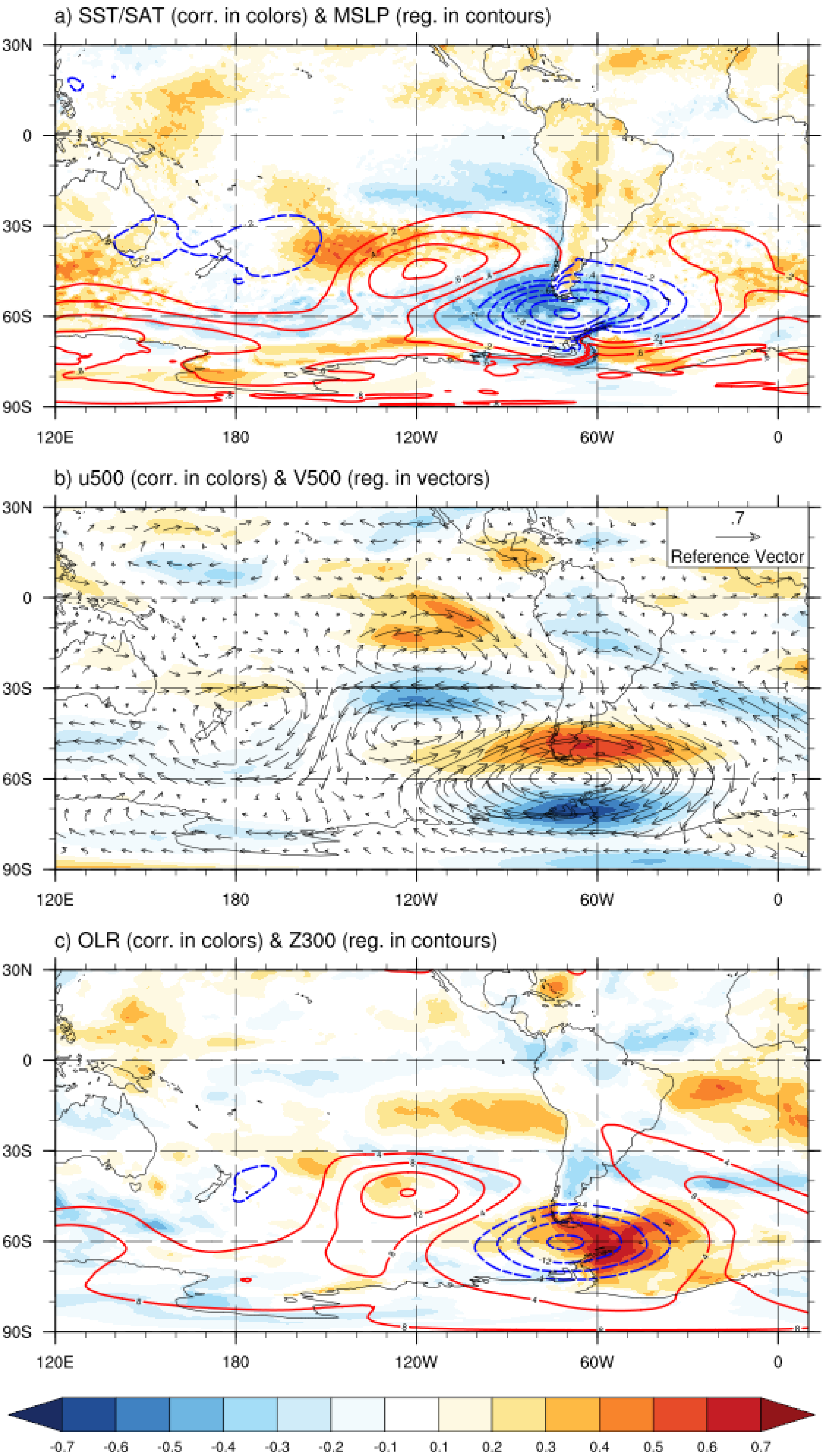

Figure S16. The same as in Fig. 10 but using GLAS_COSIPY time series.

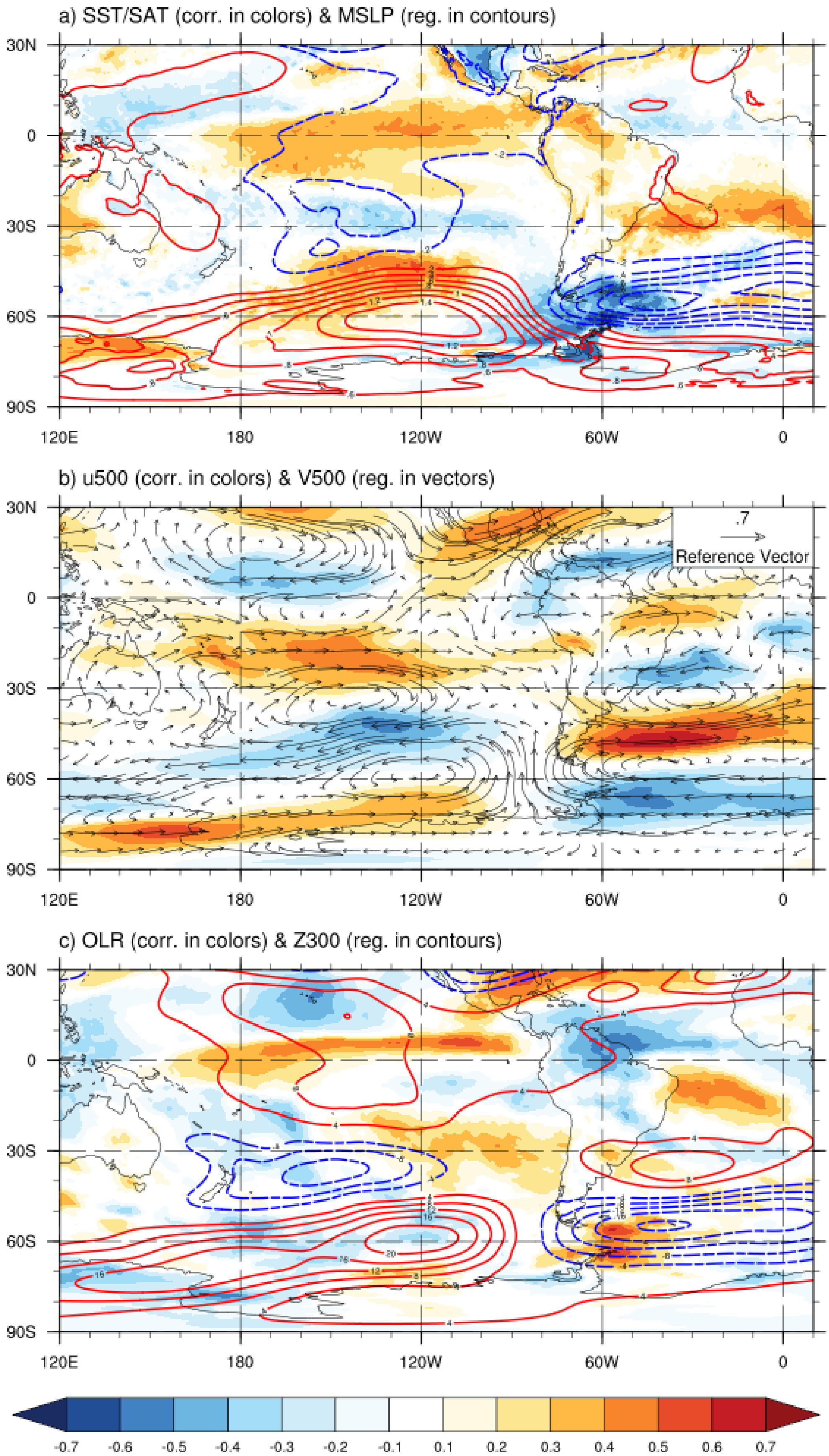

Figure S17. The same as in Fig. 11 but using GLAS_COSIPY time series.

References

Boone, A. (2002). Description du schema de neige isba-es (explicit snow). *Description of the ISBA-ES (Explicit snow scheme), Note de Centre, Meteo-France/CNRM*, *70*.

Brock, B. W., Willis, I. C., & Sharp, M. J. (2006). Measurement and parameterization of aerodynamic roughness length variations at haut glacier d'arolla, switzerland. *Journal of Glaciology*, *52*(177), 281–297. https://doi.org/10.3189/172756506781828746

Gromke, C., Manes, C., Walter, B., Lehning, M., & Guala, M. (2011). Aerodynamic roughness length of fresh snow. *Boundary-Layer Meteorology*, *141*, 21–34. https://doi.org/10.1007/s10546-011-9623-3

Mölg, T., Maussion, F., Yang, W., & Scherer, D. (2012). The footprint of asian monsoon dynamics in the mass and energy balance of a tibetan glacier. *The Cryosphere*, *6*(6), 1445–1461. https://doi.org/10.5194/tc-6-1445-2012

Oerlemans, J., & Knap, W. H. (1998). A 1 year record of global radiation and albedo in the ablation zone of morteratschgletscher, switzerland. *Journal of Glaciology*, *44*(147), 231–238. https://doi.org/10.3189/S0022143000002574

9.2 The SCAR report

SCAR Fellowship Report

High-resolution atmospheric and glaciological modelling for the South Shetland Islands on the northern Antarctic Peninsula

Christian Torres
PhD Student
Federal University of Rio Grande, Brazil
christian010194@gmail.com

Home Institution: Institute of Oceanography, Federal University of Rio Grande
Prof. Dr. Jorge Arigony-Neto | jorgearigony@furg.br | Brazil

Host Institution: Department of Meteorology, University of Valparaíso
Prof. Dr. Deniz Bozkurt | deniz.bozkurt@uv.cl | Chile

Dates of Activity 01/04/2023 - 30/11/2023

Introduction

Since the 1950s, the Antarctic Peninsula (AP) has experienced one of the most significant warming trends on Earth causing abrupt changes in the cryosphere of this region. However, there are a few detailed studies investigating atmosphere-cryosphere interactions on the small island glaciers like those found on the South Shetland Islands (SSI), due to the harsh environmental conditions, which impose a limitation on the field data collection. In addition, due to the insufficient observational network and complex topographical features, precipitation—a crucial variable in determining glacier surface mass balance (SMB)—over these small regions are poorly represented in global reanalysis and climate models (e.g., ERA5, CMIP5 and CMIP6). In this context, regional climate models (RCM) can be used to provide climatological variables at a high-spatiotemporal resolution with more accuracy over these small regions.

Project Objectives

The objectives of this study were threefold: (1) to analyse the capability of the Polar version of the Weather Research and Forecasting (PWRF) model in producing accurate high resolution datasets of atmospheric variables, particularly the total precipitation and solar radiation, for the SSI on the northern AP; (2) to force the new COupled Snowpack and Ice surface energy and mass-balance model in PYthon (COSIPY) with PWRF and to evaluate its ability to simulate the glacier SMB; and (3) to describe the local scale atmospheric (precipitation and solar radiation) and glaciological (SMB) characteristics on the SSI obtain a more spatially detailed.

Methods, Execution and Results

We utilised the PWRF model, version 3.9.1, to generate high-resolution atmospheric data for the SSI. Our setup consists of three nested domains spatial resolutions of 15, 5 and 1 km with a one-way nesting approach on a polar stereographic projection. For our simulation domain, we incorporated the updated Reference Elevation Model of Antarctica (REMA) from Howat et al. (2019). The modelling experiment was tested for both one summer (January) and winter (July) month in 2013. The ERA5 reanalysis released by ECMWF was used for the PWRF model initialization and input of the boundary conditions at six-hours intervals. The physics options used in this study were obtained from Bozkurt et al. (2020). Additionally, we conducted sensitivity experiments for both microphysics and cumulus schemes.

To assess the accuracy of PWRF simulations, we compared them with observational data from two stations: one situated on a glacier surface (Fourcade and Polar Club Glacier) and another on a bare ground surface (King Sejong Station). The results of the PWRF sensitivity experiments revealed that employing the Morrison 2 moment microphysics and Grell Freitas cumulus schemes enhanced the accuracy and reduced bias in temperature, surface pressure, wind, and solar radiation variables. However, longwave atmospheric radiation was only moderately represented by different PWRF configurations. Furthermore, the high-resolution PWRF outputs exhibited improved representation of precipitation, attributed to orthographic influence.

For the meteorological fields, we used the best high-resolution PWRF output to force the COSIPY model for the same period (January and July 2013). The glaciological modelling results demonstrated a more accurate spatial representation of the SMB for these small glaciers. In summer, the SMB exhibited a strongly negative trend in the lower parts and a moderately positive trend in the upper parts of the glaciers. Conversely, during winter, the SMB was highly positive across almost the entire glacier area. These findings offer valuable insights into the spatial distribution of energy and mass fluxes within the small glaciers situated on the SSI.

Project Outcomes

The PWRF atmospheric model provides multiple options for parameterization of selected physical processes, e.g., cloud microphysics, cumulus, radiation or boundary layer turbulence. One of the main outcomes of this project was to find an optimised configuration for cloud microphysics and cumulus schemes to acquire high-resolution climatic data over the small islands region like those found on the SSI, northern AP. This optimal PWRF configuration tested and verified over this region can be used over small islands for long-term climate simulations, case study analyses, etc. In addition, the utilisation of this model (i.e., PWRF) empowered us to acquire high-resolution meteorological fields for both one summer (January) and winter month (July) in 2013. These substantial data, totaling around 28GB, were efficiently stored in netCDF files for user-friendly availability. Subsequently, we used these high-resolution atmospheric datasets to force the COSIPY model, generating energy and mass balance data with more detail for small glaciers within the SSI. These datasets, comprising approximately 1GB, were also stored into netCDF files for user-friendly dissemination. The enhanced spatial resolution allowed a more understanding of local atmospheric and glaciological processes in this region. For instance, on January 7, 2013, a low-pressure system was identified to the east of the SSI. This cyclonic system, coupled with the intricate local orography of the northern AP, induced strong southward winds at the SSI. This meteorological event aligns with findings from a previous study by Kwon et al. (2019). Additionally, the intensified winds coincided with minor surface temperature and substantial snowfall over the SSI, as corroborated by our PWRF outputs. This event contributed to the SMB of the small glaciers within the SSI. I am very satisfied with these new results that can surely be published in an international journal.

Publications, Presentations and Products

We are writing the results of the atmospheric and glaciological simulations in a single manuscript that will be submitted to an international journal in the coming months. Additionally, the results of this project will be presented next year at the SCAR Open Science Conference 2024 “Antarctic Science: Crossroads for a New Hope" in Pucón, Chile. We will also put the atmospheric and glaciological data, PWRF namalists and scripts files in a github repository to make it freely available to the scientific community. In this way, other researchers and students will be able to replicate it at their study sites. On the other hand, during the exchange I attended two international conferences (International Union of Geodesy and Geophysics-IUGG and Congreso de la Sociedad Chilena de la Criósfera-SOCHICRI) presenting preliminary results of my PhD and this project. In addition, preliminary results of the impact of Atmospheric Rivers on small glaciers located on the SSI were presented at the XI Antarctic Conference between 24 and 26 October in Punta Arenas, Chile. Complementary, a research proposal for the CLIMATE-AmSud (https://www.sticmathamsud.org/sitio/) programme was led and submitted by me during this exchange. This proposal aims at strengthening research networks from Peru, Chile, Bolivia, Ecuador, Brazil and France on topics related to machine learning, glaciology, climate and extreme weather events. Finally, during the exchange I took the opportunity to write and discuss with my host supervisor two manuscripts. One was accepted in November for publication in Annals of the Brazilian

Academy of Sciences and the other is under discussion by the co-authors for submission early January next year to Journal of Glaciology.

Capacity Building, Education and Outreach Activities

During the exchange, I introduced my SCAR project to researchers at the host institution, and their enthusiastic interest provided valuable feedback. This collaboration not only fostered a dynamic exchange of ideas, but also allowed me to substantially expand my research network, with a focus on climate change, meteorology and glaciology. I am currently in the process of planning to share my SCAR fellowship experience with both undergraduate and graduate students at my home institution. Numerous colleagues from my home institution are actively engaged in developing their research projects within the AP, concentrating on oceanographic and biological aspects. Therefore, sharing my experience can motivate my colleagues to apply to the SCAR fellowship program and they can do an exchange at another institution to increase their skills.

Future Plans and Follow-ups

Next year I will finish my PhD, then I plan to do a postdoc. I am in constant communication with my host supervisor to finalise the manuscript we are writing with the results of this SCAR-project. I will take advantage of these meetings to tell him about the possibility of applying for a postdoc fellowship in Chile. During this postdoc I will focus on the study of extreme events and their role in synoptic atmospheric circulation anomalies and their impacts on small glaciers in northern AP using the high-resolution glaciological and atmospheric data generated in this SCAR-project. During my participation in IUGG-2023 in Berlin, Germany, as part of my PhD activities, I met leading researchers from British Antarctic Survey, UK, and Masaryk University, Czech, whose work involves RCM in Antarctica. In the future, I plan to try to visit these research institutions too.

Personal Impact

I am an Environmental Engineer by education and my work is to analyse the impact of climate change on small glaciers located in the northern AP and the Peruvian Andes. However, analysing glacier-atmosphere-ocean interaction in these small glaciers is not an easy task due to the limited availability of data and coarse resolution global model outputs. Through this exchange, I acquired fundamental skills in RCM that are fundamental for a more detailed understanding of atmospheric processes at regional and local scales. This exchange definitely increased my skills for a successful career in the field of glaciology, meteorology and climatology. On the other hand, my scientific working group will also benefit from high-resolution atmospheric and glaciological datasets.

Financial Statement

The funds provided by the fellowship were used exclusively to sustain my own living expenses, which includes travel costs, accommodation, health insurance and groceries.

Acknowledgements and References:

I would like to thank Prof. Dr. Deniz Bozkurt for giving me support in RCM and also for the extensive conversations we had during this visit on scientific, cultural and social issues, which definitely allowed me to grow professionally and personally. I would also like to thank Prof. Dr. Jorge Arigony for having provided the facilities with my home institution to carry out this exchange in Chile. In addition, we would like to thank the National Laboratory for High Performance Computing (NLHPC) from the University of Chile, this project was partially supported by the supercomputing infrastructure of the NLHPC (ECM-02:Powered@NLHPC). Finally, the data (KOPRI-KPDC-00000960) from King Sejong Station used in this work was provided by the Korea Polar Research Institute and we are very grateful.

Bozkurt, D., Bromwich, D. H., Carrasco, J., Hines, K. M., Maureira, J. C., & Rondanelli, R. (2020). Recent near-surface temperature trends in the Antarctic Peninsula from observed, reanalysis and regional climate model data. Advances in Atmospheric Sciences, 37, 477-493.

Howat, I. M., Porter, C., Smith, B. E., Noh, M. J., & Morin, P. (2019). The reference elevation model of Antarctica. The Cryosphere, 13(2), 665-674.

Kwon, H., Park, S. J., Lee, S., Kim, B. M., Choi, T., & Kim, S. J. (2019). A numerical simulation of a strong wind event in January 2013 at King Sejong station, Antarctica. Quarterly Journal of the Royal Meteorological Society, 145(720), 1267-1280.